Mutual Interactions between Shock Waves and Structures

by
Minwei Gong

Submitted to the School of Engineering
in partial fulfillment of the requirements for the degree of
Doctor of Philosophy
at the
City University of New York
2006

This manuscript has been read and accepted for the Graduate Faculty in Engineering in satisfaction of the dissertation requirement for the degree of Doctor of Philosophy.

. . . . . .

Prof. Yiannis Andreopoulos

. . . . . .

Prof. Mumtaz K. Kassir

. . . . . .

Prof. Feridun Delale

. . . . . .

Prof. Charles Watkins

. . . . . .

Prof. Ben Liaw

. . . . . .

Prof. Kolluru Subramaniam

. . . . . .

Prof. Constantine Chassapis

THE CITY UNIVERSITY OF NEW YORK

Abstract

Mutual Interactions between Shock Waves and Structures

by

Minwei Gong

Adviser: Professor Yiannis Andreopoulos

In this thesis, the mutual interaction of shock waves and structures was studied. Experiments were carried out in a shock tube to investigate the aero-elastic response of fully clamped thin circular plates during face-on impact with planar shock waves. High frequency response dynamic strain history was obtained on various locations of the plate and measurement of acoustic pressure excited by the vibrating plate was performed as well. Analytical formulas based on Poisson-Kirchoff theory were employed to determine the modal frequency. These modal frequency was also calculated by performing Finite Element Analysis consists of a coupled system of equations between the fluid and solid phases. Further more, a coupled aero-elastic solver based on *quad-edge* data structure was implemented to solve the fluid structure interaction problem. The moving boundary was treated with an advancing front remeshing which was fully conservative. Adaptive mesh refinement was also implemented for improved efficiency and accuracy. Numerical strain history of the plate was obtained as well as the full flow filed. It was also shown that shock wave reflection starts at the same time at all locations of contact, and the reflected pressure may exceed the pressure reflected off a rigid wall in comparable configuration. Further non-linear analysis was performed on the numerical results. The time and location of the shock wave formation as a result of non-linear propagation of the pressure wave was estimated analytically. Non-linearity intensifies when the plate is vibrating at high frequency while the wave propagation speed is low which is characterized by the characteristic time scale of the plate vibration and pressure wave propagation.

Acknowledgments

First of all, I would like to thank my PhDs committee members for their various suggestions and insightful advice throughout the years. Especially I am grateful to my my advisor, Prof. Yiannis Andreopoulos, under whose guidance this research was undertaken. His physical perspective and scientific spirit was indispensable to my work. I would also like to thank Dr. Zhexuan Wang, Dr. Savvas Xanthos and Mr. Alexis Pierides, for their inspiration and readiness for help, and sometimes, showing up as the necessary impetus for pushing things forward. I would also like to express my thanks to Mr. Jinrui Chen for his help in the preparation of my experimental setup, where he provided necessary resources and assisted directly on some of the machining work. Dr. Yanxiong Liu and Dr. Tomas Cheung also helped directly on the material test experiment. I would also like to acknowledge the useful discussions I have had with my roommates, Mr. Huapei Wan and Mr. Zhihua Yi, on the topics of structure analysis and blast waves.

I would also like to thank my parents for their confidence on me and the moral support they have provided in my study and work.

Finally, things like open source software, and the work of many other researchers, all available over the Internet, made my own work much more comfortable. In some instances, it would not have been possible for me to finish the coding without such resources.

Contents

List of Tables

List of Figures

Chapter 1

Introduction

1.1 Introduction

The mutual interaction between structure and blast waves or shock waves is the subject of this research. Impingement of blast waves on structures can cause a reflection wave off the surface of the structure followed by a substantial transient aerodynamic load, which can cause significant deformation of the structure. In addition, a complex aeroelastic interaction between the blast wave and the structure develops that can induce reverberation within an enclosure, which can cause substantial overpressure through multiple reflections of the wave. Thus human injuries can occur at blast levels much lower than those that can cause equipment damage. This problem is of particular importance in the new design of future army vehicles with composite materials. It has been observed in the field that blast waves impinging on the external surface of army vehicles could induce substantial waves within the crew/personnel compartment. Excessive levels of sound can cause permanent hearing loss and can be deleterious, both physiologically and psychologically, to one's health.

Geometrical deformation caused by blast loading may also give rise to complicated fluid dynamic phenomena. The complexity of the interaction lies in that the deformation of the structure caused by blast wave loading can alter the overpressure that is built behind the reflected shock, and the geometrical deformation can then have an effect on the flow,

change the maneuvering of an aeronautical vehicle or a projectile.

The assessment of the effects of the blasts on structural systems was not studied systematically until World War I. The early published work was Hopkinson's study [33], in which he outlined his theory using scale models with the statement: "If two structural systems, identically similar except in size, be subjected to blast loading from two explosive charges whose weights are in proportion to the cube of the ratio of the linear dimensions of the two structures, then the behavior of the two structural systems will be identically similar with the distortions scaling as the ratio of the linear dimensions."

There are some studies related to structures subjected to blast loading in the literature and one of the the earliest analysis was performed by G.I.Taylor [53], where he developed a solution for one-dimensional wave impinging a free-standing plate to compute the momentum transmitted to the plate by the shock pulse. The prediction and measurement of the structural response of ship panels to free field air-blast explosions performed by Houlston *et. al* [34] was also among the earliest works. In the research conducted by Houlston and his co-workers, square plates and stiffened panels subjected to air-blast and underwater shock loads were investigated. Later, assuming a Navier form of displacement function and a modified Friedlander reflected blast oeverpressure loading that exponentially decays with time, Gupta *et. al.* [26] conducted a single-degree-of-freedom elastodynamic analysis of the response of a rectangular plate subjected to an explosive blast. Beshara [10] investigated the prediction of dynamic effects of unconfined explosions needed for the structural analysis of blast-loaded above-ground structures. Recently, Turkmen [57] carried out a study on the dynamic behavior of laminated composite plates subjected to blast loading. In his study, theoretical analysis and experiment results of the strain time histories were obtained. Very recently Zhenyu Xue and Hutchinson [61] studied the *quasi-static* dynamic responses of clamped circular sandwich plates subject to uniformly distributed impulsive loads. Numerical analysis on the plate neglecting the effects of fluid-structure interaction was carried out and a new constitutive relation for sandwich plates was introduced as well [62]. In a similar research [20] and [47], the dynamic responses of a clamped sandwich beam/plate

was assessed. The fluid-structure interaction effect was evaluated utilizing Taylor's [53] approximation by including a segregated *fluid-structure interaction phase* in their research.

However, all those aforementioned researches on the aeroelastic response of structure to blast or shock wave impact are all concentrated on the structure alone. Blast loading on the structure are treated in a simplified manner and the mutual interaction between the fluid and structure is either not accounted for or approximated in a loose-coupled fashion. Particularly, the complicated flow phenomena associated with sound excitation and shock waves reflections mentioned above have not yet been fully investigated.

1.2 Blast and Shock Wave Loading

Blast wave

A blast wave is generated by an explosion, which can be categorized as a physical, nuclear or chemical event. The rapid expansion of the gas caused by an explosion will generate a shock wave, followed by a rarefaction or an expansion wave.

Blast loading is directly related to the distance between the explosion and the structures, namely, the *stand-off distance*. As stand-off distance increases, blast pressure decays in relation to the cube of the stand-off distance and this can be expressed by a scaling law [44]:

$$\frac{R_1}{R_2} = \left(\frac{W_1}{W_2}\right)^{1/3} \tag{1.1}$$

where R is the distance from the center the explosion and W is the blast intensity. The pressure-time history of a blast wave can be described by an exponential function:

$$p(t) = p_s[1 - \frac{t}{T_s}]e^{-bt/T_s} \tag{1.2}$$

where t is time, $p(t)$ is the pressure history; p_s is the peak pressure of the blast wave; T_s is the characteristic time of the blast time, which indicates the time when the blast wave turns into negative;b is a parameter that gives the slope of the expansion wave following the

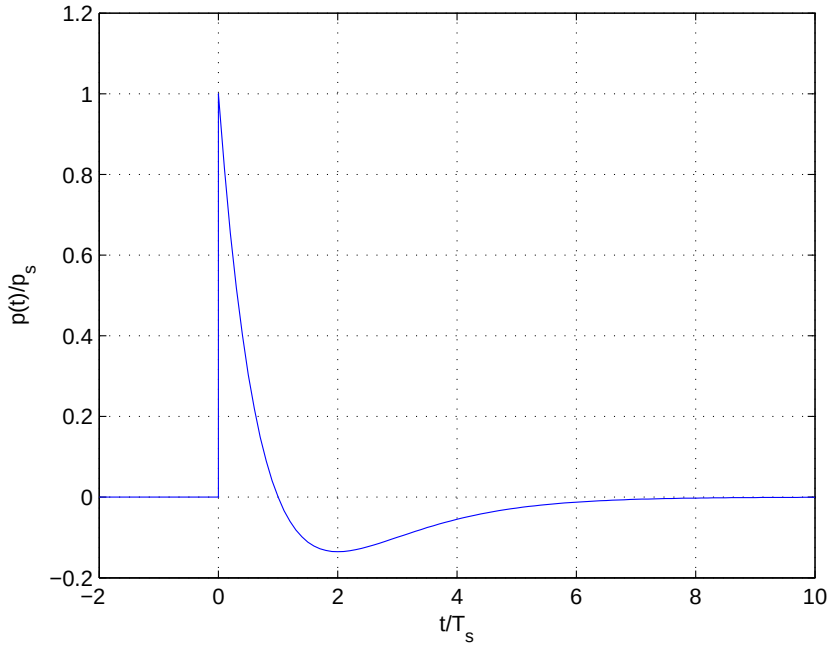

Figure 1-1: Type blast wave time history at $b = 1.0$.

pressure jump, a smaller b will result in a larger pressure drop. This pressure-time history $p(t)/p_s$ verses t/T_s is plotted in Figure 1-1.

Even though the ideal blast loading can be expressed by simplified equations, the actual blast wave is quite complicated. Figure 1-2 shows a typical blast wave measured with a CCNY omni-directional Blast Over Pressure probe [3]. Following the main incoming blast, there are also two other peaks which can be seen in the figure, they are the reflections of the blast wave off the ground and secondary blast wave.

Blast loading

When blast waves encounter a solid surface or an object made of medium more dense than air, they will reflect from it and depending on its geometry and size, diffract around it. High shearing rates occur during the impact of the shock wave front on the structural element because of the extremely short time scales of the flow. Relaxation of this high shearing rates take place immediately after the shock wave impact during the passage of the expansion

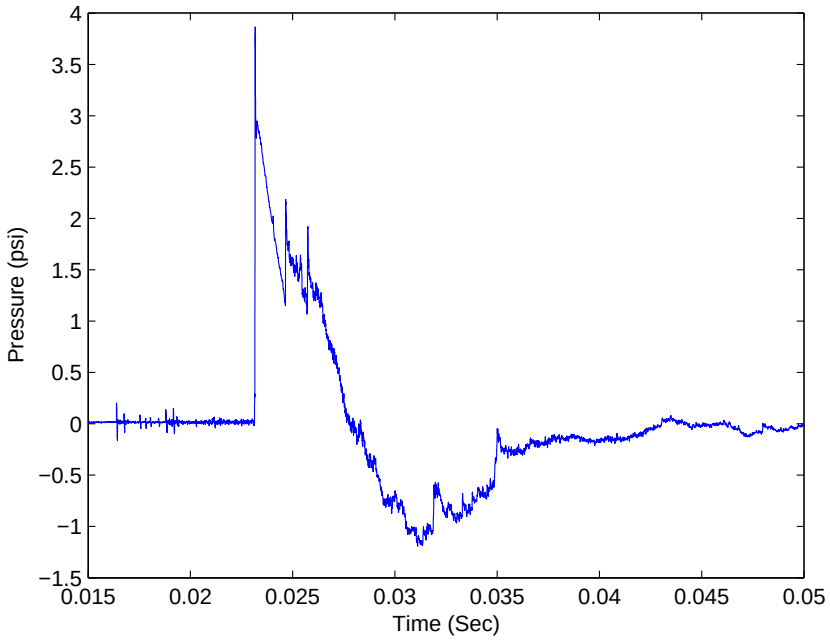

Figure 1-2: A typical blast wave measured with a CCNY Blast Over Pressure probe, 20ft away from a 1lb barecharge. Pressure transducer oriented 90^o to the incoming blast wave.

wave which is associated with time scales that are 10^3 times or more lower than those of the shock wave.

Depending on the time scales of the blast wave and that of the structure, the structure response to a blast loading can be categorized as the following: [44]

Impulsive response The load pulse is short compared to the natural period of vibration of the structure so structure response can be determined by applying the load pulse in the form of kinetic energy to the structure, which subsequently deforms and acquires strain energy.

Quasi-static Pressure load duration is long compared with the natural response time of the structure. The blast will cause the structure to deform whilst the loading is still being applied. The loading does work on the structure, causing it to deform and acquire strain energy.

Dynamic or pressure-time Load duration and structural response time are similar, equation of motion of the structural system is needed to solve the structural response. This is also the point of interest in the present research.

As mentioned above, blast loading is highly dependent on distance and time scales. It also varies with the direction that the blast loading is applied, which is related to the geometry of the structure and the wave propagation characteristics. As blast is inherently three dimensional, it will create reflections in multiple directions even if the structure itself is of simple geometry, e. g. a flat plate. In order to simplify the complexity of the problem, the present investigation focuses on the shock wave part of the blast wave. An idealized planar shock wave will facilitate the understanding of wave phenomena occurring during the fluid structure interaction. In addition, due to the short time scales associated with the shock wave impact, shearing/strain rates are higher than the rates developing during the expansion wave phase and therefore their role in the dynamic behavior of the structure may be more significant than the slow relaxation of the loading during the passage of expansion waves.

1.3 Summary

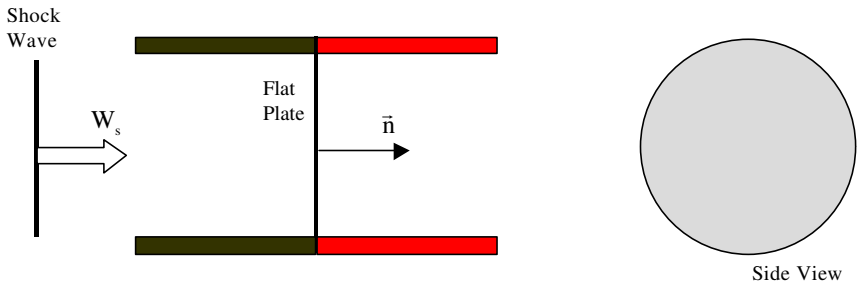

Figure 1-3: Shock wave interaction with thin flat plate.

With idealized, yet relevant geometry and simplified flow fields, the present research will focus on the shock wave and circular plate mutual interaction (see Figure 1-3). This

thesis will be organized as follows:

Chapter 1 is a brief Introduction.

Chapter 2 is devoted to the the experimental study. Experimental setup, measurement techniques, data acquisition and analyzing procedure are presented. The experimental results are also presented and discussed.

Chapter 3 analyzes the modes of the vibrating plate. An existing analytical method based on Poisson-Kirchoff plate theory was applied in the current research. Finite element modal analysis of the coupled structure and fluid problem was also implemented.

Chapter 4 describes a numerical scheme that can simulate the mutual interaction between the shock wave and structure. In this section, the three major models pertaining to CAE (Computational Aero Elasticity), namely, flow solver, structure solver and moving mesh algorithm, were studied and thereby a suitable model was chosen for performing fluid-structure interaction calculations.

Chapter 5 reports the numerical results. In this section, numerical simulation will be extended to problems with complicated geometries and length/time scales, e.g. blast wave and sandwich circular plate interaction.

Chapter 6 further analyze results and summarize the current research. Non-linear behavior of shock wave and structure interaction is studied in details in this section.

Chapter 7 is conclusion and summary.

Chapter 2

Experimental Study

In this chapter we will investigate the shock wave with the circular plate interaction problem experimentally in the CCNY shock tube facility. The approach of using a shock tube platform appears to have certain distinct advantages over approaches using detonations. The major one is that the shock front in the shock tube is planar, thus yielding uniform pressure loading on the structure. This simplifies the geometry and boundary conditions and therefore it allows for a better evaluation of modelling issues associated with numerical simulations of the phenomena involved. On the contrary, shock wave fronts generated by detonations are three dimensional in space and lead to complex pressure loadings which can mask the underlying basic physics of the impact.

2.1 Shock Tube

2.1.1 Shock Tube Facility

The experiments were carried out in the shock tube Research Facility shown in Figure 2-1. The shock tube is a powerful flow generating tool providing controllable high speed flows and shock waves. The facility is described in detail by Briassulis et al. [12].

This shock tube facility is of large scale dimensions with an inside diameter of 12 inches

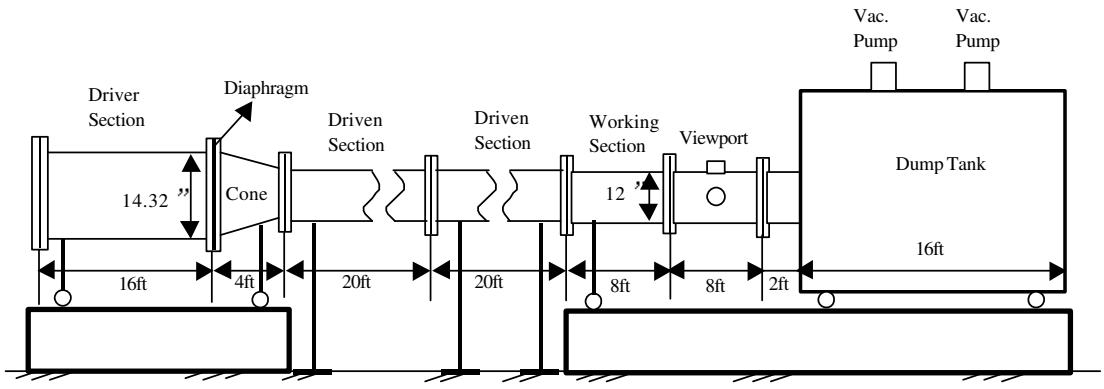

Figure 2-1: Schematic of Shock Tube Research Facility

and total length of 90 feet including all components. The facility consists of the following:

1. The driver section.
2. The conical reducer.
3. Two driven sections.
4. The working section.
5. Viewport section.
6. Dump Tank & Vacuum System.

2.1.2 Operation of Shock Tube

Initially, a circular aluminum diaphragm is inserted between the connecting flanges which separate the driver section from the rest of the facility, thus creating a partition. The $18\frac{1}{2} inch$ diameter diaphragms are machined with an inscribed score mark to create a stress concentration which will aid in rupturing the diaphragm and in controlling the bursting pressure. The basic operation consists of pressurizing the driver section until the dividing

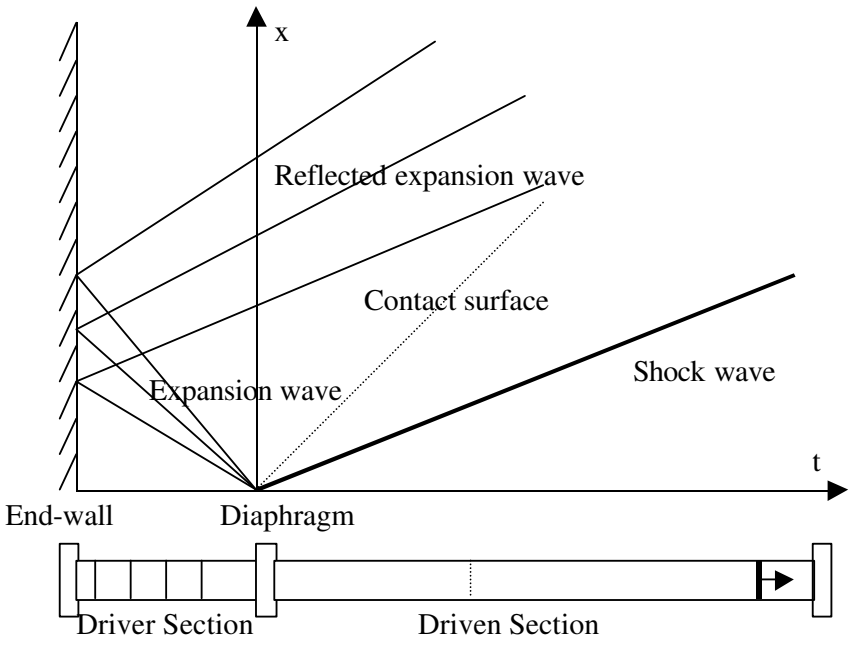

Figure 2-2: x-t diagram of the shock tube

diaphragm ruptures. Immediately after the diaphragm ruptures there is a simultaneous generation of a shock wave which travels downstream (into the driven section) at supersonic speed and expansion waves which travel at the local sonic speed in the opposite direction, upstream. The interface which separates the gas initially in the driver section from the gas in the driven section is known as the contact surface. This interface is associated with sharp changes in density and temperature between the two gases. The shock which is marked by a sharp jump in pressure induces uniform flow behind it while the expansion fan produces a gradual drop in pressure. The typical pressure history is presented in Figure 2-9. The x-t diagram is shown in Figure 2-2. The downstream travelling shock wave finally will propagate towards the end wall, where the plate is mounted.

2.1.3 Physics of the Interaction

A shock wave is considered travelling in a shock tube with a plate mounted at the end-wall. The pressure behind the incident shock wave, p_2, remains constant across the flow field before the shock reflection. As the shock wave touches the surface of the end wall the process of reflection starts, the plate is loaded and deformation begins. If the plate were a rigid body the pressure behind the reflected shock, p_5 would be given by the relation:

$$\frac{p_5}{p_2} = \frac{\left[\frac{\gamma+1}{\gamma-1} + 2\right]\frac{p_2}{p_1} - 1}{\frac{p_2}{p_1} + \left[\frac{\gamma+1}{\gamma-1}\right]} \tag{2.1}$$

In this relation, p_1 is the pressure ahead of the moving shock wave, p_2 is the pressure behind the shock wave and p_5 is the pressure behind the reflected shock wave which causes the aerodynamic load on the structures and γ is the ratio of specific heats C_p/C_v (see [2]). This pressure ratio is always greater than 1 indicating that consecutive reflections tend to increase the pressure behind each reflection substantially. The reason is that the kinetic energy of the moving shock wave and the flow behind is converted to potential energy after the reflection as the flow has to acquire the velocity of the reflecting boundary which is zero. Even for weak shock waves with a low pressure ratio $p_2/p_1 = 1.5$, the pressure behind a flat wall reflection will be $p_5/p_1 = 1.5 \times 1.47 = 2.2$. However, when the plate is elastic, its deformation starts at the moment load is applied during the initial contact between the shock wave and the surface. If we assume that the plate structure is rigid and the shock wave is a singular discontinuity then its reflection takes place instantaneously, with pressure p_5 applied instantaneously on the plate. In that aspect this is the loading pressure of the plate since the flow velocity behind the reflected shock is zero. In the case of an elastic plate equation 2.1 is not valid and as the aerodynamic load will reverberate the plate. During the initial displacement of the plate towards the $x > 0$ direction, expansion waves will be shed off in the direction of the reflected shock $x < 0$ and compression waves in the opposite direction on the external side of the plate. During displacement of the plate

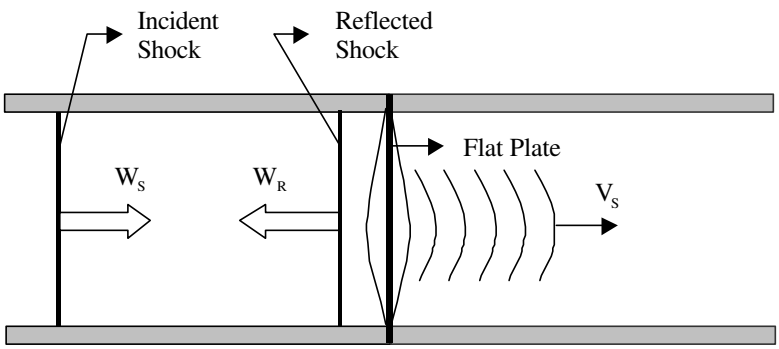

Figure 2-3: Illustration of shock wave and circular plate interaction.

in the other direction, compression waves will be shed off in the $x < 0$ direction behind the reflected shock wave and expansion waves will be shed off on the other side in $x > 0$ direction. (see Figure 2-3).

2.2 Measurement Techniques

2.2.1 Data Acquisition System

The present work required the implementation of a new high-speed data acquisition with high resolution. The PCI-416 are high performance A/D boards based on 32-bit PCI bus architecture. At this time, they represent the state-of the-art in "off the self" A/D boards. 4 DATEL PCI-416 A/D boards are integrated into a PC to provide 8 channels. The data acquisition systems is designed to acquire data with a rate of 1.0MHz and 14 bits resolution. New software has been developed to interface the boards and drive the data acquisition and data transfer. The software was developed in C/C++/Assembly language. A new circuit was also designed and implemented to synchronize the 4 A/D board, which provides simultaneous S/H and triggering.

2.2.2 Amplifier and Filter

Conditioning of the signal prior to digitizing was achieved through EG&G PARC Pre-amplifier/filters, model 5113. The units provide multiple filter and amplifier settings. The units allow for single ended and differential input modes, with both AC and DC coupling modes available. Maximum input voltage will depend on the coupling mode as DC offset is always presented in the experiment. There are two rolloff filter settings 6dB/octave and 12 dB/octave and the rolloff is centered about the chosen cut-off frequency.

All signals were low-passed filtered at 100 KHz with a response of 12dB/octave during the linear segment to roll off. Input signal amplitude gain settings varied depending on the magnitude of the signals to provide a suitable output range for the DATEL A/D board. Special consideration has been given to the wiring and grounding of the signals as they are essential for achieving the best possible signal to noise ratio (S/N).

2.2.3 Strain Measurement

Type-UHP5000-60 micro-strain gages fabricated by Kulite Semiconductors were used in this work. They have a size of $0.5mm \times 0.7mm$. They possess a high frequency response, high sensitivity and high signal to noise ratio. Their miniature size allows for localized measurement of strain.

Mounting and wiring these sub-miniature strain-gages on the plates required special attention and skills. They were first positioned on the plates with the help of a microscope. Immediately after, they were placed in an oven for several hours so that the epoxy was cured and a strong bond between the gage and the plate was created which allowed for a "point" measurement of the local strain. The plate was then mounted on the shock tube.

Constant Current technique is used to connect the strain gages. A battery operated power supply circuit was designed with temperature compensation taken into consideration such that minimum drifting and ripple is achieved. Since the experiment duration is quiet short in the range of 10ms, temperature drift effects on the strain gage are negligible. The

current experimental procedure guarantees that DC drifted can be calibrated in situ right before the interaction process. Calibration carried out also showed that changes in gage resistance result in proportional changes in the output voltage.

2.2.4 Pressure Measurement

High frequency response Kulite pressure transducers were used in the experiment for pressure measurement. Each of the pressure transducers was driven by batteries and carefully grounded to provide the best Signal/Noise ratio. Pressure transducers used in experiments function as the following:

1. provide triggering signal for the data acquisition.
2. record shock wave strength and speed.
3. record pressure of the plate during the impingement of the shock wave with the plate.
4. record resonance pressure as a result of the vibration of the plate.

Pressure transducers with different sensitivities were used in the experiments, ranging from 5psi to 250psi. Various holders have been designed and manufactured to hold the transducers in the experiment.

2.2.5 Acceleration Measurement

Several accelerometers are employed in the experiment to measure the acceleration of the plate during the interaction. The accelerometers are made by Analog Devices. Several accelerometers with model numbers ADXL190, ADXL250 and ADXL150 are tried in the experiment. Each of the models has a different sensitivity and operation range. These accelerometers use the newest iMEMS technology, which incorporates a complete acceleration measurement system on a single monolithic IC. It contains a polysillcon surface-micromachined sensor and signal conditioning circuitry to implement an open-loop acceleration measurement architecture. The ADXL 190 is capable of measuring both positive

and negative accelerations up to $\pm 100g$, which currently holds the highest range on AD products line for acceleration measurement.

The accelerometers also feature the built-in self-test and self-compensate functions that exercise both the mechanical structure and electrical circuitry. It provides a proportional voltage as output with regard to the acceleration. No calibration is needed for the accelerometer.

2.3 Shock Wave Impact on Isotropic Plates

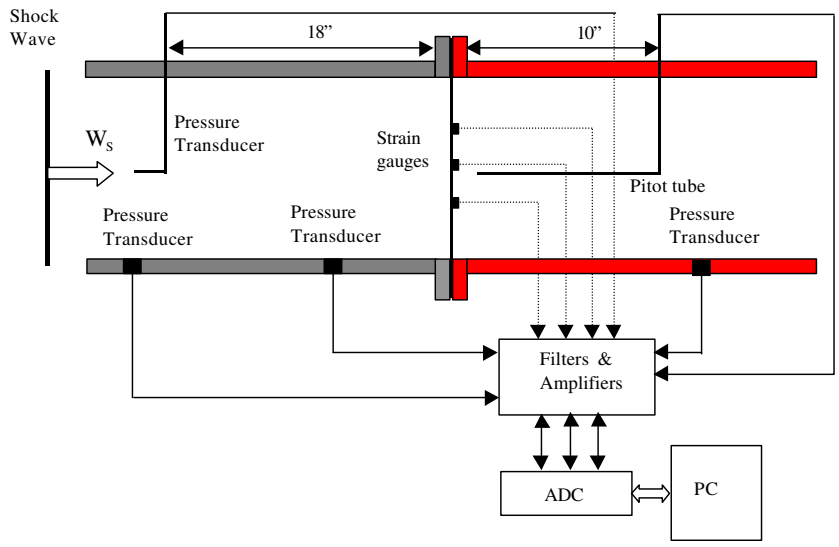

Figure 2-4: Experimental Setup

Figure 2-4 shows the experimental arrangement. Two wall pressure transducers and one total pressure transducer were used to monitor the flow and trigger the data acquisition. Two extra pressure transducers were placed near the rear (non-impacted) side of the plate. Among the two transducers, one was mounted on the wall to measure static pressure and the other at the tip of a holder to measure total pressure inside the flow. Dimensions of the plates and their material properties are given in Table 2.1. Each plate has a outer diameter of 14.5” while during the experiment, it was mounted on a flange of a diameter 12”, thus

Plate Material	Thickness (inch)	Diameter (inch)	Young's modulus (Gpa)	Poisson's ratio	Density ($10^3 kg/m^3$)
Aluminium	1/8"	14.5"/12"	71	0.33	2.7
Stainless Steel	1/16"	14.5"/12"	205	0.3	7.7
Composite	0.22"	14.5"/12"	33	0.25	1.81

Table 2.1: Geometry and material properties of various plates used in experiment.

result in an effective diameter of 12".

It also has to be mentioned that the composite plate is laminated with 10 woven fabric layers. The Young's modulus of the composite plate is obtained through an tensile test performed on a MTS-810 test system in the *Material Processing & Solid Mechanics Lab at CCNY*. In the subsequent calculation and numerical simulation, this plate will be regarded as quasi-isotropic.

The locations of the strain gages on each plate are shown in Figures 2-6 2-7 and 2-8. During experiments, the plate surface mounted with strain gages is on the non-shock impact exterior side, such that the thermo effect on the strain gages caused by the temperature fluctuations within the flow can be minimized. With such configuration, during the shock impact, strain gages near the edge of the plate will expect to undergo compression and result in a negative strain value. Strain gages mounted near the center of the plate are expected to have a positive value while experience tension. Such variation of exterior surface strain in the radial direction was illustrated in Figure 2-5. The transition from positive to negative strain occurs at $r = 0.628R$ and the maximum absolute strain is at the boundary of the plate.

2.3.1 Results

All the experiments are carried out with a pressure ratio $p_2/p_1 = 1.49$ across the incident shock wave. Figure 2-9 shows one typical wall pressure in the experiment. Figure 2-10 shows one typical strain gage signal obtained in the experiment with the aluminum plate. The two jumps in the pressure signal are caused by the passage of the incident and

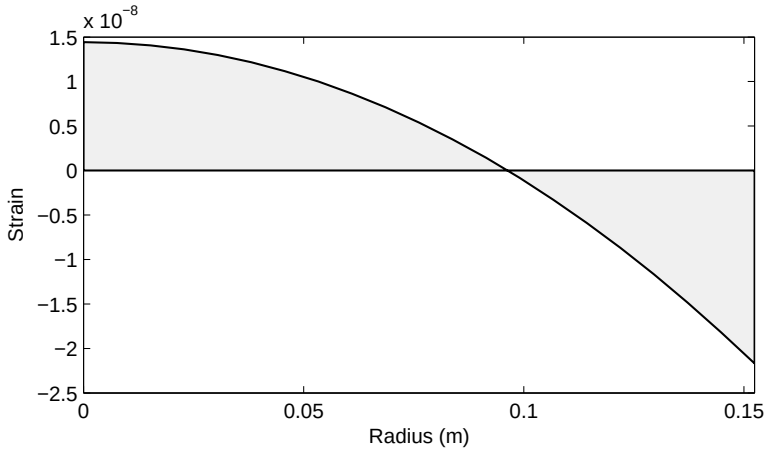

Figure 2-5: Variation of strain in radial direction along radius at the exterior surface of the fully clamped aluminum plate under steady uniform unit load.

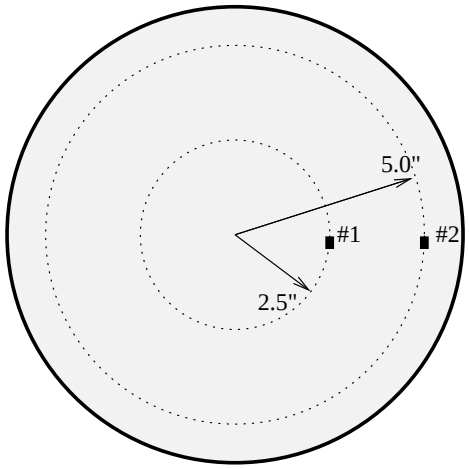

Figure 2-6: Strain Gage locations on Aluminum Plate

reflected shock waves. In the case of the strain gage signal the incident shock is reflected at the same position and at the same time. As a result of these combined effects of incident and reflected shock only one signal jump can be observed in the strain signal. The strain signal remains always negative due to compression at the location where strain gage #1 is mounted ($r = 5$"). The resonance pressure signal obtained by the pitot tube on the exterior side, across the plate, is also shown in Figure 2-10. Peak to peak fluctuations of $\pm 0.02 psi$ can be observed. The signal after the onset of the initial shock impact shows a considerable amount of periodicity. A frequency analysis of the signal by using Fast Fourier Transform

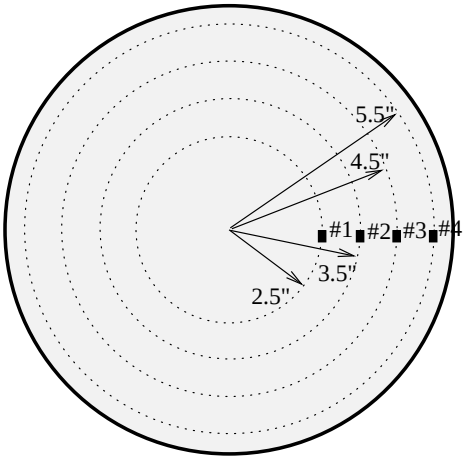

Figure 2-7: Strain Gage locations on Stainless Steel Plate

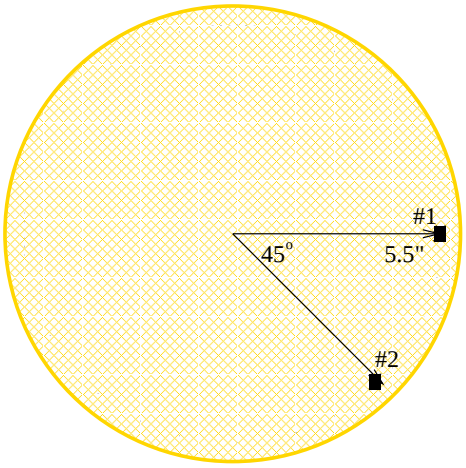

Figure 2-8: Strain Gage locations on Composite Plate

indicated the existence of several peaks in the spectrum (see Figures 2-12 and 2-11).

Several other frequencies multiple of the above were also found. It should be mentioned that the frequency window of the FFT is $500KHz/2^{14} = 30Hz$. It appears that a complicated wave pattern exists within the reverberating plate, which starts as soon as the shock gets in contact with the plate and gets reflected off the plate. This wave pattern may consist of compressive P-wave, shear SH - and/or SV-waves. The waves travel within the plate along its thickness and reflect off the rear face. They also reflect from the circular boundary which holds the plate and interact with themselves in a manner not yet understood. Peak

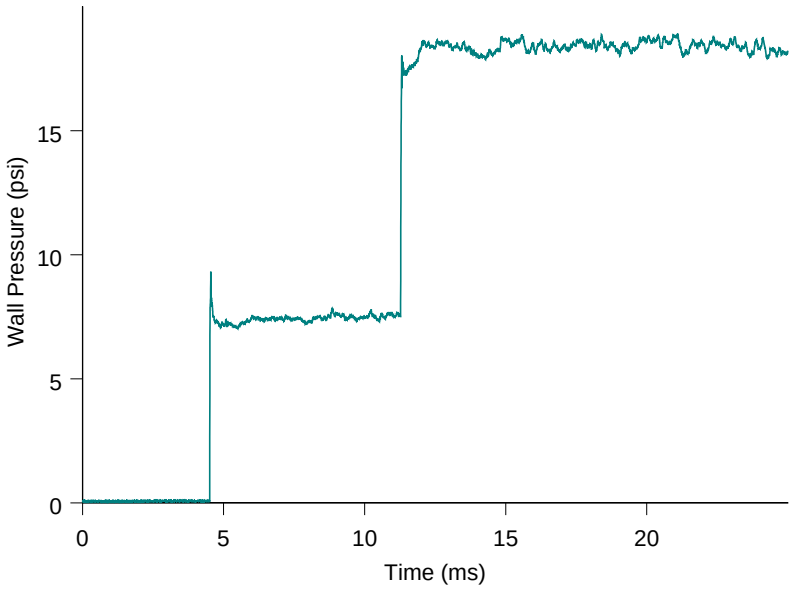

Figure 2-9: Wall Pressure Signal

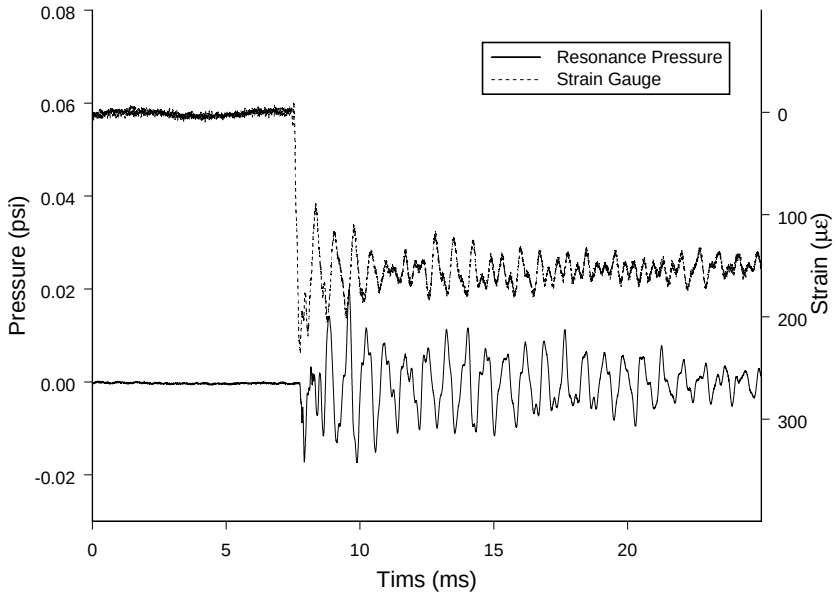

Figure 2-10: Signal of strain gage #1 and resonance pressure signal in the case of aluminum plate

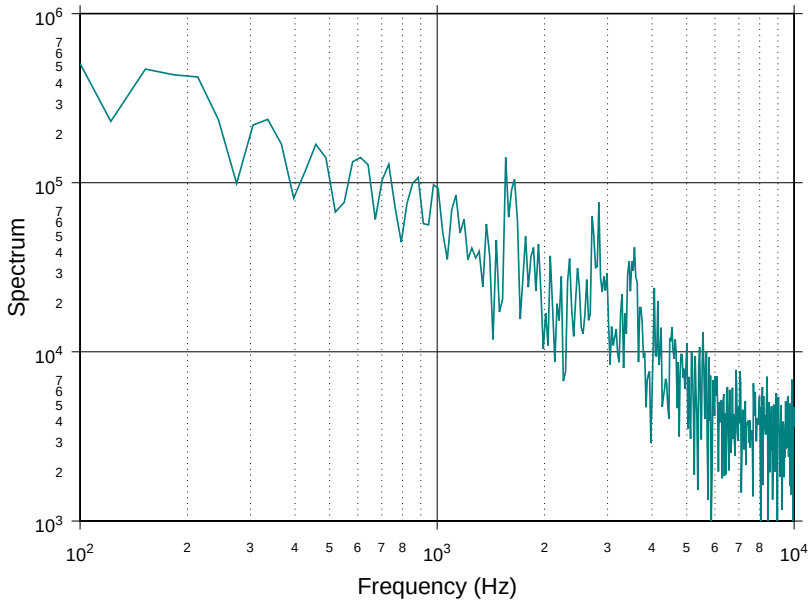

Figure 2-11: Spectrum of strain gage #1 signal on aluminum plate.

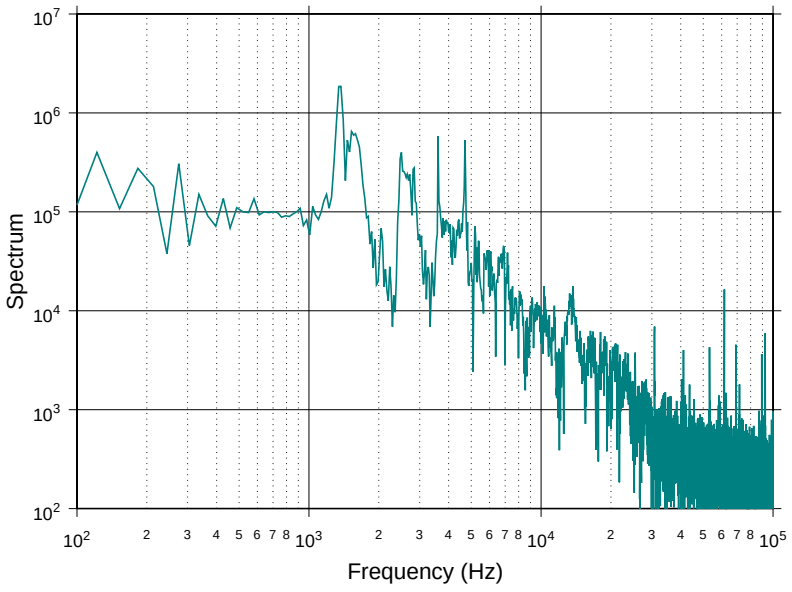

Figure 2-12: Frequency spectrum of the pressure excited by the reverberating aluminum plate

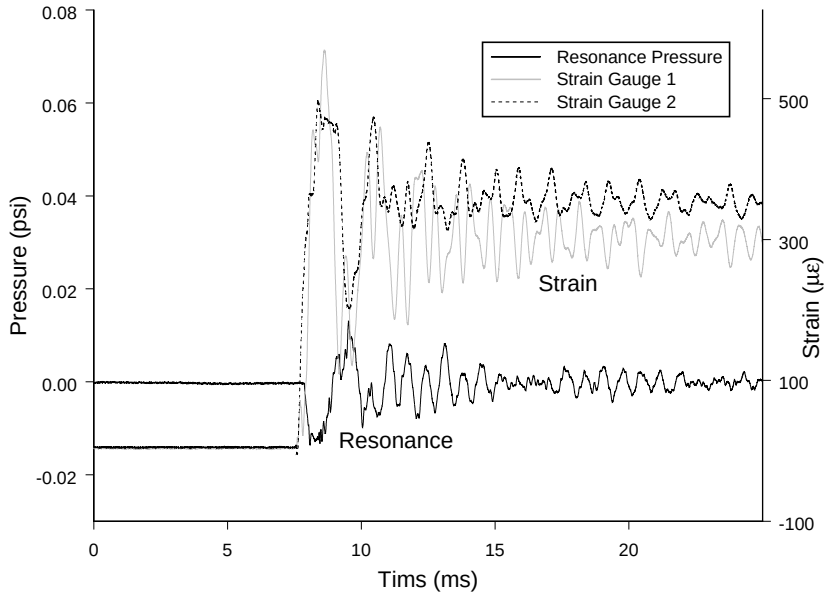

Figure 2-13: Signals of strain gage #1 #2 and resonance pressure signal in the case of stainless-steel plate

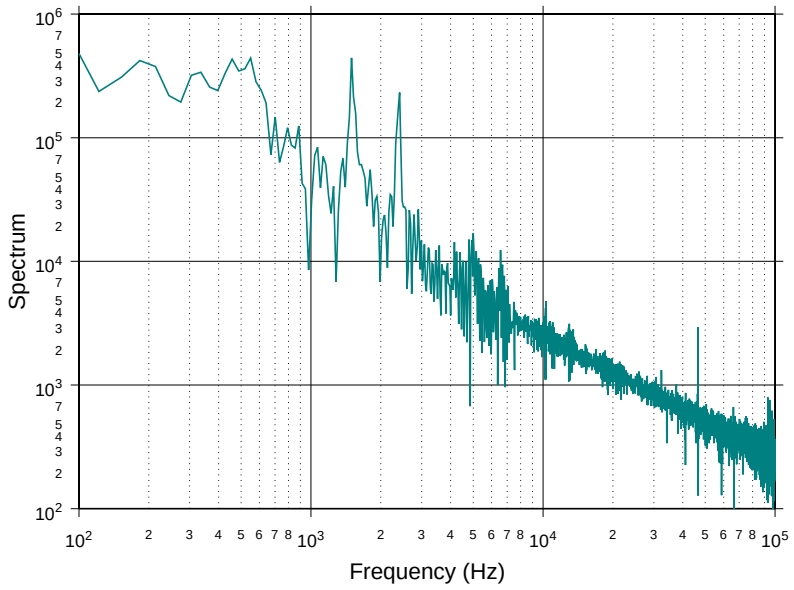

Figure 2-14: Spectrum of strain gage signal #1 on stainless-steel plate.

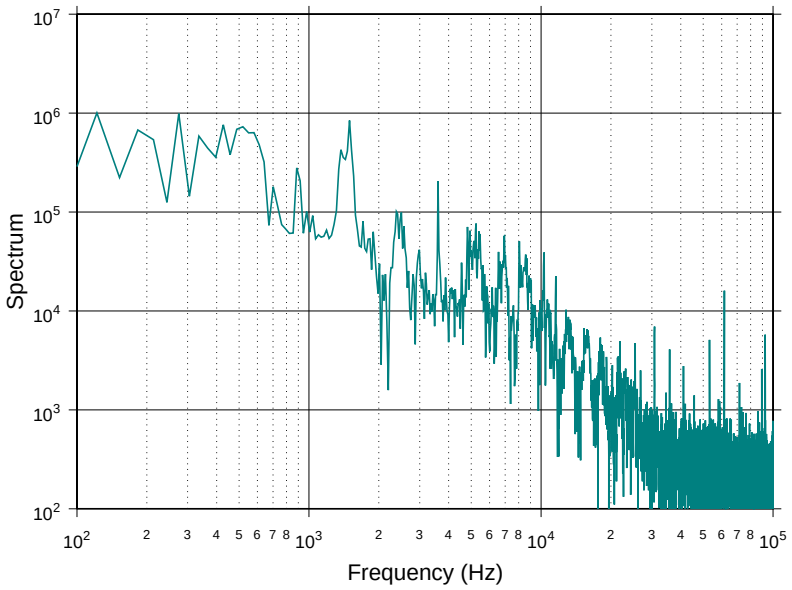

Figure 2-15: Frequency spectrum of the pressure excited by the reverberating stainless-steel plate

frequencies shown in the spectrum of strain are also present in the spectrum of resonance pressure. It is also observed that there exists several extra peaks in the resonance signal power spectrum, they may belong to the subharmonic and high harmonic of the acoustic excitation as suggested in [21].

The signals of strain and resonance pressure in the case of the stainless steel plate are shown in Figure 2-13. Strain gage #1 and #2 is under tension in this case as there are closer to the center of the plate, thus these strains are positive. Periodicity is also evident in the signals. Power spectrum of the signals are shown in Figures 2-14 and 2-15.

In the case of plates made of composite materials, the signals, shown in Figure 2-16, are considerably "cleaner" than in the cases of steel or aluminum plates. Both strains are negative in this case as both strain gages are mounted near the edge of the plate and compression is expected at the exterior side of the plate. The spectra shown in Figure 2-17 indicate one major peak at 400Hz. The spectrum of the resonance pressure, however, shows

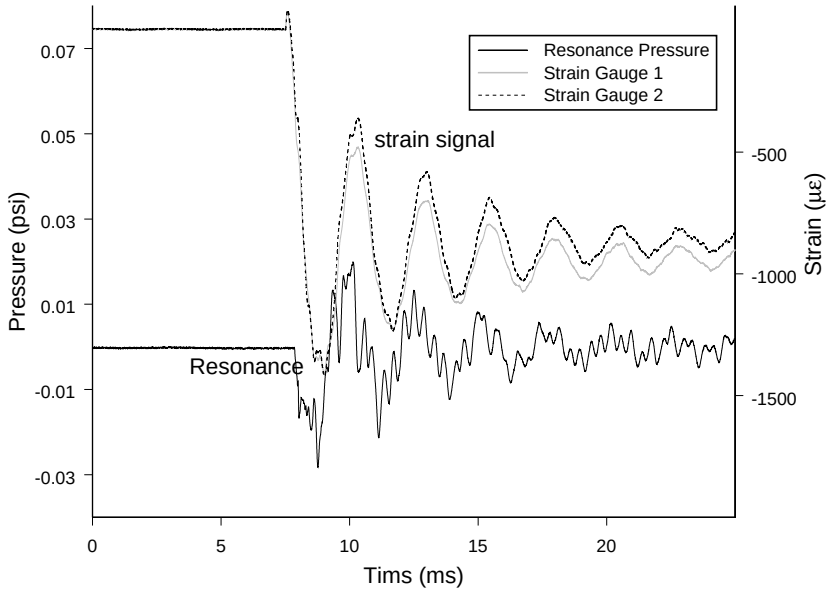

Figure 2-16: Signals of strain gage #1 #2 and resonance pressure signal in the case of composite plate

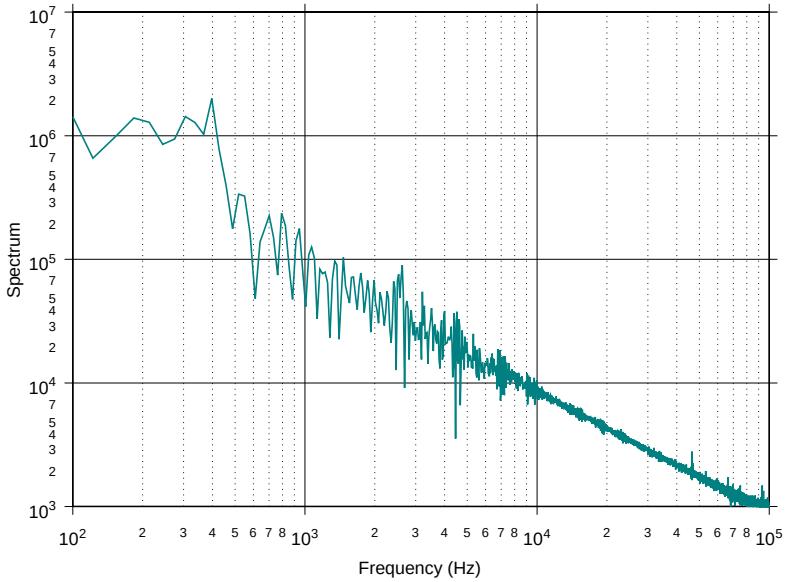

Figure 2-17: Spectrum of strain gage signal #1 on composite plate.

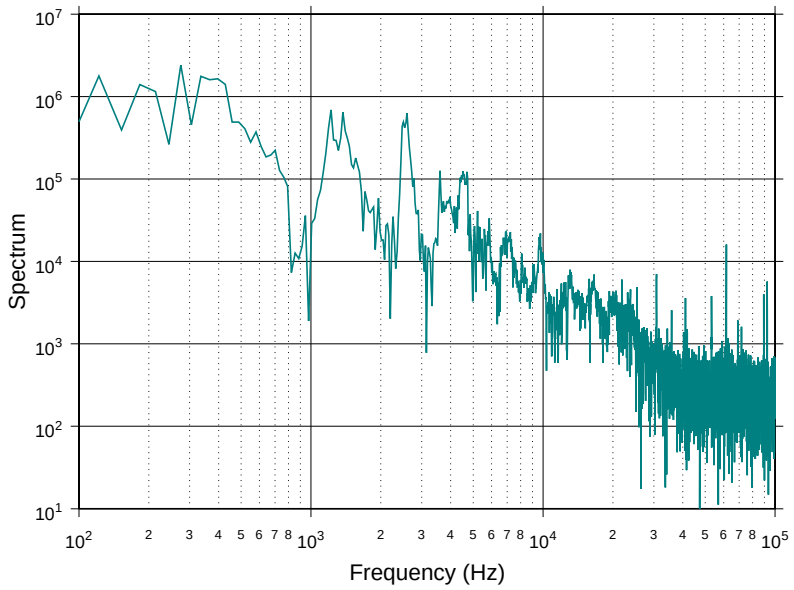

Figure 2-18: Frequency spectrum of the pressure excited by the reverberating composite plate

several major peaks, indication of presence of several modes in the signal. This is also evident in the signals shown in Figure 2-18 where the strain signals showing a periodicity with frequency of 400Hz, while the resonance pressure signal contains this frequency as well as higher ones. It is yet unclear where these higher frequency components originate from.

Two strain gages, located at the same radial distance from the center were used in this experiment with the composite plate. One gage, however, was rotated 45^o to the direction of the local radius. The fact that the signals of the two strain gages are identical indicates that this 10-layer composite has a quasi-isotropic behavior.

It is obvious from the above experiments that the impact of the shock sets the plate in motion, which then excites waves in the other side. The amplitude of the waves is quite large, 0.04 psi (143dB) indicating that it maybe stronger than a simple sound wave. The frequency spectrum of the pressure signal has peaks at the same frequencies as the spectrum

of the stain. This provides evidence that the pressure is induced by the motion of the plate triggered by the shock impact on the other side.

2.3.2 Conclusion

Strain and pressure signals was acquired in the current experimental investigation and complicate wave phenomena were observed in both fluid and structure. Experimental result shows that plates made of different material exhibits distinct modal response when subject to shock wave loading. The experiments with composite plates indicated that the shock impact results in one dominant mode of waves only which may indicate that it may caused by mechanism that do not play any role in the metallic plate. Although the strain field indicates considerable damping of several of the modes, all modes were observed in the acoustic resonance signal. It is also observed that there exists several extra peaks in the resonance signal power spectrum, they may belong to the subharmonic and high harmonic of the acoustic excitation. Such acoustic excitation is non-linear and further investigation is needed in order to better understand this behavior. Damping of the plate vibration in time was also observed on all plates during the interaction but the mechanism is still not yet known. It is still not determined whether such damping is mainly caused by the acoustic excitation or the material's viscoelastic behavior.

2.4 Shock Wave Impact on Non-isotropic Plates

Several experiments using composite plates with various properties were also carried out. The experimental arrangement is the same as described above. The composite plates used are shown in table 2.2. The strain gage locations are shown on Figure 2-19. The power spectrums of the strain and reverberating signals are shown in Figure 2-20 through 2-34. Periodicity is evident in these signals and all strain signals posses a peak at around 900Hz. However, because the composite plate used in these experiment is no longer isotropic, the magnitude of these peaks is directional dependent. It is also worth to mention that the

Plate	Laminates	Thickness (inch)	Diameter (inch)	Density ($10^3 kg/m^3$)	Youngs Modulus (0^o direction) Gpa
1	$[0]_1 2$	1/8”	14.5”/12”	1.72	65.1
2	$[0, 90]_6$	1/8”	14.5”/12”	1.72	38.9
3	$[0, 45, -45, 90]_3$	1/8”	14.5”/12”	1.72	29.6

Table 2.2: Composite plate dimensions and material properties

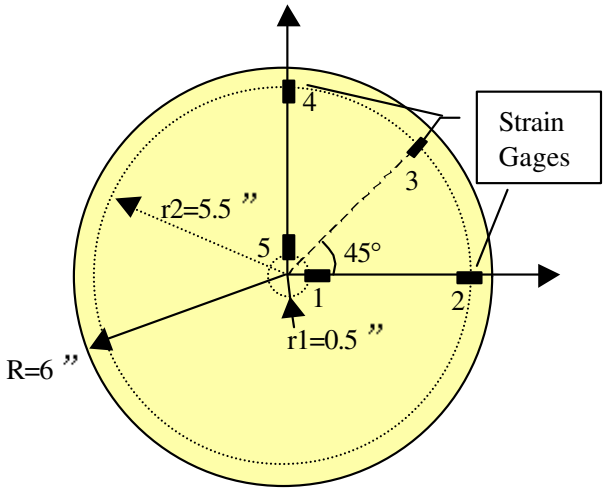

Figure 2-19: Strain Gages Locations on all Composite Plates.

resonance spectrum in these experiments all have major peaks around 1300Hz, even though this is not always the dominate frequency among the strain signals. It is possible that such behavior maybe related to the non-linear behavior of the vibrating composite plates. It also has to be mentioned that the Young’s modulus of all composite plates is smaller than that of the aluminium plates, which means that the plates vibration magnitude caused by same shock loading is larger compared with the experiments with aluminum, again this may intensify the non-linear effects on the plate deformation, acoustic pressure excitation and transfer.

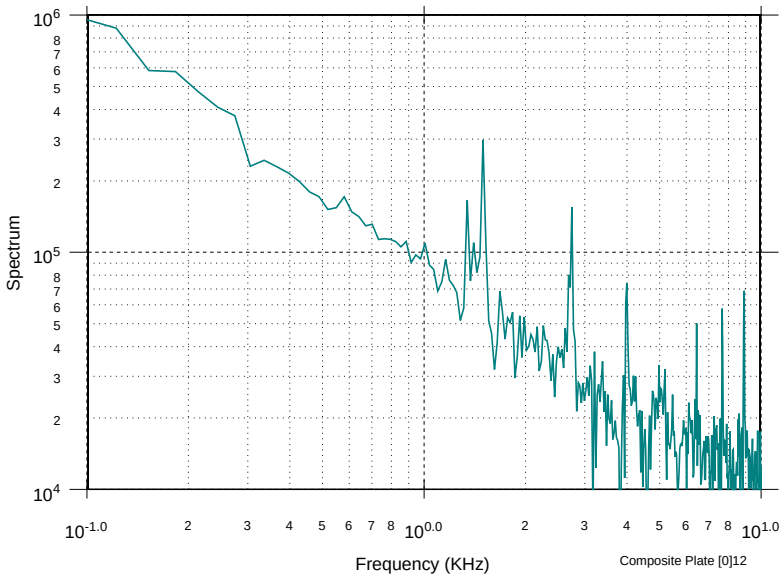

Figure 2-20: Resonance Spectrum of a Composite Plate $[0]_{12}$

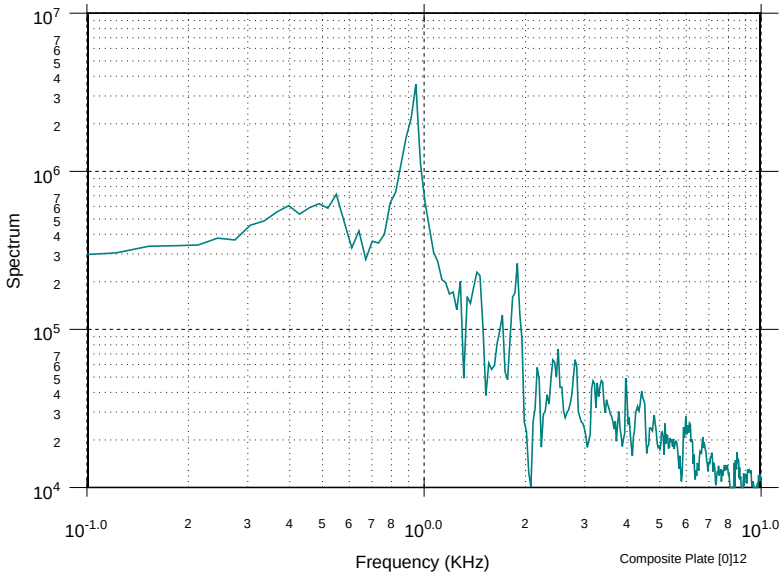

Figure 2-21: Strain Signal Spectrum 2 of a Composite Plate $[0]_{12}$

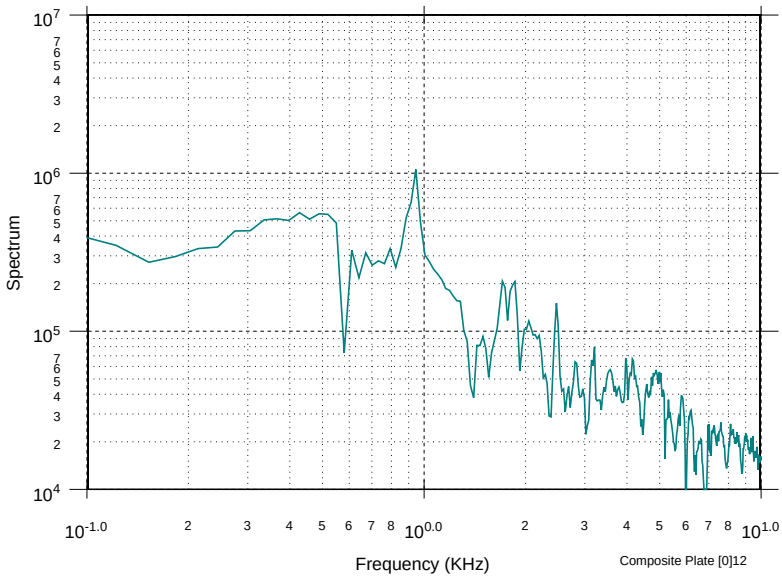

Figure 2-22: Strain Signal Spectrum 3 of a Composite Plate $[0]_{12}$

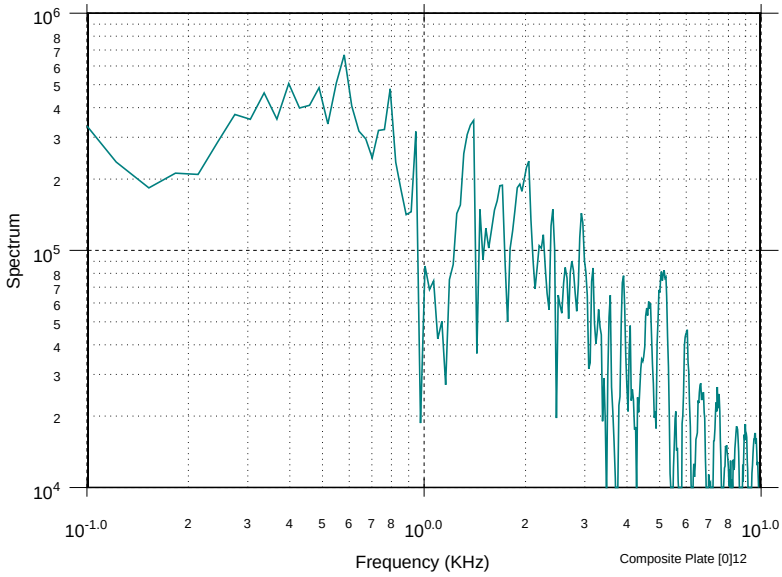

Figure 2-23: Strain Signal Spectrum 4 of a Composite Plate $[0]_{12}$

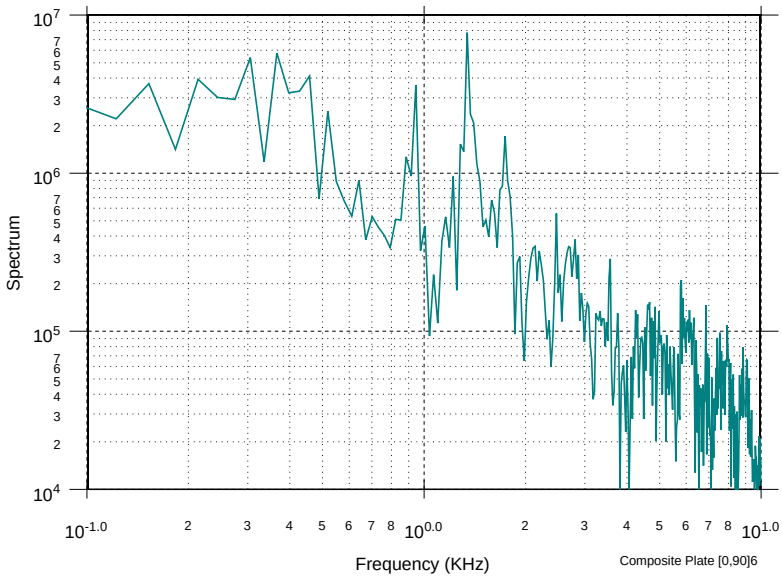

Figure 2-24: Resonance Spectrum of a Composite Plate $[0, 90]_6$

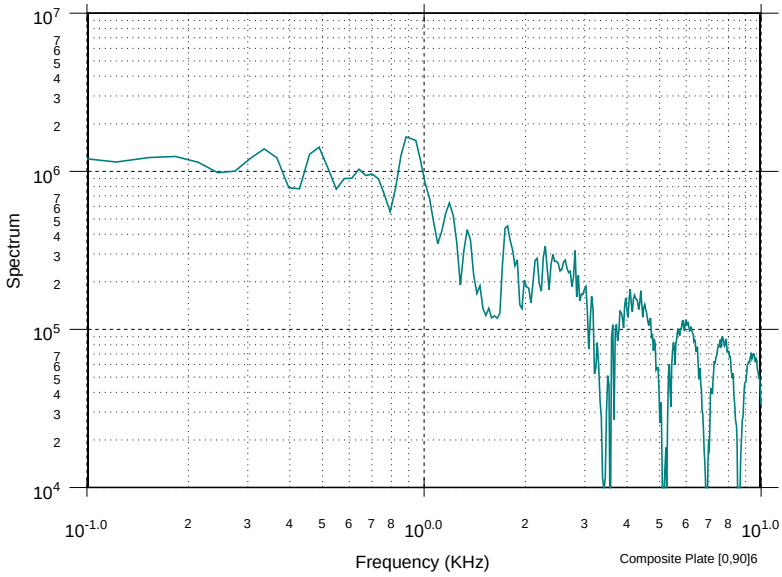

Figure 2-25: Strain Signal Spectrum 1 of a Composite Plate $[0, 90]_6$

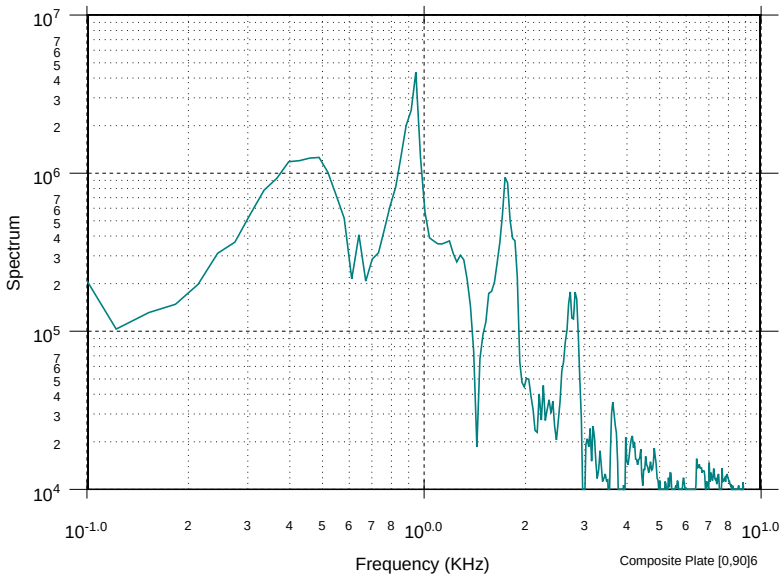

Figure 2-26: Strain Signal Spectrum 2 of a Composite Plate $[0, 90]_6$

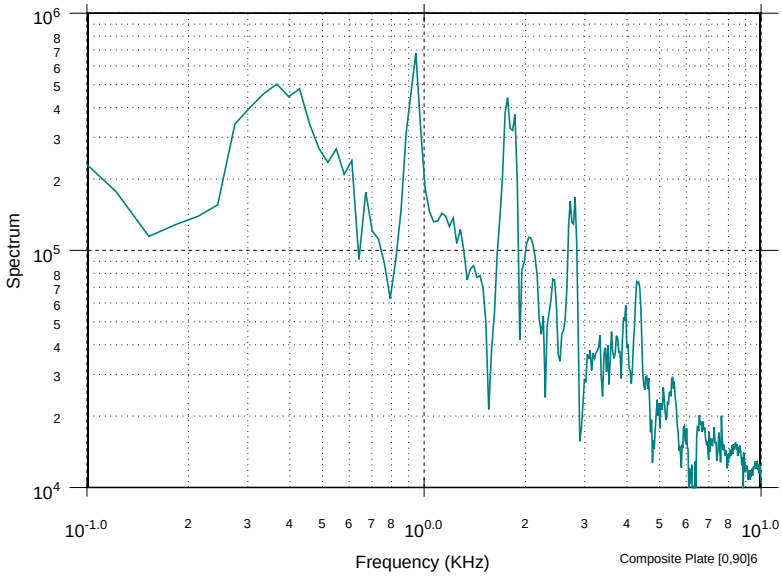

Figure 2-27: Strain Signal Spectrum 3 of a Composite Plate $[0, 90]_6$

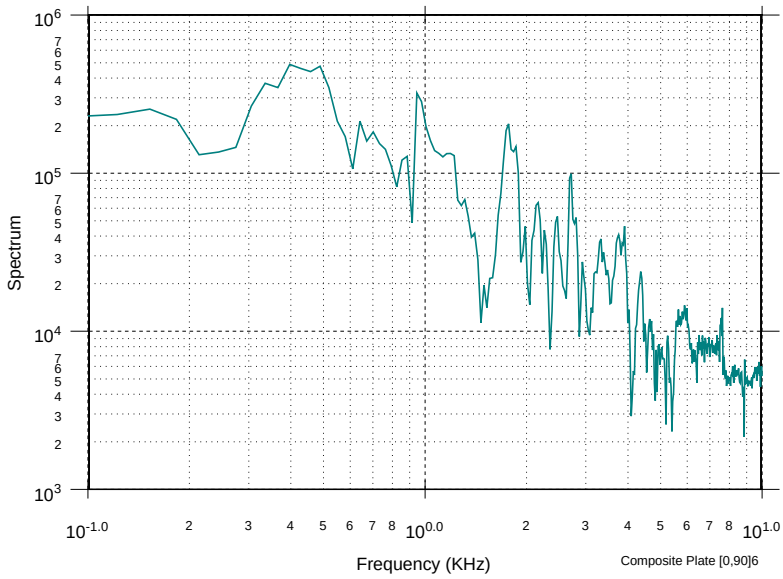

Figure 2-28: Strain Signal Spectrum 4 of a Composite Plate $[0, 90]_6$

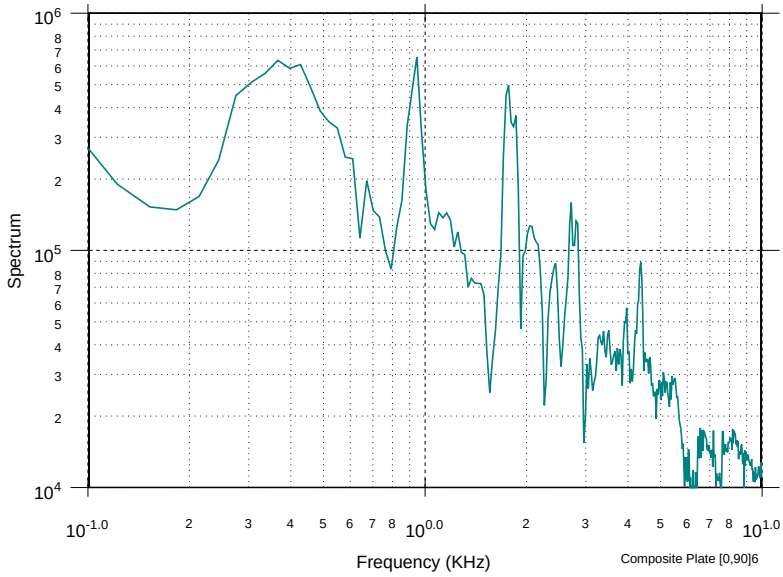

Figure 2-29: Strain Signal Spectrum 5 of a Composite Plate $[0, 90]_6$

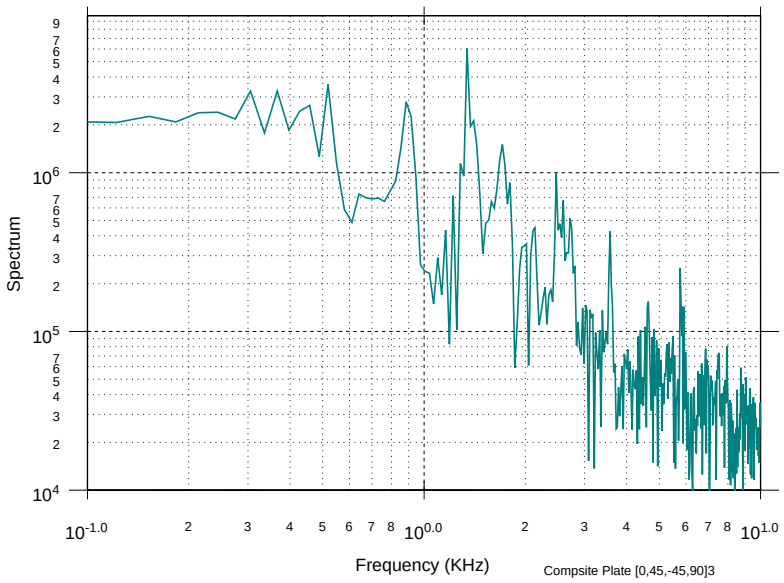

Figure 2-30: Resonance Spectrum of a Composite Plate $[0, 45, -45, 90]_3$

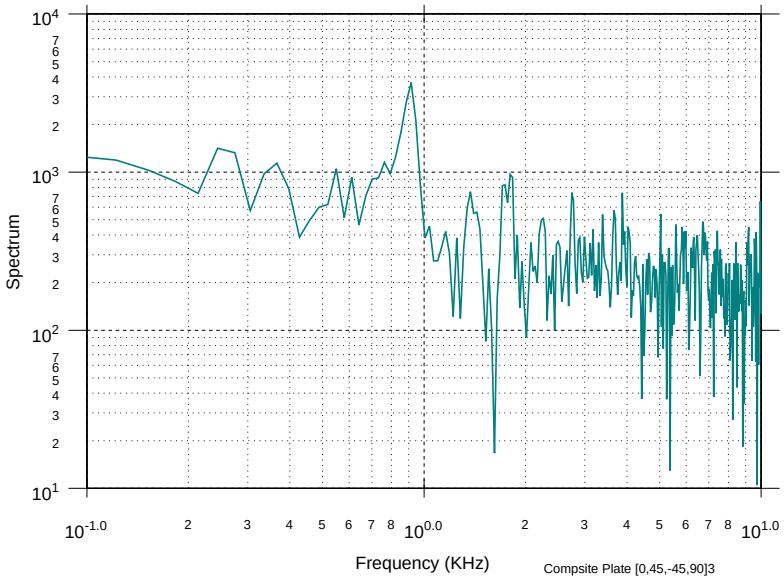

Figure 2-31: Strain Signal Spectrum 2 of a Composite Plate $[0, 45, -45, 90]_3$

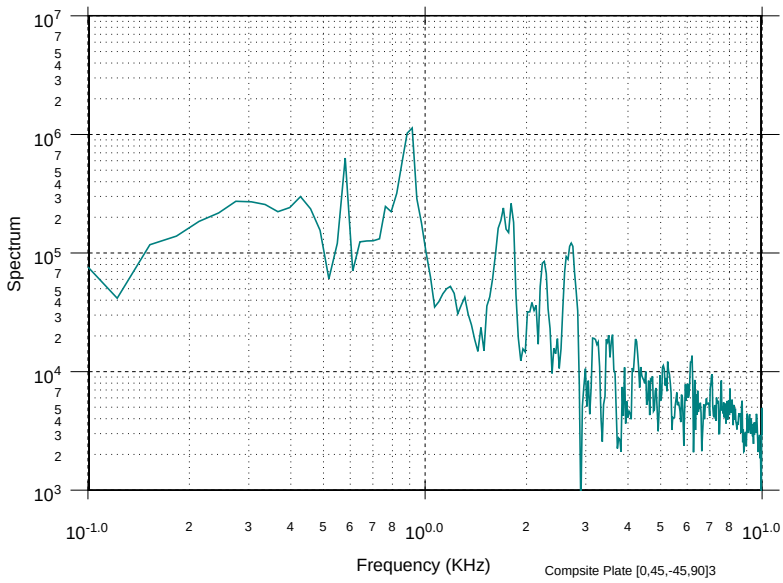

Figure 2-32: Strain Signal Spectrum 3 of a Composite Plate $[0, 45, -45, 90]_3$

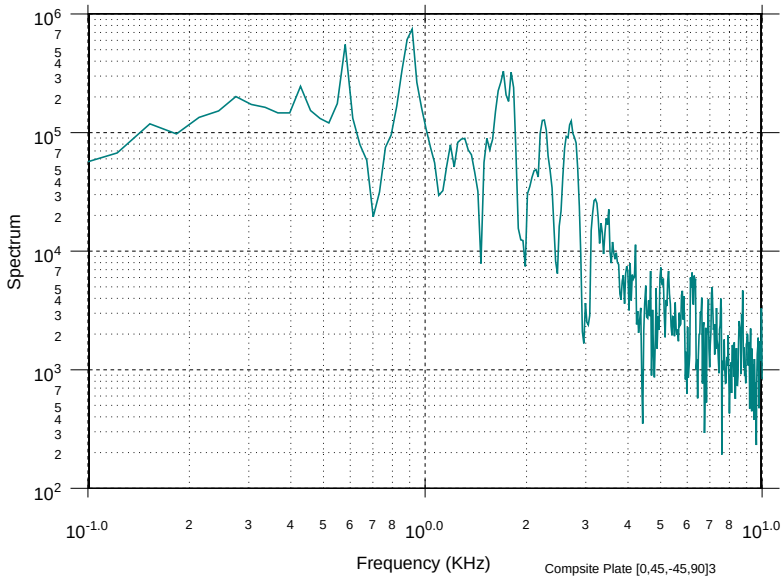

Figure 2-33: Strain Signal Spectrum 4 of a Composite Plate $[0, 45, -45, 90]_3$

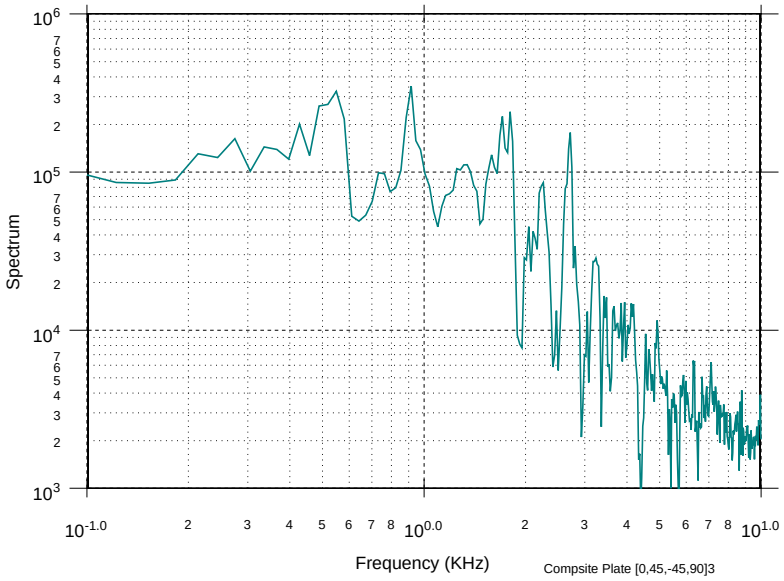

Figure 2-34: Strain Signal Spectrum 5 of a Composite Plate $[0, 45, -45, 90]_3$

Chapter 3

Modal Analysis

3.1 Forced Axisymmetric Motions of Circular Elastic Plates

In this section the mathematical model of an axisymmetric elastic thin plate subjected to shock wave loading is presented. The plate is modelled by the Poisson-Kirchoff plate theory [51]. A time dependent solution is obtained by modal superposition and it was later employed to model the dynamic response of a plate subject to shock wave loading.

3.1.1 Poisson-Kirchoff Formulation

Equation of motion

The partial differential equation of motion for the axisymmetrically loaded isotropic plate,shown in Figure 3-1, can be expressed as:

$$\nabla^4 w(r,t) + \frac{m}{D}\frac{\partial^2 w(r,t)}{\partial t^2} = \frac{p(r,t)}{D} \tag{3.1}$$

where,

$w(r,t)$ is the transverse deflection of plate;

h is the thickness of the plate as shown in Figure 3-1;

m is the mass per unit area of plate;

D is the flexural rigidity of plate, $D = \frac{Eh^3}{12(1-\nu^2)}$, with E and ν as the Young's modulus and Poisson's ratio, respectively;

$p(r,t)$ is pressure loading on the plate.

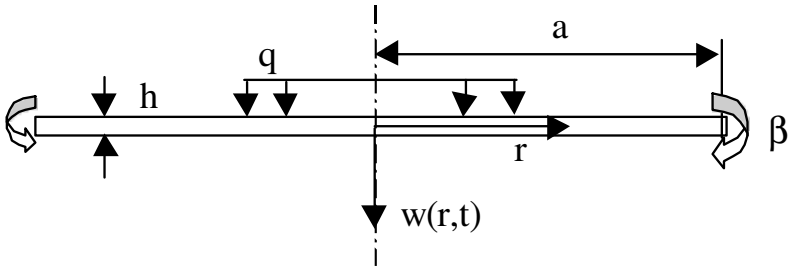

Figure 3-1: An axisymmetrically loaded plate.

We assume that in-plane forces are small compared to the forces in the normal direction of the plate because of the large amplitude of shock wave loading. As a result transverse shear stresses are ignored when the plate is undergoing small deflection.

Boundary Conditions

1. $w(0,t)$ must be finite
2. $\frac{\partial w(0,t)}{\partial r} = 0$
3. $w(a,t) = 0$, a is the radius of plate.
4. $-D[\frac{\partial^2 w(a,t)}{\partial r^2} + \frac{\nu}{a}\frac{\partial w(a,t)}{\partial r}] = \beta\frac{\partial w(a,t)}{\partial r}$, where β is the edge spring constant of proportionality.

Initial Conditions

1. $w(r,0) = 0$
2. $\frac{\partial w(r,0)}{\partial t} = 0$

These initial conditions indicate that initially the plate has no deflection and is at rest.

3.1.2 Solution

Introducing the dimensionless quantities $\rho = r/a$ and $\eta = w/a$, equation 3.1 becomes:

$$\nabla^4\eta(\rho,t) + \frac{ma^4}{D}\frac{\partial^2\eta(\rho,t)}{\partial t^2} = \frac{a^3p(\rho,t)}{D} \tag{3.2}$$

The third and fourth boundary conditions become:

- 3. $\eta(1,t) = 0$ at the edge of the plate;
- 4.

$$-D[\frac{\partial^2\eta(\rho,t)}{\partial\rho^2} + \nu\frac{\partial\eta(\rho,t)}{\partial\rho}] = a\beta\frac{\partial\eta(\rho,t)}{\partial\rho} \tag{3.3}$$

at $\rho = 1$.

Homogeneous Solution

First, the eigenfunctions for the homogeneous equation are determined for the elastically built-in plate. Setting $p(\rho,t) = 0$ in equation 3.2 and assuming separable solutions in the form

$$\eta(\rho,t) = R(\rho)e^{i\Omega t} \tag{3.4}$$

The ordinary differential equation resulting is:

$$[(\frac{d^2}{d\rho^2} + \frac{1}{\rho}\frac{d}{d\rho})^2 - \frac{ma^4}{D}\Omega^2]R(\rho) = 0 \tag{3.5}$$

The general solution of the above equation may be written as

$$R(\rho) = C_0J_0(\kappa\rho) + C_1Y_0(\kappa\rho) + C_2I_0(\kappa\rho) + C_3K_0(\kappa\rho) \tag{3.6}$$

where

$\kappa^2 = a^2(\frac{m}{D})^{1/2}\Omega$

J_0 is the Bessel functions of the first kind; Y_0 is Bessel functions of the second kind; I_0 is the modified Bessel function of the first kind; K_0 is the modified Bessel function of the second kind.

C_{0-3} are constants dependent on the boundary conditions and yet to be determined.

C_1 and C_3 must be zero in order to satisfy the first two boundary conditions. Boundary condition 3 is satisfied by selecting C_0 and C_2 as follows:

$$R(\rho) = I_0(\kappa)J_0(\kappa\rho) - J_0(\kappa)I_0(\kappa\rho) \tag{3.7}$$

When the above equation was introduced into boundary condition 4, transcendental equation for the determination of the eigenvalues, κ_i was obtained as:

$$\frac{2\kappa_i}{1 - \frac{\beta a}{D} - \nu} = \frac{J_1(\kappa_i)}{J_0(\kappa_i)} + \frac{I_1(\kappa_i)}{I_0(\kappa_i)} \tag{3.8}$$

The dimensionless ration $\beta a/D$ will be referred to as the edge fixity parameter.

Formal solution-Forced Motions

A series solution for $\eta(\rho, t)$ in equation is assumed in the form of

$$\eta(\rho, t) = \sum R_j(\rho)g_j(t) \tag{3.9}$$

where

$$R_j(\rho) = I_0(\kappa_j)J_0(\kappa_j\rho) - J_0(\kappa_j)I_0(\kappa_j\rho) \tag{3.10}$$

$g_j(t)$, which depends on the loading function, the structural plate parameters, and boundary conditions, is now to be determined.

Substituting 3.9 into 3.5 and interchanging the order of differentiation and summation

	EI(GP)	$\rho(kg/m^3)$	ν	h	a(inch)
Aluminum Plate	71	2700	0.33	1/8	6
Stainless plate	205	7700	0.3	1/16	6

Table 3.1: Plate properties.

Eigen Frequency	1	2	3	4	5
Aluminum (Hz)	343.6025	1337.676	2996.958	5320.419	8307.896
Stainless steel (Hz)	174.226	678.278	1519.629	2696.757	4212.579

Table 3.2: Eigen frequencies of an aluminum plate and a stainless steel plate.

gives:

$$\sum\{g_j(t)(\frac{d^2}{d\rho^2}+\frac{1}{\rho}\frac{d}{d\rho})^2R_j(\rho)+\frac{ma^4}{D}\frac{d^2g_j(t)}{dt^2}R_j(\rho)\}=\frac{a^3}{D}p(\rho,t) \tag{3.11}$$

Exploiting the fact that $R_j(\rho)$ satisfies the homogeneous equation, the equation above can be reduced to:

$$\sum\{g_j(t)\kappa_j^4+\frac{ma^4}{D}\frac{d^2g_j(t)}{dt^2}\}R_j(\rho)=\frac{a^3}{D}p(\rho,t) \tag{3.12}$$

Multiplying both sides of the above equation by $\rho R_i(\rho)d\rho$ and integrating from $\rho = 0 \rightarrow 1$, by virtue of the orthogonality property, we can obtain:

$$\{\frac{d^2g_j(t)}{dt^2}+\frac{\kappa_j^4D}{ma^4}g_j(t)\}N_{ij}=\frac{1}{ma}\int_0^1\rho p(\rho,t)R_i(\rho)d\rho \tag{3.13}$$

where N_{ij} is:

$$N_{ij}=\{\frac{1}{2}[I_0^2(\kappa_j)J_1^2(\kappa_j)-J_0^2(\kappa_j)I_1^2(\kappa_j)]-\frac{1+\nu+\frac{\beta a}{D}}{1-\nu-\frac{\beta a}{D}}I_0^2(\kappa_j)J_0^2(\kappa_j)\}\delta_{ij} \tag{3.14}$$

3.1.3 Numerical Evaluation

The eigen frequencies of the plate were obtained by numerically evaluating the above relations in a C++ program. Table 3.2 shows the typical values for an aluminum plate and a stainless steel plate calculated with the properties shown in Table 3.1:

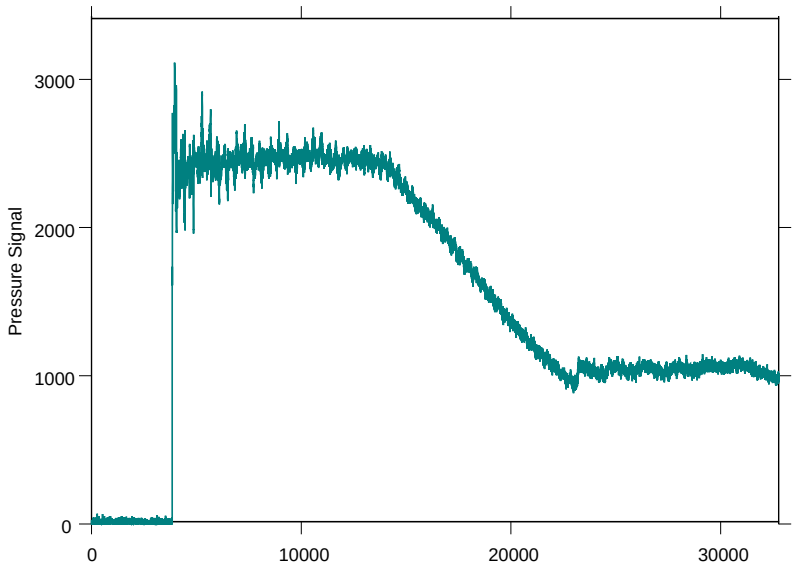

Figure 3-2: Pressure signal used for numerical evaluation.

Attempts have also been made using Equation 3.14 to simulate the response of a plate subject to a shock wave impact loading. The raw pressure history obtained by experiment is shown in Figure 3-2. In the experiment this pressure signal was measure from a pressure transducer mounted on the center of the plate. The corresponding raw strain signal from one strain gage near center at $r = 0.5$" is shown in Figure 3-3.

The numerical results obtained by using equation 3.14 are presented in Figure 3-4 We can see that this result is significantly different from the experiment. This may be caused by the following:

- Equation 3.14 is the solution of 3.1, which neglects the damping effect. However, experiment data shows that damping plays a substantially important role in this problem. Thus a new mathematical model which considers the damping effect is required for an appropriate approach to this problem.

- The signal in Figure 3-4 shows that the displacement is mostly consisted by the first

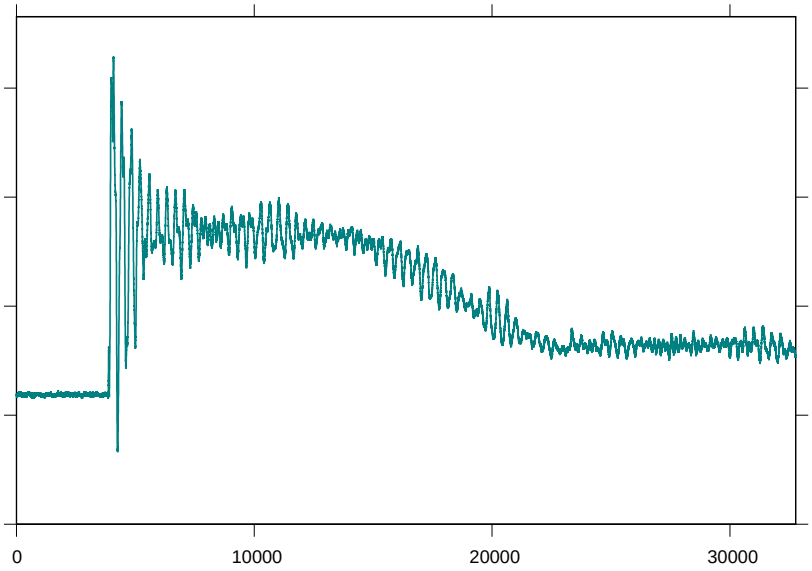

Figure 3-3: Strain-time history obtained by experiment

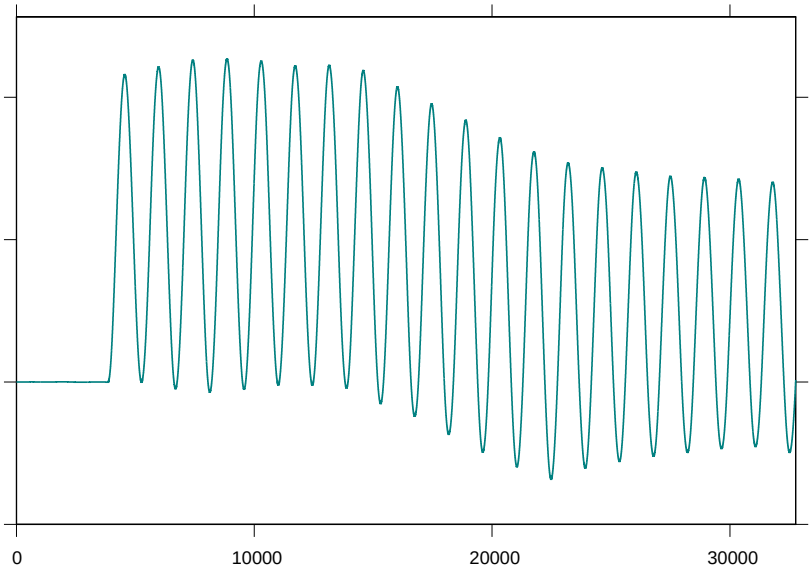

Figure 3-4: Strain-time history obtained from equation 3.14

mode of the plate. The numerical evaluation also shows that the second mode of the vibration is of a magnitude of 1/100th of the first mode. However, experiments show that the first mode is somehow suppressed and its amplitude is of the same order as the second mode.

3.2 Coupled Fluid Structure Vibration Modal Analysis

3.2.1 Finite Element Method

The problem of free vibrating plate coupled with fluid can be analyzed using Finite Element Method, where the structure and fluid matrix equations were merged together and then solved [50], [45] .

In finite element form, the discrete structural problem of a vibrating plate can be described by:

$$[\mathbf{K}]\{\mathbf{u_i}\} + [\mathbf{C}]\frac{\partial\{\mathbf{u}_i\}}{\partial t} + [\mathbf{M}]\frac{\partial^2\{\mathbf{u_i}\}}{\partial t^2} - \frac{1}{\rho_F}[\mathbf{Q}]\{\mathbf{p_i}\} + \{\mathbf{R}\} = 0 \tag{3.15}$$

where

$[\mathbf{K}]$ is the stiffness matrix;

$[\mathbf{C}]$ is the matrix of viscous damping terms;

$[\mathbf{M}]$ is the mass matrix;

$\{\mathbf{R}\}$ is the external forcing function;

$[\mathbf{u}_i]$ is the structure displacement vector;

ρ_F is the density of the fluids;

$\{\mathbf{p}_i\}$ is the fluid's pressure vector;

$-\frac{1}{\rho_F}[\mathbf{Q}]\{\mathbf{p_i}\}$ is the fluid structure coupling term, which is caused by the pressure specified on the fluid-structure boundary.

$$[\mathbf{Q}] = \sum[q] \tag{3.16}$$

$$[q] = \int_S \rho_F[\mathbf{S}]^T(-\mathbf{n}_s)[\mathbf{N}]dS = \int_S \rho_F[\mathbf{S}]^T\mathbf{n}[\mathbf{N}]dS \tag{3.17}$$

here $[\mathbf{N}]$ is the shape functions for the fluid element; $[\mathbf{S}]$ is the shape function of the structure; dS is the elemental area at fluid-plate interface; p is pressure and defined positive as compression. On the fluid-structure interface, we have

$$-p\mathbf{n}_s = p\mathbf{n}$$

$\mathbf{n}_s$ and $\mathbf{n}$ are surface outward normals to the solid and fluid, respectively.

For free vibrations without damping, Equation 3.15 reduces to

$$[\mathbf{K}]\{\mathbf{u_i}\} + [\mathbf{M}]\frac{\partial^2\{\mathbf{u_i}\}}{\partial t^2} - \frac{1}{\rho_F}[\mathbf{Q}]\{\mathbf{p_i}\} = 0 \tag{3.18}$$

The following wave equation for the non-viscous, compressible fluid is used to represent the motion of the fluid:

$$\nabla^2 p - \frac{1}{c^2}\frac{\partial^2 p}{\partial t^2} = 0 \tag{3.19}$$

where

p is the pressure in the fluid

c is the sound speed of the fluid, i.e., the propagation speed of small disturbance waves in the fluid.

Using the calculus of variations, this above wave equation can be expressed in discrete finite element form as:

$$[\mathbf{H}]\{\mathbf{p}_i\} - [\mathbf{G}]\frac{\partial^2\{\mathbf{p}_i\}}{\partial t^2} + [\mathbf{Q}]^T\frac{\partial^2\{\mathbf{u}_i\}}{\partial t^2} = 0 \tag{3.20}$$

where,

$\{\mathbf{p}_i\}$ is vector of fluid nodal pressure caused by structure vibration;

$\{\mathbf{u}_i\}$ is vector of structure nodal displacement;

$[\mathbf{H}]$ is in a form similar to the stiffness matrix of the structure, it may be considered as the fluid's virtual stiffness matrix;

$$[\mathbf{H}] = \sum [h] \tag{3.21}$$

$$[h] = \int_{vol} \left\{ \frac{\partial [\mathbf{N}]^T}{\partial x} \frac{\partial [\mathbf{N}]}{\partial x} + \frac{\partial [\mathbf{N}]^T}{\partial y} \frac{\partial [\mathbf{N}]}{\partial y} + \frac{\partial [\mathbf{N}]^T}{\partial z} \frac{\partial [\mathbf{N}]}{\partial z} \right\} dV \tag{3.22}$$

$[\mathbf{N}]$ is the shape functions for the fluid element.

$[\mathbf{G}]$ is in a form similar to the mass matrix of the structure, it may be considered as the fluid's virtual mass matrix.

$$[\mathbf{G}] = \sum [g] \tag{3.23}$$

$$[g] = \frac{1}{c^2} \int_{vol} [\mathbf{N}]^T [\mathbf{N}] dV \tag{3.24}$$

where c is the speed of sound as described before;

$[\mathbf{Q}]^T \frac{\partial^2 \{\mathbf{u}_i\}}{\partial t^2}$ is the fluid structure coupling term, which is the pressure force acting in the surface normal direction on the fluid-structure interface,

$$[\mathbf{Q}] = \sum [q] \tag{3.25}$$

$$[q] = \int_S \rho_F [\mathbf{S}]^T \mathbf{n} [\mathbf{N}] dS \tag{3.26}$$

where ρ_F is the density of the fluid; $[\mathbf{S}]$ is the shape function of the structure element; $\mathbf{n}$ is the fluid outward surface normal; Note that when deriving this coupling force

term, the relationship

$$\frac{\partial p}{\partial n} = -\rho_F \dot{v}_n = -\rho_F \mathbf{n}^T \cdot \frac{\partial^2 \mathbf{u}}{\partial t^2} \tag{3.27}$$

is used, where v_n is the fluid velocity at the fluid structure interface boundary, caused by the motion of the structure, which is then described by $\mathbf{n}^T \dot{\mathbf{u}}$. The underlying assumptions in this relationship are that the fluid is under very small disturbance such that the convection term can be neglected; and the density of the fluid ρ_F varies by a small amount only so it may considered constant.

In the integral above, dS is the elemental area at fluid-plate interface and dV is the element volume.

If the fluid-structure vibrates with simple harmonic motion, we can assume that the vector of nodal acoustic pressure $\{\mathbf{p}_i\}$ and the vector of nodal displacements $\{\mathbf{u}_i\}$ is given by:

$$\{\mathbf{p_i}\} = \{\mathbf{p_0}\} \cos \omega t$$

and

$$\{\mathbf{u_i}\} = \{\mathbf{u_0}\} \cos \omega t$$

Coupling Equation 3.18 and 3.20 leads to the following sets of simultaneous equations:

$$\begin{bmatrix} [\mathbf{K}] & -[\mathbf{Q}]^T]/\rho_F \\ [0] & [\mathbf{H}] \end{bmatrix} \begin{bmatrix} \mathbf{u_0} \\ \mathbf{p_0} \end{bmatrix} - \omega^2 \begin{bmatrix} [\mathbf{M}] & [0] \\ [\mathbf{Q}] & [\mathbf{G}] \end{bmatrix} \begin{bmatrix} \mathbf{u_0} \\ \mathbf{p_0} \end{bmatrix} = 0 \tag{3.28}$$

where ω is radian frequency. The solution of Equation 3.28 is not convenient because it is unsymmetrical. However, we can rearranging Equation 3.28 using the bottom row of the equation:

$$\{\mathbf{p_0}\} = [\mathbf{H}]^{-1} \omega^2 ([\mathbf{G}]\{\mathbf{p}_0\} + [\mathbf{Q}]\{\mathbf{u}_0\})$$

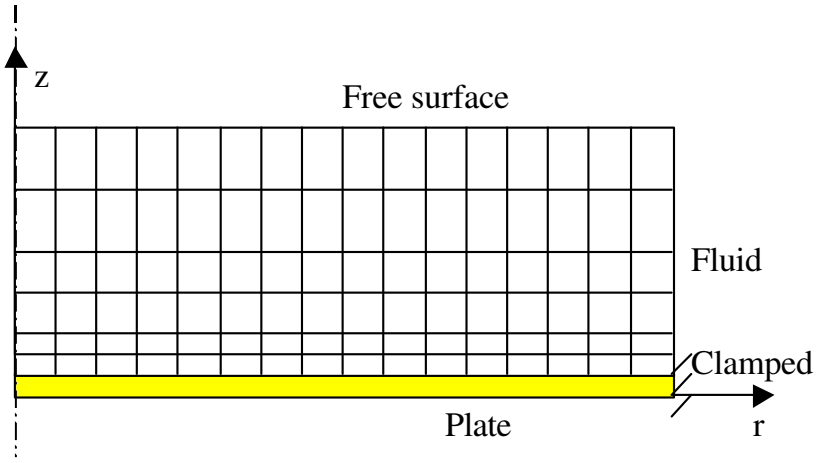

Figure 3-5: Numerical simulation of a vibrating plate.

The symmetrical form of Equation 3.28 is:

$$\left\{ \begin{bmatrix} \rho_F[\mathbf{K}] & [0] \\ [0] & [\mathbf{G}] \end{bmatrix} - \omega^2 \left[\begin{array}{c|c} \rho_F[\mathbf{M}] + [\mathbf{Q}]^T[\mathbf{H}]^{-1}[\mathbf{Q}] & [\mathbf{Q}]^T[\mathbf{H}]^{-1}[\mathbf{G}] \\ \hline [\mathbf{G}][\mathbf{H}]^{-1}[\mathbf{Q}] & [\mathbf{G}][\mathbf{H}]^{-1}[\mathbf{G}] \end{array}\right] \right\} \begin{bmatrix} \mathbf{u_0} \\ \mathbf{p_0} \end{bmatrix} = 0 \tag{3.29}$$

Considering the case for incompressible fluid, $[\mathbf{G}]$=0, Equation 3.29 becomes

$$\rho_F[\mathbf{K}] - \omega^2(\rho_F[\mathbf{M}] + [\mathbf{Q}]^T[\mathbf{H}]^{-1}[\mathbf{Q}]) = 0 \tag{3.30}$$

where

$$\frac{1}{\rho_F}[\mathbf{Q}]^T[\mathbf{H}]^{-1}[\mathbf{Q}] \tag{3.31}$$

is the added virtual mass.

3.2.2 Results

A C++ program is employed to implement the above theory to solve for the natural frequency of a plate vibrating in air. Figure 3-5 shows a circular plate divided into 16 elements with 5 fluid layers. The material properties used in the calculation is listed in previous chapter, Table 2.1. The properties of fluid(Air) used for this computation are:

fluid density $\rho_F = 1.293 kg/m^3$

fluid layer thickness=0.53m.

The result was listed and compared in Table 3.3 3.4 3.5 together with other known results obtained from experiment and that from the classical Poisson-Kirchoff plate theory. It is shown that coupled finite element analysis provided predictions closer to measured values than the classical modal analysis. The coupled fluid-structure calculation yields a lower eigen frequency compared with that of non-coupled calculation, which is obvious as a result of the added virtual mass term in the coupled solution.

Modes	1	2	3	4	5
Theoretical Frequency (Hz)	343.6	1338	2997	5320	8308
Frequency result without fluid coupling	348.5	1357	3040	5398	8432
Frequency result with fluid coupling	333.4	1335	3015	5371	8404

Table 3.3: Calculated eigen frequencies of the aluminum plate.

Modes	1	2	3	4	5
Theoretical Frequency (Hz)	174.2	678.3	1519	2698	4213
Frequency result without fluid coupling	173.5	675.5	1514	2687	4198
Frequency result with fluid coupling	168.2	667.7	1504	2676	4185

Table 3.4: Calculated eigen frequencies of the stainless plate.

Modes	1	2	3	4	5
Frequency result without fluid coupling	497.8	1938	4342	7710	12043
Frequency result with fluid coupling	479.5	1911	4310	7673	12002

Table 3.5: Calculated eigen frequencies of the composite plate.

Chapter 4

Coupled Fluid and Structure Solver

4.1 Introduction

The numerical simulation of the blast and structure interaction is essentially a fluid-structure interaction problem similar to the computational aeroelasticity problem, i.e. CAE. Recent advances were reviewed in [38] and [17]. In this section, the three major models pertaining to CAE, namely, flow solver, structure solver and moving mesh algorithm, are studied and thereby suitable models are chosen to simulate the fluid-structure interaction.

4.2 The Governing Equations

4.2.1 The Euler Equations

The Euler Equations define a system of non-linear, hyperbolic, first order conservation laws which describe the flow of a compressible and inviscid fluid. The Euler equations in two dimensions for an arbitrary control volume Ω, fixed in space and bounded by a closed surface $\mathbf{S}$ with the outward vector $d\mathbf{S}$ can be expressed as:

$$\frac{\partial}{\partial t}\int_{\Omega}\mathbf{U}dV = -\int_{\partial\Omega}\mathbf{F}\cdot d\mathbf{S} - \int_{\partial\Omega}\mathbf{G}\cdot d\mathbf{S} \tag{4.1}$$

where the conservative state vector $\mathbf{U}$ and the flux functions $\mathbf{F}$ and $\mathbf{G}$ are defined as

$$\mathbf{U} = \begin{bmatrix} \rho \\ \rho u \\ \rho v \\ \rho e \end{bmatrix}, \quad \mathbf{F} = \begin{bmatrix} \rho u \\ \rho u^2 + p \\ \rho uv \\ (\rho e + p)u \end{bmatrix}, \quad \mathbf{G} = \begin{bmatrix} \rho v \\ \rho uv \\ \rho v^2 + p \\ (\rho e + p)v \end{bmatrix} \tag{4.2}$$

where ρ is the density, u and v are the velocity components, e is the internal energy, and p is the static pressure given by

$$p = (\gamma - 1)[e - ((\rho u)^2 + (\rho v)^2)/2\rho)]. \tag{4.3}$$

The system of equations written above define the conservation laws for mass, momentum and energy.

4.2.2 The Navier-Stokes Equations

The Euler equations 4.1 are actually the Navier Stokes without the viscous term. Similarly the Navier-Stokes equations can be expressed as:

$$\frac{\partial}{\partial t}\int_{\Omega} \mathbf{U} dV = -\int_{\partial\Omega} \mathbf{F} \cdot d\mathbf{S} - \int_{\partial\Omega} \mathbf{G} \cdot d\mathbf{S} + \int_{\partial\Omega} \mathbf{Q_s} \cdot d\mathbf{S} \tag{4.4}$$

The conservative state vector $\mathbf{U}$ and the flux functions $\mathbf{F}$ and $\mathbf{G}$ are defined above in equation 4.2. The viscous term $\mathbf{Q_s}$ is defined as:

$$\mathbf{Q_s} = \begin{Bmatrix} 0 & 0 \\ \tau_{xx} & \tau_{yx} \\ \tau_{xy} & \tau_{yy} \\ \tau_{xx}u + \tau_{xy}v + kT_x & \tau_{yx}u + \tau_{yy}v + kT_y \end{Bmatrix} \tag{4.5}$$

Where T is the temperature and τ_{ij} is the viscous shear stress tensor,

$$\tau_{ij} = \mu[(\partial_i v_j + \partial_j v_i) - \frac{2}{3}(\nabla \cdot \mathbf{v})\delta_{ij}], \tag{4.6}$$

or explicitly

$$\begin{aligned} \tau_{xx} &= \tfrac{2}{3}\mu(2u_x - v_y) \\ \tau_{xy} &= \tau_{yx} = \mu(u_y + v_x) \\ \tau_{yy} &= \tfrac{2}{3}\mu(2v_y - u_x) \end{aligned} \tag{4.7}$$

The coefficients of dynamic viscosity μ and thermal conductivity k are functions of temperature T. Following Sutherland's formula they are taken as, with temperature in Kelvin degrees,

$$\mu = \mu_c(T/T_c)^{3/2}\frac{T_c + S_\mu}{T + S_\mu}, \tag{4.8}$$

$$k = k_c(T/T_c)^{3/2}\frac{T_c + S_k}{T + S_k}, \tag{4.9}$$

where T_c, μ_c and k_c are reference values, and S_μ, S_k are the Sutherland constants, which are characteristics of the gas. For air, we have

$\mu_c, 10^{-6}kg/(sm)$	S_μ, K	$k_c, J/(smK)$	S_k, K
17.16	111	0.0241	194

The Navier-Stokes equations are non-dimensionalized by defining some characteristic constants. We choose the characteristic density ρ_0, length L_0, temperature T_0, velocity $U_0 = (RT_0)^{1/2}$, coefficient of dynamic viscosity $\mu_0 = \mu(T_0)$, coefficient of thermal conductivity $k_0 = k(T_0)$ and the specific heat coefficient under constant pressure $c_{p0} = \gamma R/(\gamma - 1)$. The combination of these values gives two fundamental parameters: *Reynolds number*

$$Re = \frac{\rho U_0 L_0}{\mu_0} \tag{4.10}$$

and *Prandtl number*

$$Pr = \frac{c_{p0}\mu_0}{k_0} \tag{4.11}$$

The dimensionless conservation laws are the same as the dimensional ones, but the coefficients are changed to

$$\mu = \frac{1}{Re} T^{3/2} \frac{1 + S_\mu/T_0}{T + S_\mu/T_0}, \tag{4.12}$$

$$k = \frac{\gamma}{\gamma - 1} \frac{1}{RePr} T^{3/2} \frac{1 + S_k/T_0}{T + S_k/T_0}, \tag{4.13}$$

with the dimensionless equation of state

$$p = \rho T \tag{4.14}$$

and the dimensionless sound speed

$$c = (\gamma T)^{1/2} \tag{4.15}$$

If we set the $\mu = 0$ and $k = 0$ in the Navier-Stokes equations, we can obtain the Euler equations 4.1.

4.3 Finite Volume Method

The Euler equations are written in conservation form. The conservative formulation is very well suited for the Finite Volume Method (FVM) as control volumes are defined and their quantities are conserved within the control volume.

4.3.1 Control Volume Integral Means

First, the geometric domain (the flow field) under investigation is subdivided into control volumes Ω_i through an appropriate grid. When the cells are chosen as the control volumes, it is cell-centered, if the dual of a given grid is used, it is called as vertex-based, under which there is a volume corresponding to each vertex of the original grid.

Second, in order to approximate the integrals of Equation 4.1, the conservation variable

$\mathbf{U}$ is represented by cell-wise constant values $\mathbf{U}_i$.

$$\frac{\partial}{\partial t}\int_{\Omega_i}\mathbf{U}dV \approx |\Omega_i|\frac{\partial}{\partial t}\mathbf{U}_i \qquad 1 \le i \le N \tag{4.16}$$

Where $|\Omega_i|$ is the volume of Ω_i. It should also be noticed that $\mathbf{U}_i$ approximate the integral means of the true solution and are a conservative approximation. Thus Euler equations under the above discretization leads to a system of N ordinary differential equations in t.

$$\begin{aligned}\tfrac{\partial}{\partial t}\mathbf{U}_i = &\ -\tfrac{1}{|\Omega_i|}\textstyle\int_{\partial\Omega_i}\mathbf{F}\cdot d\mathbf{S} - \tfrac{1}{|\Omega_i|}\int_{\partial\Omega_i}\mathbf{G}\cdot d\mathbf{S} \\ = &\ -\tfrac{1}{|\Omega_i|}\textstyle\int_{\partial\Omega_i}\hat{\mathbf{F}}\cdot d\mathbf{S} \qquad 1 \le i \le N\end{aligned} \tag{4.17}$$

Here we define $\hat{\mathbf{F}} = \mathbf{F} + \mathbf{G}$ for notation simplicity.

4.3.2 Time Discretization

A simple time integration scheme can be obtained by replacing the time derivative $\frac{\partial}{\partial t}\mathbf{U}_i$ by a simple forward difference and evaluating the flux residual at the current level.

$$\frac{\partial}{\partial t}\mathbf{U}_i = \frac{\mathbf{U}_i^{n+1} - \mathbf{U}_i^n}{\Delta t} = -\frac{1}{|\Omega_i|}\int_{\partial\Omega_i}\hat{\mathbf{F}}\cdot d\mathbf{S} \qquad 1 \le i \le N \tag{4.18}$$

This corresponds to a single-stage explicit scheme, since updates are obtained from one evaluation of currently available quantities. Explicit Runge-Kutta schemes could also be used in order to achieve time accuracy, a fourth stage Runge-kutta scheme could be written as:

$$\begin{aligned}&\mathbf{W}_i^0 = \mathbf{U}_i^n \\ &\mathbf{W}_i^k = \mathbf{W}_i^0 + \alpha_k\Delta t\mathcal{F}(\mathbf{W}_i^{k-1}) \qquad \text{for} \quad k = 1\ldots 4 \\ &\mathbf{U}_i^{n+1} = \mathbf{W}_i^4\end{aligned} \tag{4.19}$$

Where $\mathcal{F}$ is defined as

$$\mathcal{F} = -\frac{1}{|\Omega_i|}\int_{\partial\Omega_i} \hat{\mathbf{F}} \cdot d\mathbf{S}$$

for notation simplicity. The α_k are chosen as the following:

$$\alpha_1 = 0.11, \alpha_2 = 0.2766, \alpha_3 = 0.5, \alpha_4 = 1.0$$

Δt is constrained by the *CFL condition*, which is that the domain of dependency of the numerical method includes the physical domain of dependency of the equation: Information in the numerical scheme must include information influencing the physical flow. this results in:

$$\Delta t \leq \Delta x/|\lambda_{max}| \tag{4.20}$$

where λ_{max} is the maximum wave speed,Δx is the control volume length, which will be addressed later.

4.4 First Order Upwind Scheme

As the approximate solutions are represented in a cell-wise constant manner, $\mathbf{U}_i$ over the control volume interfaces is still not well defined. If integral means are used for two neighboring control volumes i and $i+1$, $\mathbf{U}_i$ and $\mathbf{U}_{i+1}$ will be different on the interface.

There are several possibilities of dealing with this situation. One is to average the flow variables in the two control volumes on either side of the interface. Such a scheme corresponds to a central difference discretization on structured meshes and requires the addition of artificial diffusive terms to ensure stability. This approach has been used extensively to compute inviscid and viscous two- and three-dimensional flows. The discretization is simple to implement and relatively inexpensive to evaluate. However, the construction of the dissipative terms is nonoptimal in that it does not differentiate between the various wave components of the governing fluid dynamic equations [43].

Upwind schemes attempt to remedy this deficiency by applying the appropriate amount

of dissipation to each wave component. There are two major families of upwind methods, *flux vector splitting* and *flux difference splitting*. In *flux vector splitting*, the flux terms are split and discretized directionally in accordance with the sign of the associated propagation speeds (eigenvalues of the Jacobian matrix of the flux vectors). In *flux difference splitting*, the time evolution of the solution is determined by solving the Riemann problem at the interface boundaries of the computational cells.

4.4.1 Roe's Approximate Riemann Solver

In this research Roe's approximate Riemann Solver [49] was used. This approach belongs to the *flux difference splitting* category. Instead of solving the exact Riemann problem at the interface, a density-weighted averaging approach was used as a linear approximation, where the flow values are obtained via Roe's averaging

The approximate Riemann solver of Roe can then be written in the general form

$$\frac{\partial}{\partial t}U_i = -\frac{1}{2\Omega_i}\sum_{j=1}^{nsides}\Delta l_j[F_j + F_i - \mid \tilde{A} \mid (U_j - U_i)] \tag{4.21}$$

where Ω_i is the volume of the element, i and j now refer to the sides of the control volume element, and Δl_j denotes the unit normal vector to the current side of the control volume. For every edge that defines the control volume Ω_i, the subscript i refers to the left side of the edge and j to the right side, i may also be denoted by l and j as r. F is the Roe flux vector, $\mid \tilde{A} \mid (U_j - U_i)$ the dissipative term. $|\tilde{A}|$ is the positive definite Roe matrix formed from the Jacobian $\frac{\partial F}{\partial U}$, which can be decomposed as:

$$\tilde{A} = R\Lambda R^{-1} \tag{4.22}$$

Λ is the diagonal matrix containing the eigenvalues of the matrix $\tilde{A}$ and R is the characteristic vector. Derivation of Λ and R can be found in literature [59] and [56]

The Roe averaged flow values are defined as:

$$\xi = \sqrt{\frac{\rho_l}{\rho_r}} \tag{4.23}$$

$$\bar{\rho} = \xi\rho_l \tag{4.24}$$

$$\bar{u} = \frac{\xi u_l + u_r}{\xi + 1} \tag{4.25}$$

$$\bar{v} = \frac{\xi v_l + v_r}{\xi + 1} \tag{4.26}$$

$$\bar{h} = \frac{\xi h_l + h_r}{\xi + 1} \tag{4.27}$$

$$\bar{a}^2 = (\gamma - 1)[\bar{h} - \frac{1}{2}(\bar{u}^2 + \bar{v}^2)] \tag{4.28}$$

where subscripts l and r denotes the left or right face values at the control volume interface. Flow values u, v are the local projection of the flow values on the interface. So actually the Riemann solver is solved in the direction normal to the interface, it is not truly multi-dimensional, as waves are only allowed to propagate in the directions of the interfaces. This causes an inconsistency in the decomposition when the dominant characteristic in the flow field lies oblique to the grid. To improve the situation, a rotated Riemann solver [15] could be used. The fluxes are still obtained by solving the Riemann problems at the interfaces, but in directions determined by the physical nature of local flow.

4.4.2 Numerical Experiment

Numerical experiment was performed on the classical SOD's shock tube problem. Solution was obtained on a two dimension 50×3 coarse mesh and result was plotted against the exact Riemann solution in Figure 4-1. Results show that this method yields a satisfactory performance in resolving the shock wave discontinuity. However, as artificial viscosity is used in order to prevent oscillations near discontinuities, density discontinuities were not resolved on coarse mesh.

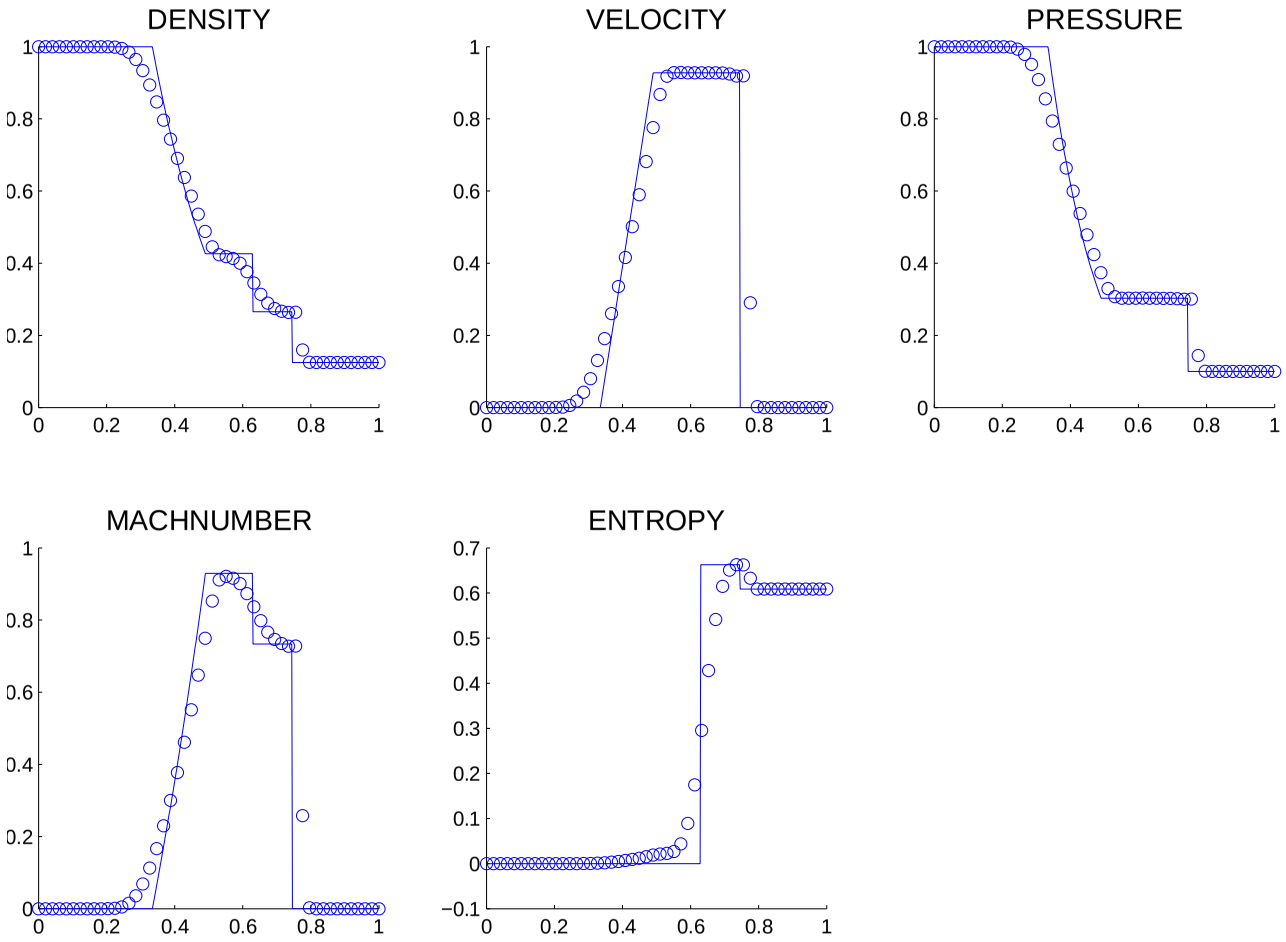

Figure 4-1: Sod's shock tube problem: exact (–) and numerical (o) solution with Roe's scheme.

4.5 High Resolution Schemes

While the upwind scheme is highly stable, it needs to be modified to high order if high resolution is desired. There are three major families of high resolution schemes, MUSCL [58], non-MUSCL TVD (e.g. MINIMOD [28]) ,ENO (essentially non-oscillatory) [29] and WENO (Weighted ENO) [36] schemes. Van Leer [58] introduced the idea of modifying the piecewise constant data in the first-order Godunov method to a achieve higher order of accuracy. This approach has become known as the MUSCL or Variable Extrapolation approach, while MUSCL stands for *Monotone Upstream-centered Scheme* for the Conservation Laws, where monotonicity in MUSCL is enforced through a limiter function applied to a piecewise polynomial flux reconstruction procedure. Harten [28] expressed monotonicity as a measure of discrete variation in the solution fields, which was named as total variational diminishing (TVD). In the non-MUSCL TVD schemes, the higher order extensions are carried out by embedding a flux limiter directly into the flux function. In ENO schemes, the accuracy is increased through the use of higher order interpolation functions and do not employ any type of limiter functions.

However, the application of higher order schemes to multi-dimensional unstructured mesh is not the direct extension of 1-D scheme due to the factor that most of the mathematical proofs in regards to these high resolution schemes have only been carried out for scalar $1D$ non-linear equations. It also has been proved that TVD schemes cannot be formally second order accurate in two or three dimensions. A number of TVD/MUSCL approaches for unstructured mesh have been implemented in the current research as illustrated and reviewed in [14] and [35]. Among them the implementation that follows the Barth and Jesperson scheme [7] [6] has been the most successful.

In the Barth and Jesperson scheme, the linear reconstruction of the control volume value Φ_p satisfies:

$$min(\Phi_N, \Phi_P) \leq R_P(\mathbf{r}_j) \leq max(\Phi_N, \Phi_P) \quad \forall N \in \texttt{Neighbors}(P) \tag{4.29}$$

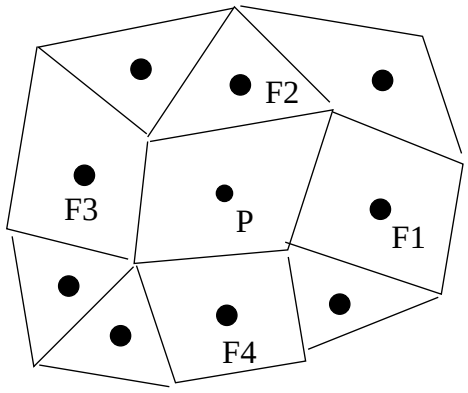

Figure 4-2: Illustration of control volume P and its neighbors, F_1, F_2, F_3, F_4.

Control volume P and its neighboring volumes are illustrated in Figure 4-2. j is some point within the control volume P, and R is the reconstruction operator given by:

$$R_P(\mathbf{r}_j) = \Phi_P + \Psi_J \nabla\Phi_P \cdot (\mathbf{r}_j - \mathbf{r}_P) \tag{4.30}$$

where Ψ is the flux limiter, and $\mathbf{r}$ is the position vector.

The idea of the reconstruction is to find the largest admissible Ψ while involving the monotonicity principle that values of the linearly reconstructed function must not exceed the maximum and minimum of neighboring centroid values. The computation of the flux limiter Ψ is performed in two steps as follows;

step 1 The reconstruction value is evaluated at each of the control volume's vertices in order to determine the flux limiter:

$$\Psi_j = \begin{cases} min(1, \frac{max(\Phi_N, \Phi_P) - \Phi_P}{\nabla\Phi_P \cdot (\mathbf{r}_j - \mathbf{r}_P)}), & \Phi_j > \Phi_P; \\ min(1, \frac{max(\Phi_P - \Phi_N, \Phi_P)}{\nabla\Phi_P \cdot (\mathbf{r}_j - \mathbf{r}_P)}), & \Phi_j < \Phi_P; \\ 1, & \Phi_j = \Phi_P. \end{cases} \tag{4.31}$$

step 2 The value of the limiter is computed as the minimal values of Ψ_j over all vertices, i. e.

$$\Psi_P = min(\Psi_j) \tag{4.32}$$

Such that during the linear reconstructions new extrema are not created and this scheme is equivalent to TVD-MUSCL scheme for a one dimensional discretization.

4.5.1 Numerical Experiment

The numerical experiment was performed on the classical SOD's shock tube problem. Solution was obtained on a two dimension 50×3 coarse mesh and the result was plotted against the exact Riemann solution in Figure 4-3. Second order linear reconstruction and second Runge-Kutta time integration was implemented in the scheme. Significant improvement on resolution was shown on the density discontinuity as compared with first order upwind scheme discussed in the previous section.

4.6 Numerical Implementation

4.6.1 Centroid of the Control Volume (Face)

In the control volume, the conservative and primitive variables are located at the *centroid* of the face (the polygon which forms the control volume). As a convex face can be divided into triangles, the location of the centroid $\mathbf{r}_G$ can be expressed in terms of the centroid of the triangles:

$$\mathbf{r}_G = \frac{\sum_{i=1}^{N} (\mathbf{r}_{Gi} * S_i)}{\sum_{i=1}^{N} S_i} \tag{4.33}$$

where

N is the total number of triangles that form the convex polygon.

r_{Gi} is the centroid of each individual triangle and can be expressed as the algebraic average of the locations of the three vertices that forms that triangle:

$$\mathbf{r}_{Gi} = \frac{1}{3}(\mathbf{r}_i + \mathbf{r}_{i+1} + \mathbf{r}_{i+2}) \tag{4.34}$$

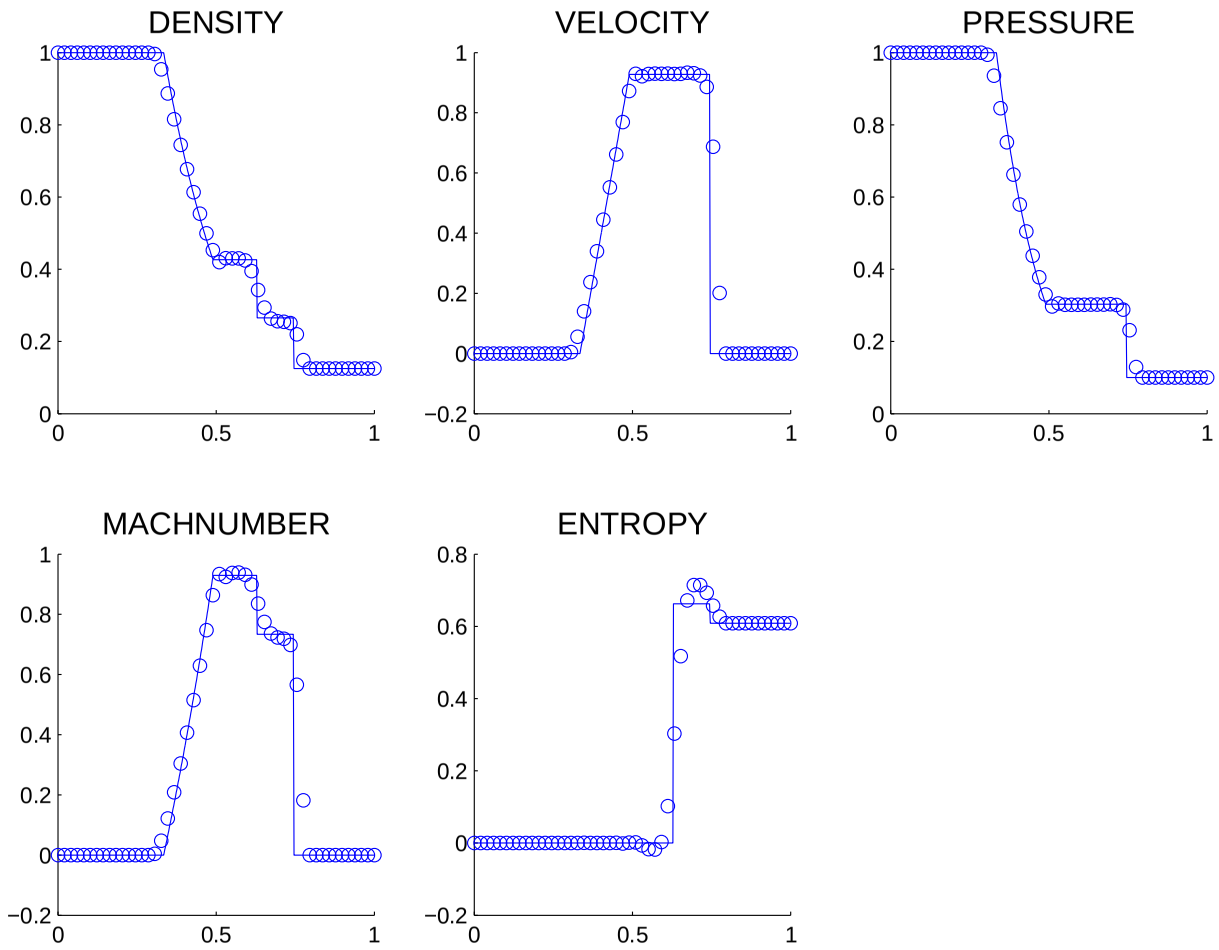

Figure 4-3: Sod's shock tube problem: exact (–) and numerical (o) solution with second order MUSCL projection and second order Runge-Kutta time stepping.

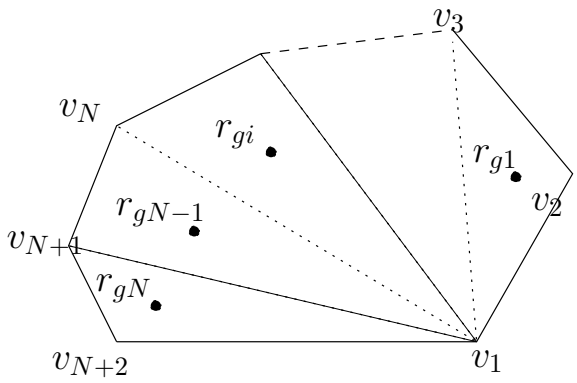

S_i is the area of the triangle, given by:

$$S_i = \frac{1}{2}|(\mathbf{r}_i - \mathbf{r}_{i+1}) \times (\mathbf{r}_i - \mathbf{r}_{i+2})| \tag{4.35}$$

4.6.2 Control Volume Lengths

When the algorithm is globally-explicit, the CFL condition must be met at all times and for all control volumes(faces) in the mesh(cell). Thus it becomes necessary to determine the lengths (or path) that the information must propagate to get through a specific volume. Previously, it was mentioned that all of the quantities were assumed to locate at the centroid of the face. Thus the distance travelled by any information must be measured from the centroid to the current edge of the face we are considering. This distance should be measured in such a way that the length vector is normal to the edge of the face. In the CFL condition

$$CFL = \frac{\Delta t|\lambda_{max}|}{\Delta x}, \tag{4.36}$$

this length vector can be referred to as Δx, or the spacing of the grid points where Δt and λ_{max} are respectively the time step and the maximum wave speed travelling through the face.

This length must be measured for all of the edges in the cell. Note that each edge has two related distances, corresponding to the two faces that share this particular edge and so $\Delta x = \Delta x^L + \Delta x^R$ where L and R refer to the corresponding lengths of the left and right

faces of a given edge.

4.6.3 Evaluation of Gradient

Face gradients are required to evaluate the viscous terms in the Navier-Stokes equations as well as to contract the high order upwind schemes.

One approach to get the gradients consists of first computing the gradients at the mesh vertices and then averaging these to the interfaces [23]. Such kind of discretization can also be derived by using a Galerkin finite-element procedure and assuming linear variation of the flow variables on the interfaces [42]. There are also schemes constructed by using Green-Gauss integration, and this method was later extended as the least-squares technique, which was shown to yield good approximations on distorted meshes [5].

Least square method is also referred to as the minimum energy reconstruction. It simply consists of fitting a linear function to the value of the neighboring nodes using the least-square technique. This is well documented in [52] by Sun Mingyu.

Suppose we are seeking the gradient $\nabla\xi = (\xi_x, \xi_y, \xi_z)$ of a scalar function ξ at node i. Values ξ_i and ξ_j at node i and its neighboring nodes j are known. The gradient is estimated by minimizing the distance between ξ_j and a piecewise approximation

$$\xi'_j = \xi_i + \nabla \cdot \Delta\mathbf{r}_{ji}, \tag{4.37}$$

where $\nabla\mathbf{r}_{ji} = (\Delta x_{ji}, \Delta y_{ji}, \Delta z_{ji}) = (x_j - x_i, y_j - y_i, z_j - z_i)$. The distance is expressed as

$$\sum_j (\xi_j - \xi'_j)^2 = \sum_j |\xi_j - (\xi_i + \nabla\xi \cdot \Delta\mathbf{r}_{ji})|^2 \tag{4.38}$$

where $\sum_j$ represents summing all neighboring nodes of node i. Minimizing the distance

leads to a linear system,

$$\begin{aligned}
(\textstyle\sum_j \Delta x_{ji}\Delta x_{ji})\xi_x + (\textstyle\sum_j \Delta x_{ji}\Delta y_{ji})\xi_y + (\textstyle\sum_j \Delta x_{ji}\Delta z_{ji})\xi_z &= \textstyle\sum_j \Delta x_{ji}\Delta\xi_{ji} \\
(\textstyle\sum_j \Delta y_{ji}\Delta x_{ji})\xi_x + (\textstyle\sum_j \Delta y_{ji}\Delta y_{ji})\xi_y + (\textstyle\sum_j \Delta y_{ji}\Delta z_{ji})\xi_z &= \textstyle\sum_j \Delta y_{ji}\Delta\xi_{ji} \\
(\textstyle\sum_j \Delta z_{ji}\Delta x_{ji})\xi_x + (\textstyle\sum_j \Delta z_{ji}\Delta y_{ji})\xi_y + (\textstyle\sum_j \Delta z_{ji}\Delta z_{ji})\xi_z &= \textstyle\sum_j \Delta z_{ji}\Delta\xi_{ji}
\end{aligned} \tag{4.39}$$

or, simply

$$\mathbf{Ax} = \mathbf{b} \tag{4.40}$$

where $\mathbf{A}$ is a matrix of the coefficients obtained from the left hand side of Equation 4.39, $\mathbf{b}$ represents the right hand side of the equation, and $\mathbf{x} = (\xi_x, \xi_y, \xi_z)^T$. Then we have

$$\mathbf{x} = \mathbf{A^{-1}b} \tag{4.41}$$

4.7 Data Structure

4.7.1 Data Structure for Numerical Simulation

Discretization techniques for partial differential equations come with a large varieties of different data-structures. Not only must we represent the conservation variables themselves for each control volume, but we must also represent the connectivity or topological relationships between the control volumes for the calculation of convective fluxes. Generally, data structures can be summarized into two categories, the *edge-based* and the *element-based* data structures.

Traditionally, finite-element methods (FEM) used in structural analysis have relied on element-based data structures, where for each element of the mesh a list of the forming vertex addresses is stored. Typically, cell types are restricted to one or a few fundamental convex polytopes, like triangles or quadrangles in 2D and tetrahedrons, prisms or cubes in 3-D.

However,unlike the FEM problem, Finite-Volume Methods (FVM) are less restrictive

on the type of cells so edge based data structure is necessary. A natural type of data structure is the structured mesh, i.e. array based data structure. Such array-based data structures store the subdivision connectivity of each control facet as a 2D array. Since the adjacency relations of the array are implicit they need not be maintained. While such kind of control volumes allow a straightforward and efficient implementation of computational algorithms for general problems, their application to complex geometries and adaptive mesh refinement requires a substantial amount of effort.

This limitation can be lifted by the implementation of an unstructured mesh. However, as there is no rigid connectivity rules at the vertices, no implicit array based data structure exists. Consequently , unstructured FVM are typically implemented using an edge-based data structure [43], either cell-centered or cell-vertex oriented. The cell-centered data structure consist of a list of cells, each with references to its vertices and cell-neighbors. The corresponding conservation variables are stored at the centroid of the cells. In the cell-vertex approach the grid is stored following grid nodes or vertices and the variables are stored at the vertices. Although no conservative variables are stored on the edge, the change of the conservative values in a cell is equal to the sum of fluxes through its interfaces, i.e. the dual edges that join two neighboring cell centroids and pierces the face common to these two cells in the vertex-based scheme or the edges which connect two adjacent vertices in that cell for the cell-centered scheme.

While an edge-based data structure is a necessity for the maintaining of the connectivity or topological relationships between the control volumes, it also has its disadvantages. It requires a preprocessing operation to extract a unique list of edges from the list of mesh elements and to compute the associated edge coefficients [43]. For unsteady flows with dynamic meshes, this preprocessing must be performed every time the mesh is altered, although this may be done locally. Additionally, for dynamic grid cases, element based data structures are generally required for performing mesh motion or adaptation, since edge lists represent a lower-level description of the mesh.

This shortcoming was over came by Sun Mingyu [52], who proposed an essentially

vectorizable cell-face data structure for any unstructured quadrilateral and hexahedral grids. The data structure is a bi-directional reference between cell and face with a strict ordering method, which is based on the *Königsberg bridge* problem. However, the dynamic grid refinement is confined to simple topological changes in this method.

In the case of viscous flow on nonsimplicial meshes, the resulting stencils involve vertices that are not connected to the center vertex by a mesh edge. In these situations, the element-based data structure must also be retained [11].

4.7.2 Quad-Edge Data Structure

The aforementioned restrictions can be eliminated by the implementation of the *quad-edge* data structure[25]. Other commonly used data structures used in computational geometry are: *winged-edge* of Baumgart [8],*split-edge* [18] and the *lath-based* [39] data structure. The incidence queries offered by these implementations rely on the ordering of edges around faces and vertices, and access to the next and previous edges at both vertices are explicitly given. All these data structures also support modifying operations. They offer some variants of Euler operators, such as attaching, splitting and deleting cells, while generally the data structure used in numerical simulation only allow refinement and derefinement operations [9].The uniqueness of the *quad-edge* data structure is its duality, with which vertices and faces are treated similarly. It is not only useful in the sense of Voronoi diagrams and Delaunay triangulation, but it also facilitates the search of vertices/edges/faces immediately adjacent to a given vertex/edge/face in constant time. With such duality, element-based data structures are no longer needed for nonsimplicial computation stencils.

The quad-edge data structure implementation was adapted from Paul Heckbert at CMU [30]. This data structure is originally written for describing the topology and geometry of polyhedra in computational geometries. It offers excellent adjacency queries efficiency and elegant Euler operation over the mesh, which make it very promising in the numerical simulation area, where the finite volume method requires effective methods in neighbor querying and mesh adaption. It can also deal with arbitrary polygonal unstructured control

volumes. Number of sides per control volume severely interferes with the mesh regeneration process due to mesh moving and local refinements are no longer restricted.

In the *quad-edge* data structure, there are classes for vertices, edges, and faces, but edges play the leading role. The edges store complete topological information; all of the topological information stored by the faces and vertices is redundant with information in the edges. Figuratively speaking, the edges form the skeleton, and the vertices and faces are optional decorations, hanging off of the edges. Vertices hold most of the geometric (shape) information.

Edge Class

The class `Edge` represents a directed edge. Given `Edge *e`, we can find the immediately adjacent vertices, faces, and edges, and the "symmetric" edge that points in the opposite direction. These operators are all fast (just a few memory references). Because edges are directed and we always imagine ourselves viewing the object from the outside, we can speak of the origin and destination vertices and left and right faces of an edge. We summarize the interface as shown in Figure 4-4.

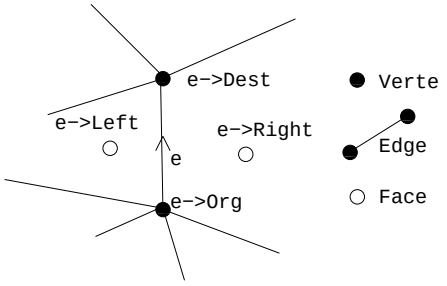

`Edge *e`	directed edge
`Vertex *e->Org()`	vertex at the origin of e
`Vertex *e->Dest()`	vertex at the destination of e
`Face *e->Left()`	face on the left of e
`Face *e->Right()`	face on the right of e

Figure 4-4: Key members of the quad-edge class.

For those functions in Figure 4-5, "next" means next in a counterclockwise (ccw) sense around a neighboring face or vertex.

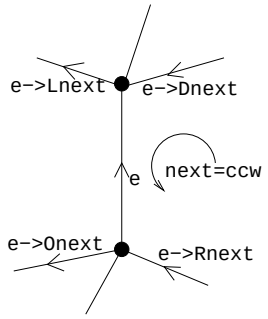

`Edge *e->Rnext()`	next edge around right face, with same right face
`Edge *e->Lnext()`	next edge around left face, with same left face
`Edge *e->Onext()`	next edge around origin, with same origin
`Edge *e->Dnext()`	next edge around dest, with same dest

Figure 4-5: CCW edges on a edge's neighboring face.

For those functions in Figure 4-6, "prev" means next in a clockwise (cw) sense around a neighboring face or vertex.

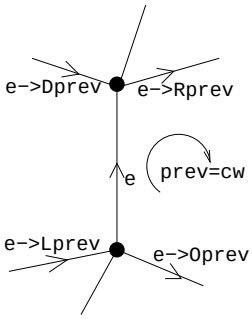

`Edge *e->Rprev()`	prev edge around right face, with same right face
`Edge *e->Lprev()`	prev edge around left face, with same left face
`Edge *e->Oprev()`	prev edge around origin, with same origin
`Edge *e->Dprev()`	prev edge around dest, with same dest

Figure 4-6: CW edges on a edge's neighboring face.

The member function `unsigned int {e->getID()` returns a unique interger ID for each edge, which is useful for numbering the edges.

We can loop around the edges of the face on the left of edge `estart` in ccw order:

```
void leftFromEdge(Edge *estart) {
    Edge *e = estart;
```

```
    do {
    <do something with edge e>
    e = e->Lnext();
    } while (e!=estart);
}
```

Similarly, the edges around the origin vertex of edge `estart` can be visited in ccw order like so:

```
void orgFromEdge(Edge *estart) {
    Edge *e = estart;
    do {
    <do something with edge e>
    e = e->Onext();
    } while (e!=estart);
}
```

Since visiting the edges around a face (or edges around a vertex) is quite common, iterator classes were set up to simplify the code. Using the iterator, an alternative to `leftFromEdge` is:

```
void edgesOfFace(Face *face) {
    // visit edges of face in ccw order;
    // edges have face on the left
    FaceEdgeIterator faceEdges(face);
    Edge *edge;
    while ((edge = faceEdges.next()) != 0)
    <do something with edge e>
}
```

Using an iterator, the alternative to `orgFromEdge` is:

```
void edgesOfVertex(Vertex *vert) {
    // visit edges of vertex in ccw order;
    // edges have vert as origin
    VertexEdgeIterator vertEdges(vert);
    Edge *edge;
    while ((edge = vertEdges.next()) != 0)
    <do something with edge e>
}
```

Duality

The quad-edge data structure gets its name because the duality is built in at a low level by storing quadruples of directed edges together:

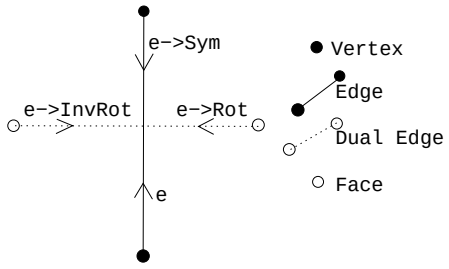

`Edge *e`	directed edge
`Edge *e->Sym()`	edge pointing opposite to e
`Edge *e->Rot()`	dual edge pointing to the left of e
`Edge *e->InvRot()`	dual edge pointing to the right of e

Figure 4-7: Duality of a quad-edge class.

Vertex Class

The information stored at a vertex consists of one piece of topological information (a pointer to one of the outgoing edges of the vertex) and the geometric information (the (x,y,z) position).

```
class Vertex {
```

```
    Vec3 pos;           // (x,y,z) position of this vertex
    const void *data;    // data pointer for this vertex
    Edge *getEdge();     // an outgoing edge of this vertex
    unsigned int getID();
    // id# of this vertex (unique for this Cell)
};
```

Here, Vec3 is essentially an array of three doubles. The Vec3 class belongs to the Simple Vector Library (SVL) of Andrew Willmott from CMU.

Face class

Each face stores one piece of topological information, a pointer to one of the ccw-oriented edges of the face, plus optional attribute information.

```
class Face {
    Edge *getEdge();     // a ccw-oriented edge of this face
    const void *data;    // data pointer for this vertex
    unsigned int getID();
     // id# of this face (unique for this Cell)
};
```

Cell, and Euler Operators

A Cell is a whole computational domain, which includes sets of vertices, edges, and faces. The routines we need most are the following four:

```
class Cell {
    Edge *makeVertexEdge(Vertex *v, Face *left, Face *right);
    Edge *makeFaceEdge(Face *f, Vertex *org, Vertex *dest);
    void killVertexEdge(Edge *e);
    void killFaceEdge(Edge *e);
```

```
};
```

which are called Euler operators, since they maintain Euler's formula $V - E + F = 2$ interrelating the number of vertices, edges, and faces of a polyhedron of genus 0 (topologically equivalent to a sphere). If the topology is a valid polyhedron before the call, it will be valid after the call, as well. Note that these routines update the topology, but they use the default constructors for Vertex and Face, so the positions of new vertices are (0,0,0) .

Given Cell *c, the calls do the following as shown in Figure 4-8:

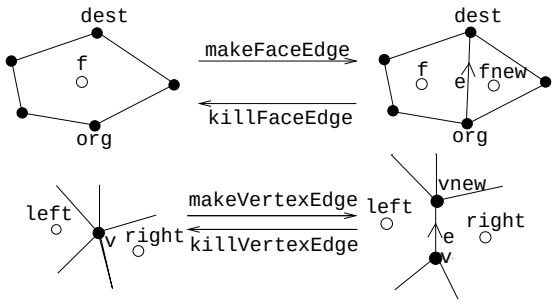

Figure 4-8: Euler operators

`c->makeVertexEdge(v, left, right)` splits vertex v, creating a new edge and vertex that both lie between faces left and right. The new edge has left on its left and right on its right, v at its origin and the new vertex at its destination. The new edge is returned; the new vertex is easily found by taking Dest() of the return value. The new vertex and edge are stored in the sets associated with cell c. If left and right are not adjacent to v then an error message will be printed and core dumped.

`c->makeFaceEdge(f, org, dest)` is the dual of makeVertexEdge. It splits face f, creating a new edge and face that both lie between vertices org and dest. The new edge has org as its origin and dest as its destination, f as its left face and the new face as its right face. The new edge is returned; the new face is easily found by taking Right() of the return value. The new face and edge are stored in the sets associated with cell c. If org and dest are not adjacent to f then an error message will be printed and core dumped.

`c->killVertexEdge(e)` is the inverse of makeVertexEdge. It removes edge `e` and vertex `e->Dest()`. Thus,
`c->killVertexEdge(c->makeVertexEdge(v, left, right))` is a no-op.

`c->killFaceEdge(e)` is the inverse of makeFaceEdge. It removes edge `e` and face `e->Right()`. Thus,
`c->killFaceEdge(c->makeFaceEdge(f, org, dest))` is a no-op.

The data structure also has routines to loop over all the vertices, edges, or faces of a cell. To loop over the vertices of Cell *c:

```
CellVertexIterator cellVerts(c);
Vertex *v;
while ((v = cellVerts.next()) != 0)
    <do something with vertex v>
```

To loop over the faces of Cell *c:

```
CellFaceIterator cellFaces(c);
Face *f;
while ((f = cellFaces.next()) != 0)
    <do something with face f>
```

4.8 Adaptive Mesh Refinement

Adaptive mesh refinement techniques which automatically adapt the computational grid to the solution of the governing partial differential equations can be very effective in improving solution accuracy or treating problems with disparate length scales. It has progressed

rapidly over the last decade and the main types of optimal mesh criteria, error indicators/estimators and refinement strategies was reviewed and compared by R. Lohner [41]. There are two motivations for using adaptive mesh refinement.

- With mesh adaption, the numerical solution to a specific problem can be achieved with the least number of degree of freedom which yields less amount of work for a given accuracy.

- Physical phenomena have disparate length scales and thus if the grid is allowed to adapt to the solution, users no longer waste time choosing a grid that is suitable for the problem at hand. It is of more importance for transient problems with travelling discontinuities such as shocks and contract surfaces. In this way, such regions of our interest will be studied with high resolution.

4.8.1 Mesh Refinement Indicator

To design an adaptive mesh procedure, a quantitative assessment of the optimality of the adaptive mesh procedure is required. Such criterion can be based on the geometry of the simulation domain or the physical phenomena. A criterion adopted in the current study is to refine the mesh such that numerical error is distributed equally in the computational domain, where mesh refinement will be applied to those cells in which error is large. Two different error indicators are tried in the current numerical experiments.

One error indicator is based on the jumps of indicator variables.This error indicator implicitly assume first order accuracy for the underlying scheme so preliminary numerical result in current numerical application is not optimal as second order numerical scheme was used in the current research.

The second error indicator is to compare different orders of derivatives. The underlying assumption is that the solution should be smooth at the order of desired numerical accuracy, i.e. the difference between Taylor series expansion on flow variables of higher order and that of desired order should be minimized with localized mesh refinement.

Mesh refinement indicator also has to be non-dimensionalized such that it will be able to indicate strong flow features (e.g. strong shocks) and weak features (secondary shocks, contact discontinuities) as well. Such indicator was proposed in [40]. In general terms, it is of the form

$$error = \frac{h^2|seconddderivatives|}{h|firstderivatives| + \alpha_f|meanvalue|} \tag{4.42}$$

By dividing the second derivatives by the absolute value of the first derivatives, the error indicator becomes bounded, dimensionless and the "eating up" effect of strong features is avoided. The terms following α_f are added as a noise filter in order not to refine wiggles or ripples which may appear due to loss of monotonicity.

The current criterion for adaption is:

$$\epsilon_T = Max(\frac{|(\nabla_{l\rho})_C - (\nabla_{l\rho})_i|}{\alpha_f\rho_c/dl + |(\nabla_{l\rho})_i|}, \frac{|(\nabla_{l\rho})_C - (\nabla_{l\rho})_j|}{\alpha_f\rho_c/dl + |(\nabla_{l\rho})_j|}) \tag{4.43}$$

where ϵ_T is the truncation error indicator, as shown in figure 4-9, i, j are indices of two neighboring cells, ∇_l is the gradient along the lines connecting two neighboring cells, index C denote the center of the edge that cell i and j share. α_f is the noise filter, typical value is 0.03. dl is the distance between two neighboring cells' centroid. For each cell, ϵ_T

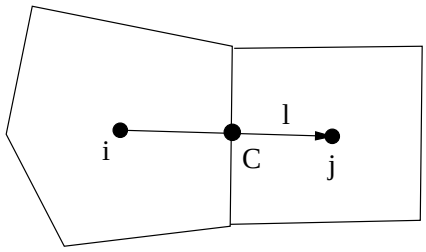

Figure 4-9: Sketch of the cell interface between two neighboring cells i and j

was evaluated at all of its interfaces and the cell will be:

- refined if maximum of ϵ_T of all neighboring edges $> \epsilon_r$;
- coarsen if maximum of ϵ_T of all neighboring edges $< \epsilon_c$

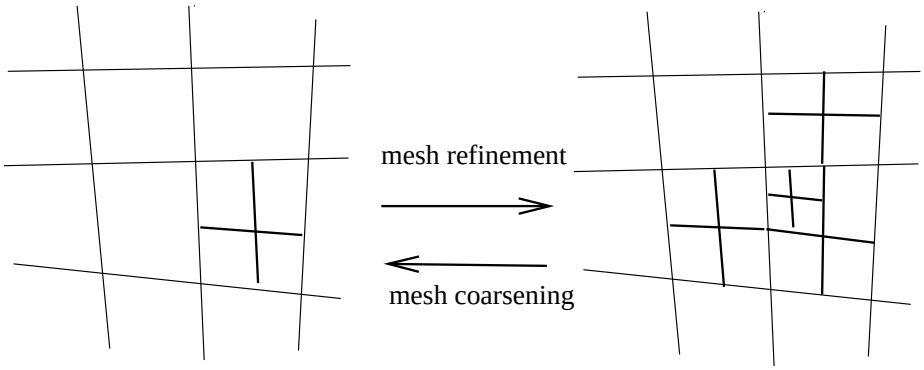

Figure 4-10: Illustration of adaptive mesh refinement strategy

ϵ_r and ϵ_c are two threshold values for refinement and coarsening with typical values: $\epsilon_c = 0.05$ and $\epsilon_r = 0.08$.

4.8.2 Mesh Refinement Strategies

Mesh refinement strategies are refereing to how the mesh is divided or merged and geometrical topology information is updated during the adaption process. A classical *h-refinement* method was chosen such that cells are subdivided by four where higher mesh densities were needed. The process of refinement and coarsening was illustrated in figure 4-10 accomplished with basic Euler operation facilitated by the *Quad-edge* mesh data structure such that geometrical topology information of each cell and corresponding vertices, edges was updated within the Quad-edge class. Recursive subdivision and agglomeration are achieved through two refinement level indicators: cell adaption level and vertices adaption level. As geometrical topology information is updated locally, such implementation is highly efficient and coding can be unified for cell flux evaluation, refined cells were treated the same way as coarsen cells.

4.8.3 Numerical Experiment

A test case was carried out to evaluate the effectiveness of the current adaptive mesh refinement procedure. The initial coarse mesh used for the calculation was shown in figure 4-11,

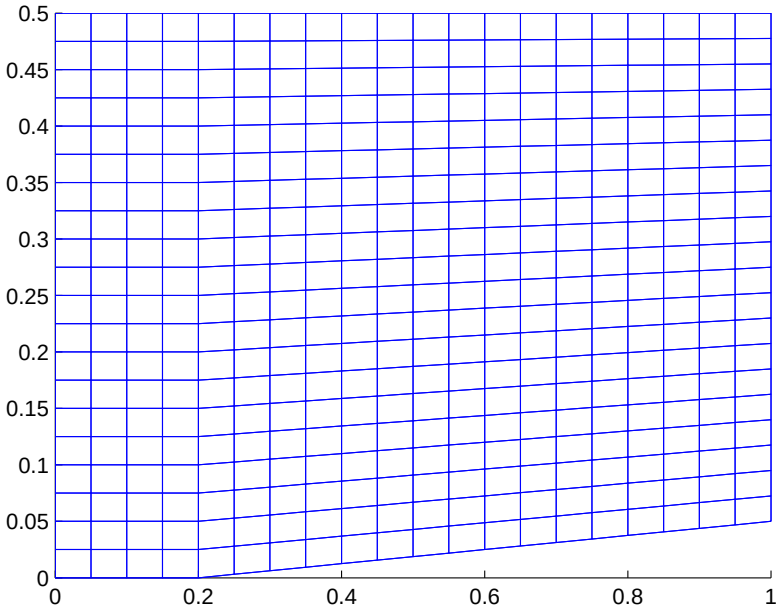

Figure 4-11: Initial coarse mesh used for supersonic flow passing a ramp.

the inlet boundary at left is set as $M = 1.5, P = 1$. Computation was performed with two levels of adaptive mesh refinement and ended at time $t = 2.0$. Figure 4-12 shows the final refined mesh. Figure 4-13 shows the pressure contour plotted on the refined mesh. Figure 4-14 shows the pressure contour. Mesh was effectively refined at the flow discontinuity and a significant improvement on the resolution of the shock wave was observed.

4.9 Treatment of Moving Boundary

4.9.1 Closely Coupled Model of Fluid Structure Interaction

The prediction of fluid and structure interaction phenomena requires solving simultaneously the coupled fluid and structural equations of equilibrium. In this process, a closely coupled model is one of the most widely used methods in the field of Computational Aero-Elastic (CAE) as it not only paves way for the use of different solvers for fluid and structure

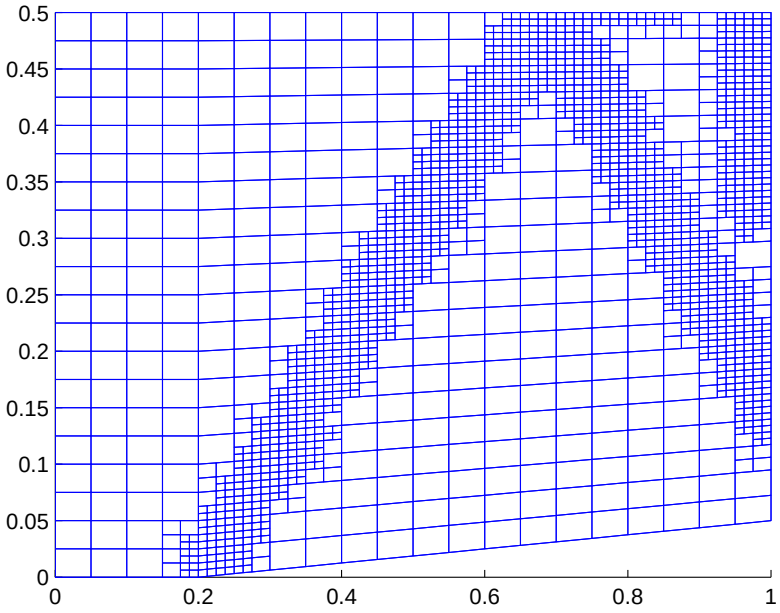

Figure 4-12: Refined mesh for supersonic flow passing a ramp, at $t = 2$.

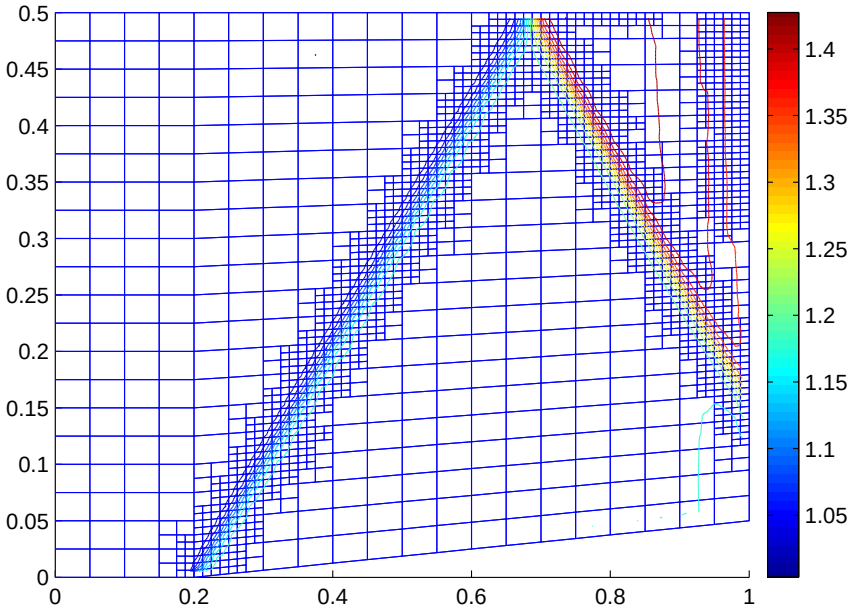

Figure 4-13: Pressure contour on refined mesh for supersonic flow passing a ramp, at $t = 2$

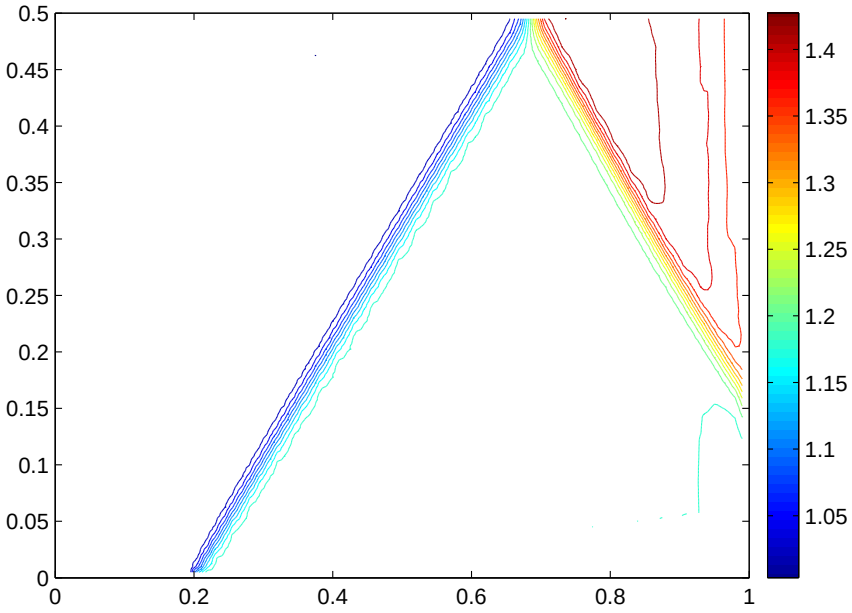

Figure 4-14: Pressure contour for supersonic flow passing a ramp, at $t = 2$

models, but also couples the solvers in a tight fashion thereby making it an efficient method for complex nonlinear problems [38]. In this approach, the fluid and structure equations are solved separately using different solvers but are coupled into one single module with exchange of information taking place at the interface or the boundary via an interface module thereby making the entire CAE model tightly coupled. The information exchanged here are the surface loads, which are mapped from CFD surface grid onto the structure dynamics grid; and the displacement field, which are mapped from structure dynamics grid onto CFD surface grid. The transfer of surface displacement back to the CFD module implies deformation of the CFD surface mesh and this calls for a moving boundary technique to enable re-meshing the entire CFD domain as we march in time.

Current implementation is that on the interface boundary, load was transferred to the structure from fluid as a pressure loading on the structural element and motion of the structure was transferred to the fluid domain by dynamically updating the computational mesh.

4.9.2 Mesh Adjustment on Moving Boundary

To transfer the structural motion back to the fluid domain during the numerical simulation of coupled fluid and structure interaction, various methods are developed in the past, including the cartesian cut-cell methods developed by De Zeeuw and Powell [16], overset mesh [31], arbitrary Lagrangian-Eulerian (ALE) methods, [32], the interface tracking methods of Glimm [24], immersed boundary methods [46] and recently the external force method [4].

Some methods require a mesh topology change during the treatment of moving boundaries. Two popular approaches are, mesh regeneration at the moving boundary or deformation of the computational mesh to accommodate the interface motion.

Popular ALE methods involve deforming mesh which may result in poor mesh quality and generally it requires the interpolation of flow variables, while such interpolation processes are not conservative, though they can be accurate and reliable in some cases [19]. However, the advancing front approach addresses the moving grid problem in a way that the interpolation process is circumvented. Mesh was locally regenerated on the moving boundary at each computation step and internal mesh interfaces were not changed, such that no interpolation of velocity is involved in the flux calculation. Such schemes maintain a conservation on all conservative flow variables and optimal mesh quality is maintained.

This advancing front method must be carefully implemented to avoid high aspect-ratio or highly skewed cells. To avoid cutting cells that are a small fraction of the size of uncut cells, it was merged with neighboring uncut cells if necessary. Such implementations result in smooth high quality mesh in most regions of the flow-field.

Again the process of advancing front mesh regeneration was greatly benefited by the implementation of *Quad-edge* data structure. Efficient algorithms were made possible for the mesh splitting and agglomerating. When an individual element was added to the boundary one at a time at an existing front, mesh topology was updated inherently during the basic mesh Euler operation such that time consuming global iteration was not needed.

When new mesh is generated by the subdivision algorithm, additional vertices are in-

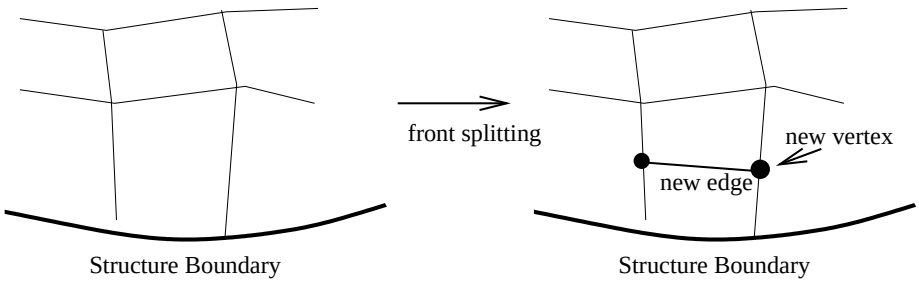

Figure 4-15: Illustration of control volume splitting during the advancing front mesh adjustment.

serted into the mesh. During the mesh simplification process, some vertices may be deleted. Such newly generated or deleted vertices generally result in faces with an arbitrary number of edges. The current numerical code was implemented in a way such that faces with an arbitrary number of edges were treated normally in computation.

The control volume splitting and merging process is illustrated in Figure 4-15 and 4-16 respectively. As a result of the structure boundary moving towards the flow region, edges of the corresponding boundary control volume may fall short of the predefined critical length, such boundary control volumes will be merged with its immediate inner control volume. However, such inner control volume may have been refined during the adaptive mesh refinement process so it will be coarsen first. A recursive algorithm is implemented such that the level of refinement would return to its original status of one. After the coarsening process, the edge shared by these two control volumes will be deleted and corresponding vertices may also be deleted if the neighboring control volume has also been merged. Corresponding conservative variables will be summed up for those merging control volumes and new primitive values will be updated as well as the corresponding geometry variables such as the edge length, control volume centroid and area. The splitting of a control volume was relatively more straightforward. New vertices were inserted in the middle of the corresponding edge if necessary and a new edge would be created linking these vertices, which would split the control volume in half. The newly created control volume will have its conservative variables interpolated and subtracted from the original control volume. Geometry variables were updated as well correspondingly. As there are no intergradation of primitive

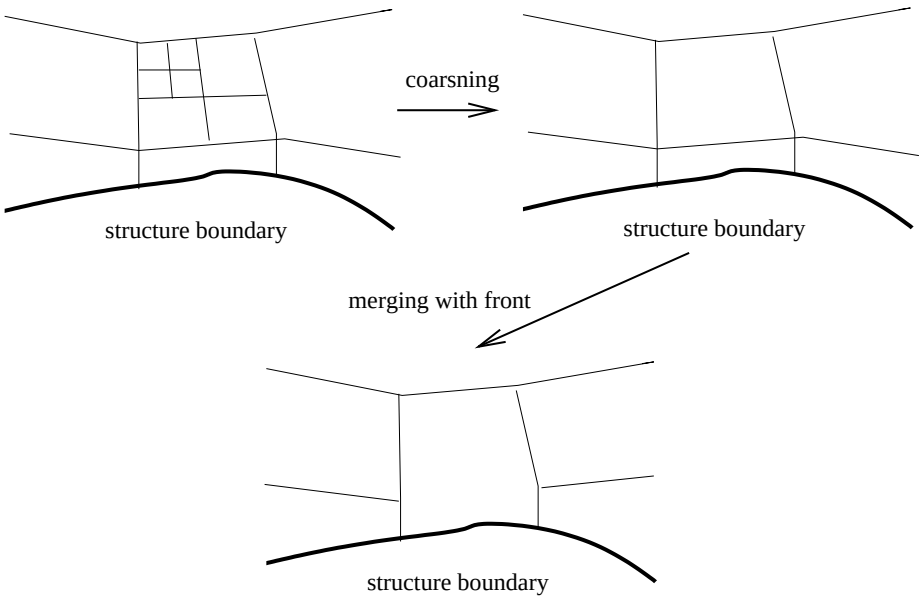

Figure 4-16: Illustration of control volume merging during the advancing front mesh adjustment.

variables and no inner edge movement involved in such implementation, this method is fully conservative.

4.9.3 Numerical Flux Evaluation on Adjusted Mesh

Traditional ALE methods were implemented as [32]:

$$\frac{d}{dt}\int_V \rho dV - \int_S \rho(\mathbf{U}-\mathbf{u})\cdot\mathbf{n}dS = 0 \qquad (4.44)$$

$$\frac{d}{dt}\int_V \rho\mathbf{u}dV - \int_S \rho\mathbf{u}(\mathbf{U}-\mathbf{u})\cdot\mathbf{n}dS + \int_V \nabla p dV - \int_V \rho g dV = 0 \qquad (4.45)$$

$$\frac{d}{dt}\int_V \rho E dV - \int_S \rho E(\mathbf{U}-\mathbf{u})\cdot\mathbf{n}dS + \int_S \nabla p\mathbf{u}\cdot\mathbf{n}dS - \int_V \rho g\cdot\mathbf{u}dV = 0 \qquad (4.46)$$

In these expressions $\mathbf{U}$ is the velocity of the surface S. When $\mathbf{U} = 0$ the equations are Eulerian, and when $\mathbf{U} = \mathbf{u}$ the equations are Lagrangian. If the control volume is under displacement and expansion/deformation at the same time, the velocity on the surface of the control volume will be a combination of the control volume centroid velocity and a

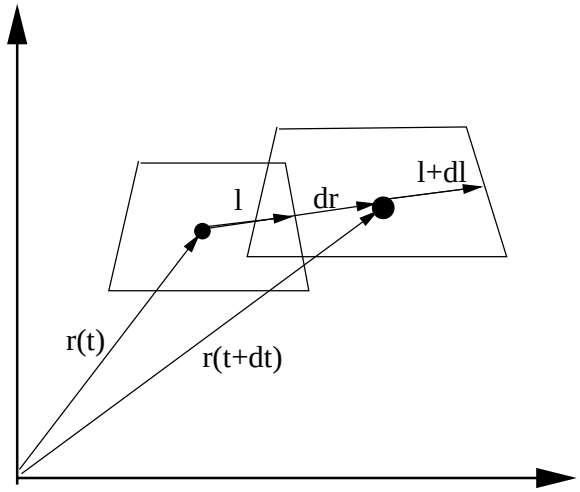

Figure 4-17: Illustration of ALE control volume.

term related to its expansion/deformation rate, $\mathbf{U} = dr/dt + d\mathbf{u}/dr \cdot dl$ as shown in Figure 4-17. If the mesh is under global movement, $\mathbf{U}$ is not zero everywhere such that it has to be accounted for on each control volume surface, and further more, $\mathbf{u}$ will have to be interpolated under a new mesh topology and it may affect the flow solver's accuracy and stability. Under the proposed advancing front method as illustrated in Figure 4-18, we have $\mathbf{U} = 0$ on all internal control volume surfaces and $\mathbf{U} = \mathbf{u}$ on structure boundary. Consequently in equation 4.44, surface integral on conservative variable $\mathbf{w}$, $\int_S \mathbf{w}(\mathbf{U} - \mathbf{u}) \cdot \mathbf{n} dS$ is 0 and no interpolation velocity will be directly involved in the flux calculation. Under a second order MUSCL scheme, primitive variables maybe needed for the Riemann solver and the velocity on the boundary control volume centroid can be calculated directly from updated conservative variables as well as the new geometrical variables including new centroid position and control volume area.

4.9.4 Numerical Experiment

Numerical experiments were carried out to confirm the effectiveness of the current advancing mesh approach. Figure 4-19 is the mesh with initial adapt mesh refinement used for numerical simulation. The lower boundary is the structure boundary so during the simula-

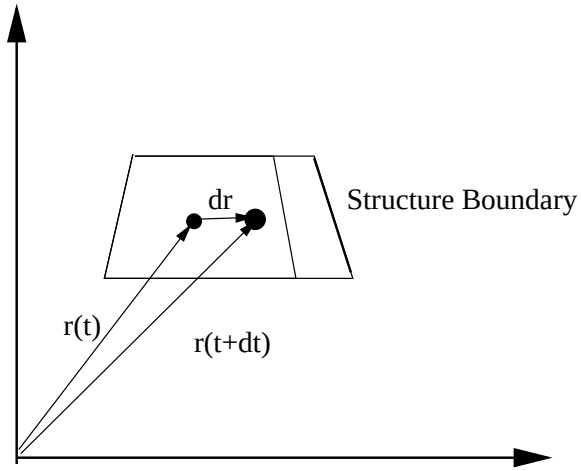

Figure 4-18: Illustration of advancing front control volume

tion, it will deform when aerodynamic loading is applied, as a result, new mesh is generated next to the structure boundary as illustrated in Figure 4-20. As the structure boundary started moving towards the inner flow region, the inner mesh is automatically removed as shown in Figure 4-21. Such mesh regeneration process is performed at each simulation time step and all boundary control volumes are automatically adjusted according to their corresponding boundary position. One level of adaptive mesh refinement is also performed within each time step so density discontinuities such as contact surface can be resolved with high resolution.

4.10 Finite Element Solver

4.10.1 Axisymmetric Shell FEM Model

The problem of a circular plate under blast loading can be modelled with a finite element axisymmetric shell model as in [45]. Using the Kirchhoff-Love assumption, the problem is greatly simplified and the element is essentially 'one-dimensional'.

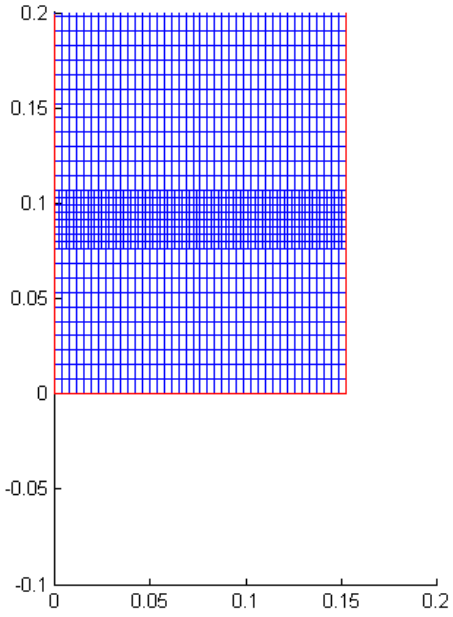

Figure 4-19: Initial mesh after first step of adapt mesh refinement.

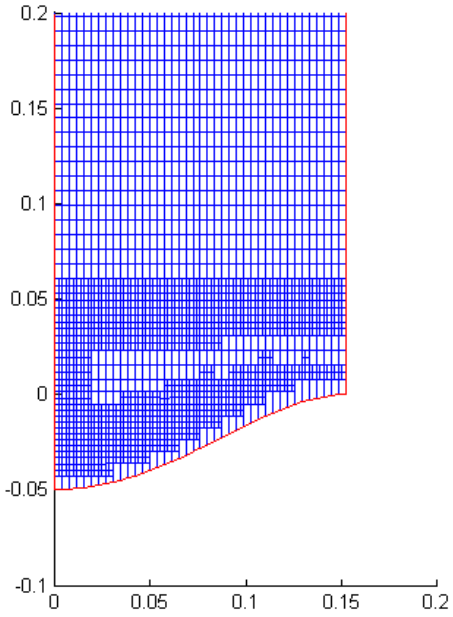

Figure 4-20: Mesh at t=0.00383 with advancing front on structure boundary.

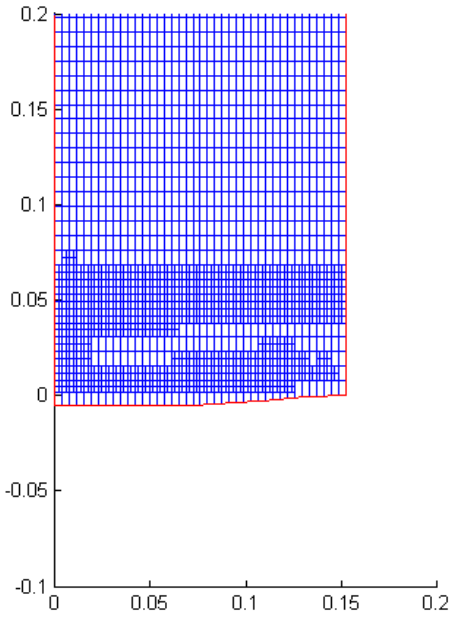

Figure 4-21: Mesh at t=0.00555 with advancing front on structure boundary.

The four strain components are given by:

$$\epsilon = \left\{ \begin{array}{c} \epsilon_s \\ \epsilon_\theta \\ \chi_s \\ \chi_\theta \end{array} \right\} = \left\{ \begin{array}{c} d\bar{u}/ds \\ (\bar{u}cos\phi - \bar{w}sin\phi)/r \\ -d^2\bar{w}/ds^2 \\ -(d\bar{w}/ds)cos\phi/r \end{array} \right\} \tag{4.47}$$

The four internal stress are related to the strains by an elasticity matrix $\mathbf{D}$:

$$\sigma = \left\{ \begin{array}{c} N_s \\ N_\theta \\ M_s \\ M_\theta \end{array} \right\} = \mathbf{D}\epsilon \tag{4.48}$$

for an isotropic shell the elasticity matrix becomes:

$$\mathbf{D} = \frac{Et}{1-\nu^2}\begin{bmatrix} 1 & \nu & 0 & 0 \\ \nu & 1 & 0 & 0 \\ 0 & 0 & t^2/12 & \nu t^2/12 \\ 0 & 0 & \nu t^2/12 & t^2/12 \end{bmatrix} \tag{4.49}$$

where E and ν are the Young's modulus and Poisson's ratio, t is the thickness of the shell. Let the shell be divided by nodal circles into a series of conical ring element, as shown in Figure 4-22 The displacement of a node i can be defined by three components, the first two being in global directions r and z,

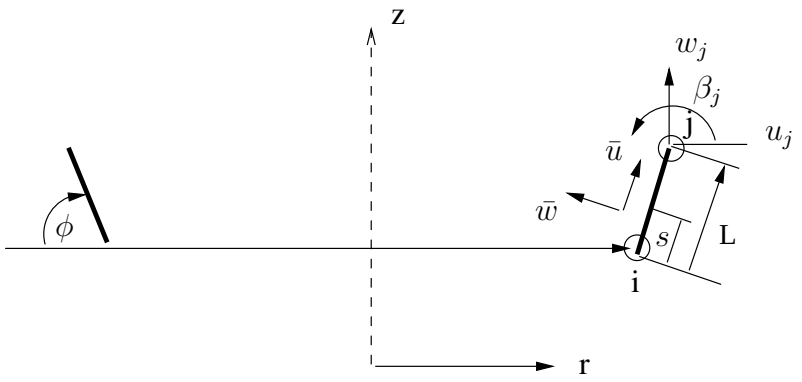

Figure 4-22: An element of an axisymmetric shell

$$\mathbf{a_i} = \begin{Bmatrix} u_i \\ w_i \\ \beta_i \end{Bmatrix} \tag{4.50}$$

and for an element with two nodes, i and j, there will be 6 degrees of freedom, determined by the element displacements

$$\mathbf{a^e} = \begin{Bmatrix} \mathbf{a}_1 \\ \mathbf{a}_2 \end{Bmatrix} \tag{4.51}$$

The displacements of a point on the middle surface of the element, $\bar{u}$ and $\bar{w}$ in the local

coordinate, can be expressed by its position within the element, s

$$\bar{u} = a_1 + a_2 s \tag{4.52}$$

$$\bar{w} = a_3 + a_4 s + a_5 s^2 + a_6 s^3 \tag{4.53}$$

$a_1, a_2, ..., a_6$ are coefficients to be determined and they should satisfy the following in order to maintain slope and displacement continuity:

$$a_1 = \bar{u}_i \tag{4.54}$$

$$a_3 = \bar{w}_i \tag{4.55}$$

$$a_4 = \left(\frac{d\bar{w}}{ds}\right)_i \tag{4.56}$$

$$a_1 + a_2 L = \bar{u}_j \tag{4.57}$$

$$a_3 + a_4 L + a_5 L^2 + a_6 L^3 = \bar{w}_j \tag{4.58}$$

$$a_4 + 2a_5 L + 3a_5 L^2 = \left(\frac{d\bar{w}}{ds}\right)_j \tag{4.59}$$

here L is the length of shell element as illustrated in Figure 4-22. Solving the above equations for $a_1, a_2, ..., a_6$ and equation 4.52 became:

$$\bar{\mathbf{u}} = \left\{ \begin{array}{c} \bar{u} \\ \bar{w} \end{array} \right\} = \bar{N}\mathbf{a^e} \tag{4.60}$$

where:

$$\bar{N} = [\bar{N}_1, \bar{N}_2] \tag{4.61}$$

$$\bar{N}_1 = \left[\begin{array}{ccc} \frac{1}{2} - \frac{1}{2}\xi & 0 & 0 \\ 0 & \frac{1}{2} - \frac{3}{4}\xi + \frac{1}{4}\xi^3 & \frac{1}{8}L\left(1 - \xi - \xi^2 + \xi^3\right) \end{array} \right] \tag{4.62}$$

$$\bar{N}_2 = \left[\begin{array}{ccc} \frac{1}{2} + \frac{1}{2}\xi & 0 & 0 \\ 0 & \frac{1}{2} + \frac{3}{4}\xi - \frac{1}{4}\xi^3 & \frac{1}{8}L\left(-1 - \xi + \xi^2 + \xi^3\right) \end{array} \right] \tag{4.63}$$

where $\xi = 2s/L - 1$.

At the node i we have the following relationship between local and global coordinate:

$$\left\{ \begin{array}{c} \bar{u}_i \\ \bar{w}_i \\ (d\bar{w}/ds)_i \end{array} \right\} = \left[\begin{array}{ccc} cos\phi & sin\phi & 0 \\ -sin\phi & cos\phi & 0 \\ 0 & 0 & 0 \end{array} \right] = \left\{ \begin{array}{c} u_i \\ w_i \\ \beta_i \end{array} \right\} = \mathbf{T}\mathbf{a}_i \tag{4.64}$$

Such that the global interpolation is:

$$\mathbf{u} = \left\{ \begin{array}{c} u \\ w \end{array} \right\} = [\bar{N}_1\mathbf{T} \quad \bar{N}_2\mathbf{T}]\mathbf{a^e} = N\mathbf{a^e} \tag{4.65}$$

We can obtain the strain matrix $\mathbf{B}$ by use equation 4.47:

$$\epsilon = [\bar{B}_1\mathbf{T}, \bar{B}_2\mathbf{T}]\mathbf{a^e} = B\mathbf{a^e} \tag{4.66}$$

where

$$\bar{B}_1 = \left[\begin{array}{ccc} -L^{-1} & 0 & 0 \\ -\frac{1}{2}\frac{-1+\xi}{r}sin\phi & (\frac{1}{2} - \frac{3}{4}\xi + \frac{1}{4}\xi^3)\frac{cos\phi}{r} & \frac{1}{8}L\,(1 - \xi - \xi^2 + \xi^3)\,\frac{cos\phi}{r} \\ 0 & -6\frac{\xi}{L^2} & -\frac{-1+3\xi}{L} \\ 0 & -\frac{3}{2}\,\frac{-1+\xi^2}{rL}sin\phi & -\frac{1}{4}\,\frac{-1-2\xi+3\xi^2}{r}sin\phi \end{array} \right] \tag{4.67}$$

$$\bar{B}_2 = \left[\begin{array}{ccc} L^{-1} & 0 & 0 \\ \frac{1}{2}\,\frac{1+\xi}{r}sin\phi & (\frac{1}{2} + \frac{3}{4}\,\xi - \frac{1}{4}\,\xi^3)\frac{cos\phi}{r} & \frac{1}{8}\,L\,(-1 - \xi + \xi^2 + \xi^3)\,\frac{cos\phi}{r} \\ 0 & 6\,\frac{\xi}{L^2} & -\frac{1+3\xi}{L} \\ 0 & \frac{3}{2}\,\frac{-1+\xi^2}{rL}sin\phi & -\frac{1}{4}\,\frac{-1+2\xi+3\xi^2}{r}sin\phi \end{array} \right] \tag{4.68}$$

The stiffness matrix in local coordinates:

$$\bar{K} = \int_{-1}^{1} \bar{B}^T \mathbf{D} \bar{B} \pi r L d\xi \tag{4.69}$$

On transformation, the stiffness matrix K on the global matrix is given by

$$K = \mathbf{T^T} \bar{K} \mathbf{T} \tag{4.70}$$

The corresponding nodal load from distributed load q on the element is evaluated as:

$$Q_i = T^T \int_{-1}^{1} \bar{N}_i^T q \pi r L d\xi \tag{4.71}$$

In this research the above integration is evaluated numerically on the Gauss points of the element.

4.10.2 Newmark Integration Method

The time integration scheme for the dynamic structural FEM modal in coupled fluid and structural simulation was reviewed and discussed in [38]. There are several ways to integrate the modal equations of motion. The schemes range from explicit central difference schemes to implicit schemes such as the Houbolt, Wilson-y and Newmark methods [45], [37]. The explicit scheme was found to be conditionally stable as limited by the choice of time step size. Therefore one may be forced to perform iterations of the structure solver to synchronize with the time step of the implicit flow solver. Implicit time integration schemes are unconditionally stable and among them, the classical Newmark algorithm is one of the most popular for dynamic analysis. It has been proven that the Newmark method performs best for $Dt/T < 0.01$; where T is the time period of vibrations and hence time step size must be chosen appropriately to obtain best accuracy. On the consideration of accuracy and stability, we choose the Newmark scheme as the time integration scheme for the structural equations of motion.

Considering the equation of motion:

$$m\ddot{u} + ku - f = 0 \tag{4.72}$$

Suppose that we are able to get estimates for the acceleration $\ddot{u}(t)$ and $\ddot{u}(t + \Delta t)$ both at the start and end of a general time step Δt, we could then use a Taylor series expansion to obtain estimates of displacement and velocity at time $t + \Delta t$:

$$\begin{aligned} u(t + \Delta t) &\approx u(t) + \Delta t\ddot{u}(t) + \frac{\Delta t^2}{2}[(1 - \beta_2)\ddot{u}(t) + \beta_2\ddot{u}(t + \Delta t)] \\ \dot{u}(t + \Delta t) &\approx \dot{u}(t) + \Delta t[(1 - \beta_1)\ddot{u}(t) + \beta_1\ddot{u}(t + \Delta t)] \end{aligned} \tag{4.73}$$

Here, β_1 and β_2 are two adjustable parameters that determine the nature of the time integration scheme. If we set $\beta_1 = \beta_2 = 0$ the acceleration is estimated based on its value at time t and this is known as an explicit time integration scheme. Alternatively, if we put $\beta_1 = \beta_2 = 1$, the acceleration is estimated from its value at time $t + \Delta t$ and this is known as implicit time integration.

The acceleration at the start and end of the time step is computed using the equation of motion. At time t we have:

$$\ddot{u}(t) = \frac{1}{m}[-ku(t) + f(t)] \tag{4.74}$$

while at time $t + \Delta t$, we have

$$\ddot{u}(t + \Delta t) = \frac{1}{m + k\beta_2\Delta t^2}\{-k[u(t) + \Delta t\ddot{u}(t) + \frac{\Delta t^2}{2}(1 - \beta_2)\ddot{u}(t)] + f(t + \Delta t)\} \tag{4.75}$$

This then gives us the following time stepping scheme:

- Given: $k, m, f(t), u(0), \dot{u}(0)$
- At $t = 0$ compute $\ddot{u}(0) = \frac{1}{m}[-ku(0) + f(0)]$

- At $t + \Delta t$, compute $\ddot{u}(t + \Delta t)$ according to equation 4.75. $u(t + \Delta t)$ and $\dot{u}(t + \Delta t)$ can be calculated from equation 4.73.

When $\beta_1 = 0.5$ and $\beta_2 = 0.25$, Newmark scheme is unconditionally stable so computation is always carried using these two values.

4.10.3 Numerical Experiment

The FEM program was coded in C++ and was validated by comparing with other known solutions under both cases of static and dynamic loading.

The analytical solution of an axisymmetric plate under distributed static load can be found at [55]. If a circular plate of radius a carries a load of intensity q uniformly distributed over the entire surface of the plate, and if the plate is clamped along its edge, then the deflection of the plate w is:

$$w = \frac{q}{64D}(a^2 - r^2)^2 \tag{4.76}$$

This solution is plotted along with the FEM numerical solution in Figure 4-23. The parameters used for numerical solution are:

$$\begin{aligned} a &= 10m \\ h &= 1m \\ E &= 1000Pa \\ \nu &= 0.33 \\ D &= \frac{Eh^3}{12(1-\nu^2)} = 93.5174N \cdot m \\ q &= 0.0318 \end{aligned}$$

20 elements were used in this simulation and good agreement was found between the FEM solution and analytical solution.

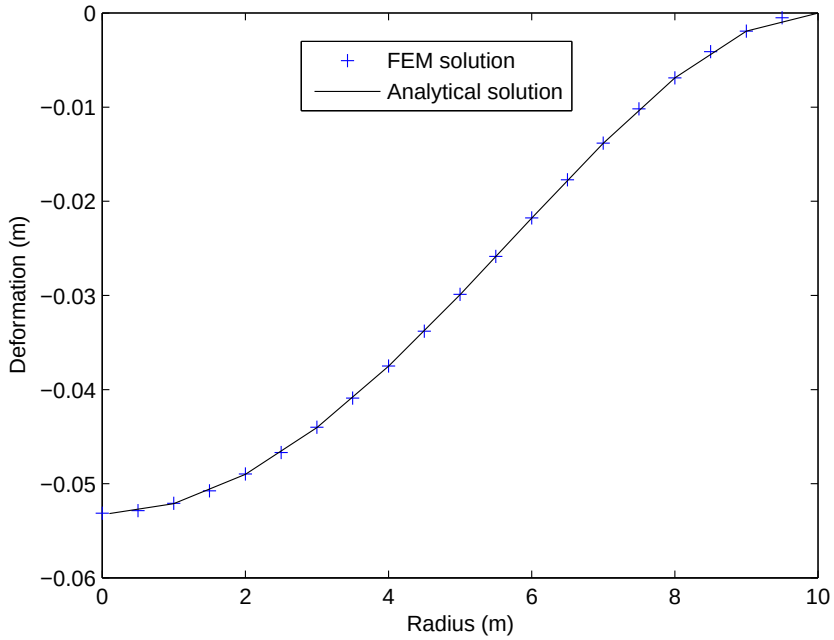

Figure 4-23: Comparison of static FEM solution vs. analytical solution.

To validate the dynamic model of current FEM code, the problem of an aluminum circular plate fully clamped around its outer boundary and subjected to transverse impulse loading was used as a test case. Such a problem was analyzed in the past and though various analytical solution exists, for simplicity, the current result was compared with the LS-DYNA numerical solution. The parameters used for this test case are:

$$
\begin{aligned}
a &= 0.1524m \\
h &= 0.003175m \\
E &= 0.71 \times 10^{11} Pa \\
\nu &= 0.33 \\
\rho &= 2700 kg/m^3 \\
f &= 444.8N
\end{aligned}
$$

The comparison of center transverse deformation was shown in Figure 4-24. A discrep-

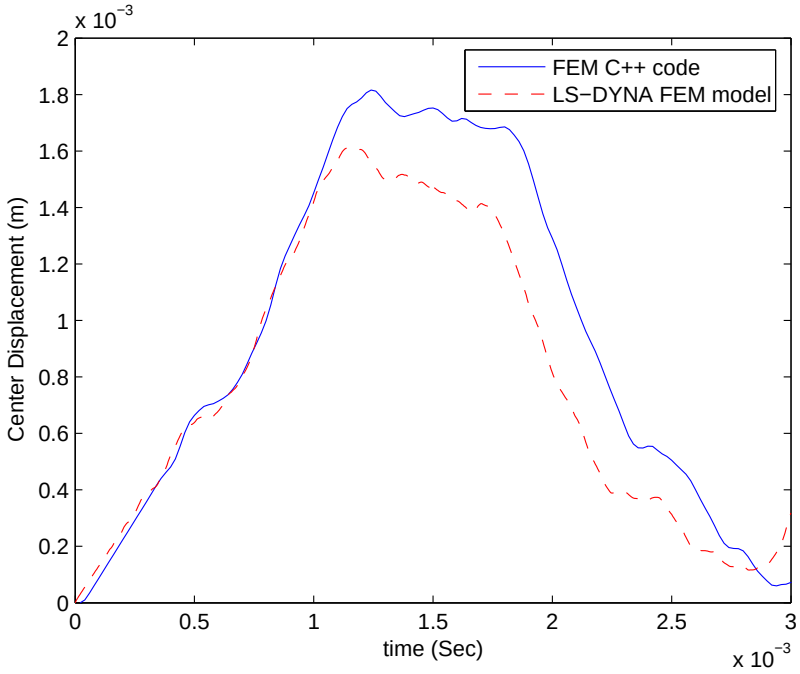

Figure 4-24: Comparison of dynamic FEM result vs. LS-DYNA result.

ancy of 10% that was observed in the comparison may have be caused by the use of triangular shell elements in the LS-DYNA model which may resulted in extra stiffness. Note that LS-DYNA result was obtained by using a central difference time integration scheme with a time step of about $5\mu s$ and in the current FEM code, Newmark integration scheme was used with a time step of $20\mu s$. The modal frequency of current the FEM code is closer to the analytical solution obtained in Chapter 3.

4.11 Discussion on Time Stepping of Coupled Solver

It is also important to mention that since the Newmark scheme performs best for $Dt/T < 0.01$, very small time step is needed to fully resolve the high frequency modes. Under the current time step of $20\mu s$, first modes are fully resolved but significant discrepancy (20%-30%) was observed for higher frequency modes. With the current closely coupled fluid-structure interaction scheme, the difficulties of resolving high frequency modes is that

if the small time step is optimized for the structure solver, numerical dissipation will rise significantly in the fluid solver. This is an issue reaming for future investigation. However, as the the goal of current research is concentrated on the flow phenomena in the fluid-structure interaction process, the time step determined by the CFL condition of the flow solver will be used in the coupled solver. Also under current configuration, experimental and analytical results both show that the amplitude of first modes is of an order or more higher than that of the second modes so such compromise of time stepping is not expected to affect the flow phenomena significantly.

4.12 Summary

An unstructured adaptive mesh flow solver, a finite element structure solver and moving mesh algorithm was implemented in the numerical simulation with good efficiency and accuracy. Specifically, a fully coupled approach was implemented on the coupled flow and structure solvers. Particulary the novel implementation of advancing front moving mesh algorithm was made possible with the implementation of a flexible and efficient *Quad-edge* data structure. Adaptive mesh refinement was introduced into the flow solver for improved accuracy as well.

Chapter 5

Numerical Results

5.1 Interaction of Shock Wave and Clamped Circular Aluminum Plate

Shock wave interaction with clamped circular plate was the topic of current research and numerical simulation was performed for a better understanding of the fluid-structure interaction phenomena.

The flow field with a radius of 0.1524 and height of $0.3048m$ was discretized by 40×40 control volumes. The aluminum plate consists of 40 axisymmetric elements, with the following material properties:

$$\begin{aligned} a &= 0.1524m \\ h &= 0.003175m \\ E &= 0.71 \times 10^{11} Pa \\ \nu &= 0.33 \\ \rho &= 2700 kg/m^3 \end{aligned}$$

Where a is the radius, h is the thickness of the plate. The flow field is initialized as :

$$\begin{cases} p = 2e5, \rho = 2.4, u = 0, v = 0 \quad upperregion : y > 0.1; \\ p = 1e5, \rho = 1.2, u = 0, v = 0 \quad lowerregion : y < 0.1. \end{cases} \tag{5.1}$$

Given the initial condition, this is virtually is mini shock tube problem as described in section 2.1.2, only differs in that the high pressure section is infinitely long such that all waves will propagating though the open end. No adaptive mesh refinement was performed during this simulation and courant number was chosen to be 0.95. Figure 5-1 shows the meshes at different simulation time steps. Figure 5-2 and Figure 5-3 show the pressure contours of the flow field at different times.

Figure 5-2.a shows the initial condition, with which a shock wave is created that will be propagating towards the plate (negative y direction). There are also expansion waves propagating towards the positive y direction which will lower the pressure on their path. Figure 5-2.b shows the pressure contour right after the shock wave has been reflected off the plate. No visible deformation was observed on the shock wave. However, there are weak expansion waves which follow immediately after the shock. It was also shown that there are expansion waves emitting around the circle near the half radius of the plate, which was excited by high order modes of plate motion. In Figure 5-2.c and Figure 5-2.d, as the reflected shock wave continues propagating upwards, the flow field was further affected by the waves generated as a result of the plate's transverse motion towards the negative y direction. It can also be noticed that as the plate starts to decelerate, it will generate compression waves propagating into the flow field. After the plate reaches its maximum displacement and starts to accelerating upwards, further pressure build up in the flow field can be observed as in figures 5-2.e and 5-2.f. The second cycle of the interaction was shown in Figure 5-3, expansion waves and compression waves were seen repeatedly propagating from the surface of the plate into the flow field.

Figure 5-4 shows the pressure history at the center of the plate together with that of a shock wave reflected off a rigid wall. The pressure reflected off the elastic plate was fluc-

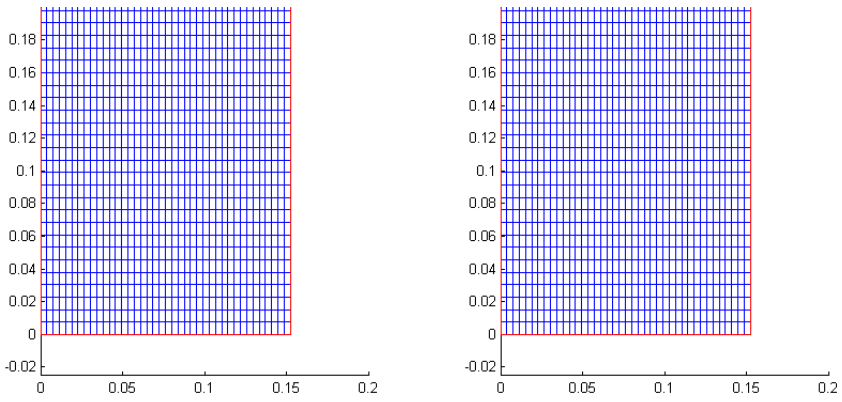

(a)

(b)

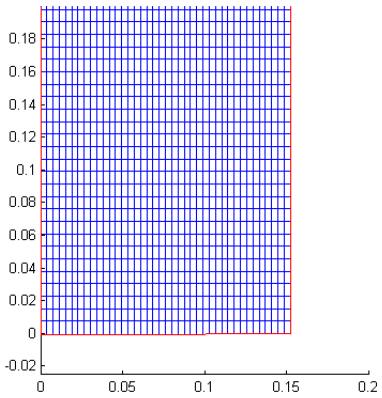

(c)

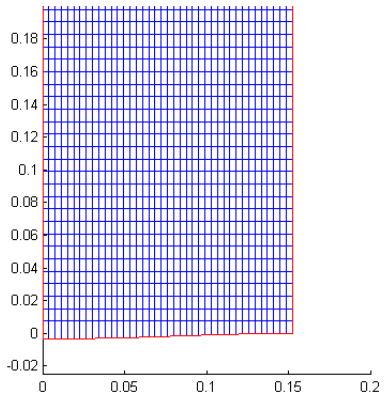

(d)

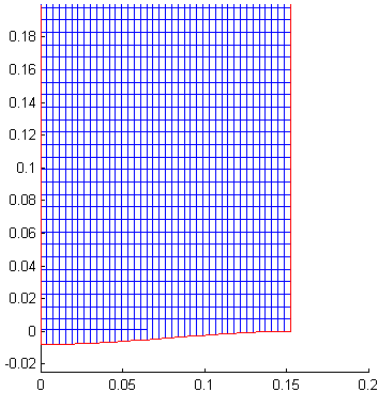

(e)

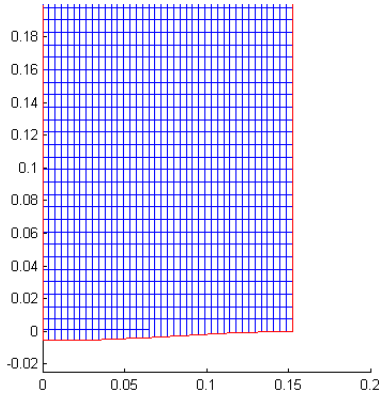

(f)

Figure 5-1: Interaction of shock wave and clamped circular aluminum plate: Mesh corresponding to Figure 5-2

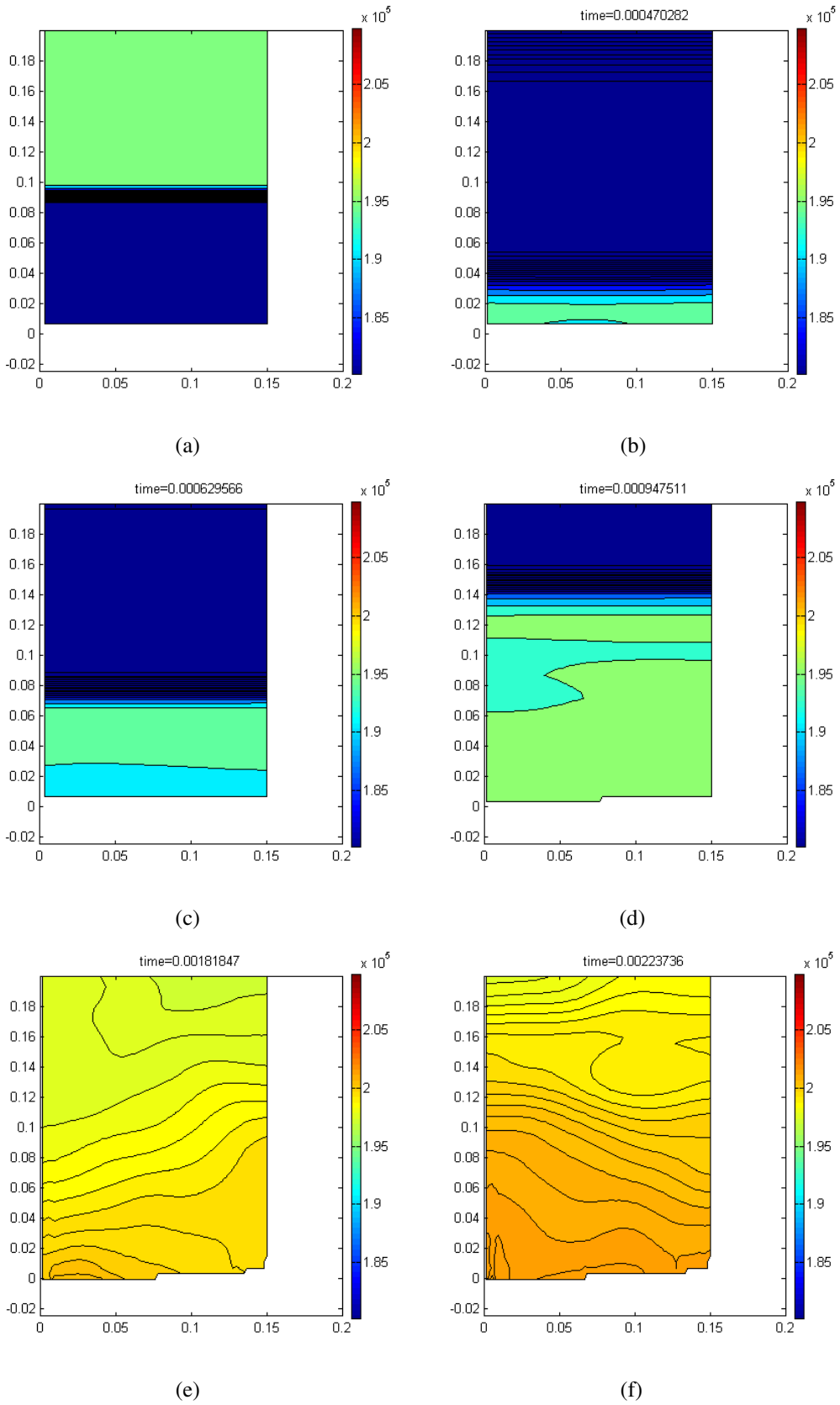

Figure 5-2: Interaction of shock wave and clamped circular aluminum plate: Pressure contour 1

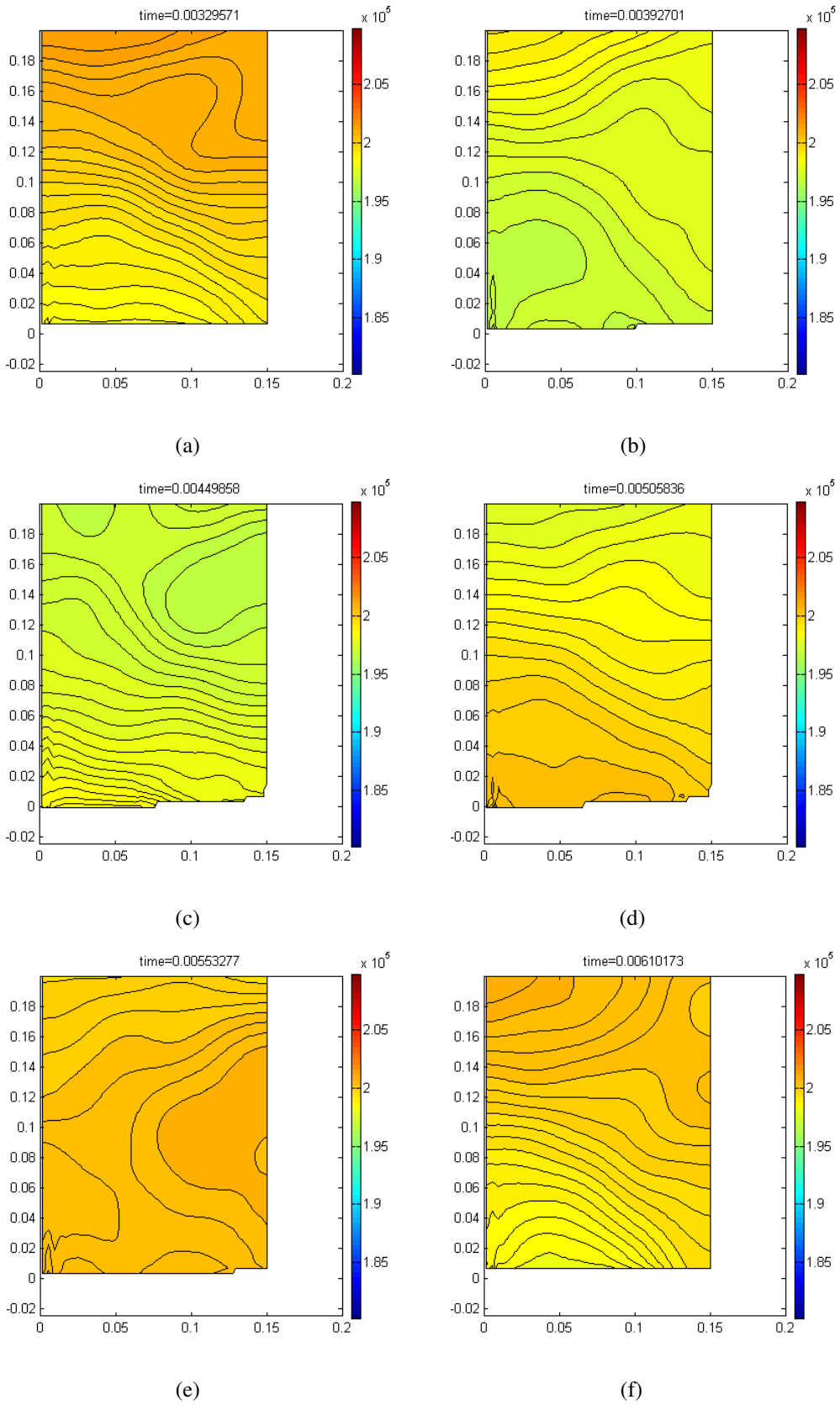

Figure 5-3: Interaction of shock wave and clamped circular aluminum plate: Pressure contour 2

tuating with a peak to peak magnitude of about $4000\ Pascal$, equivalent to about $0.6psi$. Such pressure fluctuation was related to the vibration of the plate and this dominant frequency was the same as the first modal frequency of the plate. It was also shown that the magnitude of the pressure fluctuation decreases in time, while the center transverse displacement is also decreasing, as shown in Figure 5-5. As the plate was modelled as linear elastic, such damping phenomena were solely attributed to the fluid-structure interaction. Due to the fact that the fluid structure interaction at the rear (non impact) side surface of the plate was not modelled in this simulation, it is expected that such damping effect will double if the interaction is fully modelled on both sides of the plate. Other factors such as viscosity and plastic dissipation may also contribute to the damping effect.

It should also be noticed that the plate reaches its maximum transverse displacement at the center, while the maximum stress occurs next to the edge where the plate is fully clamped. The maximum stress history was plotted in Figure 5-6.

Strain on the plate surface can be obtained from the numerical results at the element's gauss integration point. The stress on the surface of the plate can be calculated by:

$$\sigma_r = -\frac{6M_r}{h^2} \tag{5.2}$$

where σ_r is the stress along the radial direction, M_r is the bending momentum acting along the radial direction, which was obtained in the numerical simulation. In the case of thin circular plate, M_r can be expressed as:

$$M_r = -D(\frac{d^2w}{dr^2} + \frac{\nu}{r}\frac{dw}{dr}) \tag{5.3}$$

Details of the above relationship can be found in [55]. Once the surface stress σ_r is known, we can further calculate the surface strain along radial direction as:

$$\epsilon_r = \frac{(1-\nu^2)\sigma_r}{E} \tag{5.4}$$

where ν is the plate's Poisson's ratio and E is the modulus of elasticity.

Surface strain history at $r = 0.127m$ was plotted in Figure 5-8 and its corresponding transverse displacement was plotted in Figure 5-7. Strain signal history shows that several different modes have contributed to the fluctuation. The Power spectrum of the strain signal was calculated and plotted in Figure 5-9. Notice that as the time step used in numerical simulation is not a constant, before performing the Fourier transformation, sampling was performed by linearly interpolating the strain signal on constant time intervals. The 145 time steps originally obtained from simulation result was extended to a total of 256 uniform intervals. As the total time duration is $20ms$, the frequency windows of FFT is $50Hz$. From the power spectrum we can obtain three peaks at $350Hz, 1400Hz, 3100Hz$, which is slightly different than the analytical result and experimental data, which maybe attribute to numerical errors and the inadequate resolution of FFT power spectrum.

Further attempts were made to compare this numerical surface strain history along the radial direction with the experimental results obtained with a slightly higher pressure, as shown in Figure 2-10. Experimental result shows that the strain signal was fluctuating at a principle frequency of second modal frequency, while the numerical result failed to predict such frequency. This can be attributed to the factor that current plate is modelled as perfect linear elastic, while the actual plate is exhibiting significant plasticity. It was observed that permanent deflection occurs during the experiment, as shown in the experimental strain history. While the plate is plastic and experiencing permanent deformation, most of the kinetic energy transferred from the shock wave to the plate was absolved by the plastic deformation. As a result, the plate was vibrating at a dominant frequency of higher modes. To isolate the effect of first mode vibration, surface strain is filtered with a forth order Butterworth high pass filter at a cutoff frequency of 1000Hz. The filtered strain signal is shown in Figure 5-10, with most of the first mode frequency component being eliminated. As expected, comparing this filtered signal with the experimental data, the fluctuation of the strain is about 80×10^{-6} peak to peak, which is about the same magnitude as obtained from the experimental result.

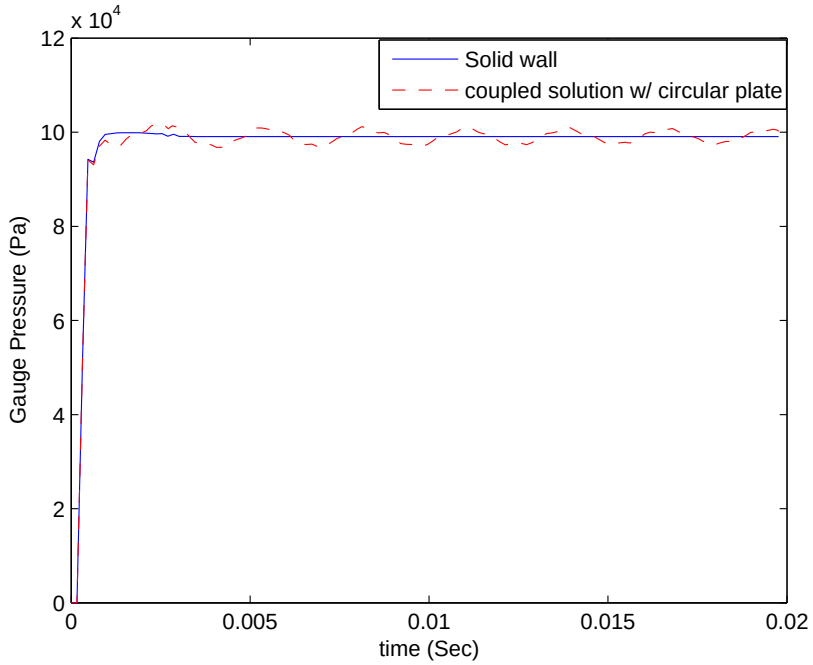

Figure 5-4: Interaction of shock wave and clamped circular aluminum plate: Center pressure loading

Interestingly, by comparing the power spectrum in Figure 5-9 with the power spectrum obtained experimentally as in Figure 2-17, we can see that the magnitude of the composite plate's high modes vibration is significantly smaller than that of the computational result of an aluminum metallic plate, with both scaled by their corresponding first modal amplitude. We can make such comparison as strain signals were obtained at the same radial location and if we assume the material's non-linearity is minor such that the magnitude of each modes can be individually evaluated. Also as observed in the experiment, the composite plate did not suffer any plastic permanent deformation, no first modal suppression exists in this case, which is also shown from the strain signal. Excluding all of the above mentioned uncertainties, we can come to the conclusion that the composite does behaves uniquely on high modes damping and such damping can be attributed to that the composite plate is viscoelastic while the metallic plate is not.

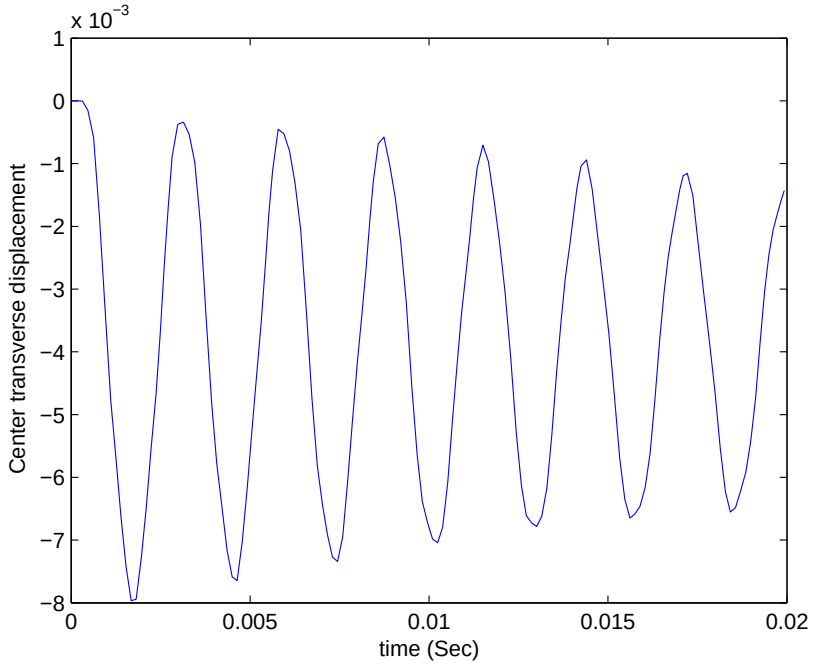

Figure 5-5: Interaction of shock wave and clamped circular aluminum plate: Center transverse displacement

5.1.1 Grid Dependency and Validation

Gird dependency was conducted to ensure that the physical phenomena simulated numerically through out this research do not rely on the resolution of the numerical grid. An initial mesh of 21×21 was chosen to perform the same numerical simulation in the case of shock wave interaction with a clamped circular aluminum plate. All initial conditions, boundary conditions and physical properties are set to be the same as those used in numerical simulation with a 41×41 initial mesh. The mesh at different time levels are plotted in Figure 5-11. The corresponding pressure contours are plotted in Figure 5-12. Because the different time steps used in numerical simulations performed with different meshes, the time levels in these plots are not exactly the same as those plotted in Figure 5-1, 5-2 and 5-3. However, closest time levels are chosen for comparison if exists. Comparing pressure contours in these two simulations performed with different meshes, as those in Figure 5-2.a,b,d,e, and Figure 5-3.c,d compared with Figure 5-12.a-f, it can be seen that the pressure

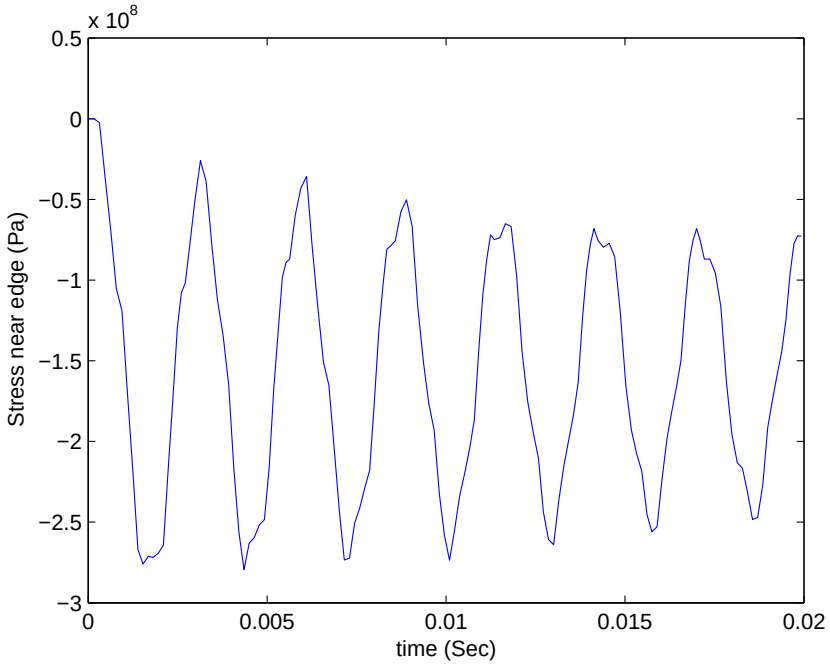

Figure 5-6: Interaction of shock wave and clamped circular aluminum plate: Stress history near the clamped edge

contours with finer meshes may have a slightly higher spatial resolution, other than that the pressure contours are in very similar pattern and of the same magnitude at approximate the same time levels.

Such grid independency can be further illustrated by Figure 5-13 and 5-14. In Figure 5-13, the pressures at the center of the plate are plotted for both the 21×21 and 41×41 meshes. In Figure 5-14 the center transverse displacements of the plate are plotted and compared. It can be seen that numerical results obtained from different meshes are in excellent agreement.

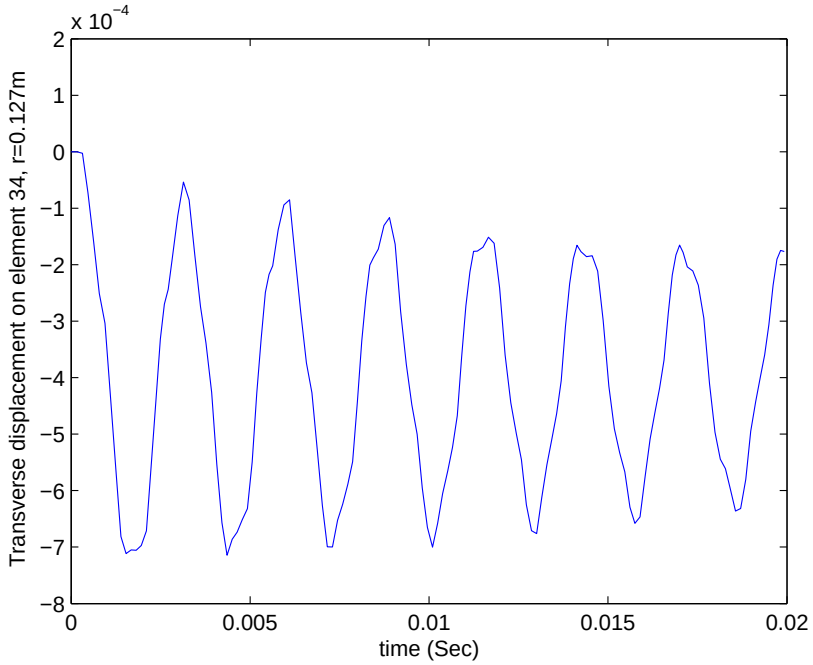

Figure 5-7: Interaction of shock wave and clamped circular aluminum plate: Transverse displacement at r=0.127

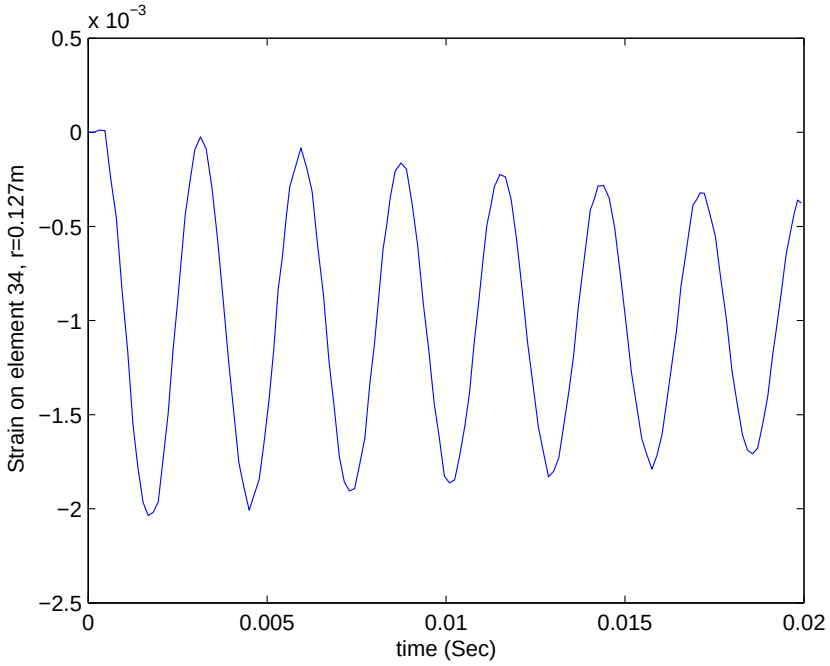

Figure 5-8: Interaction of shock wave and clamped circular aluminum plate: Surface strain at r=0.127.

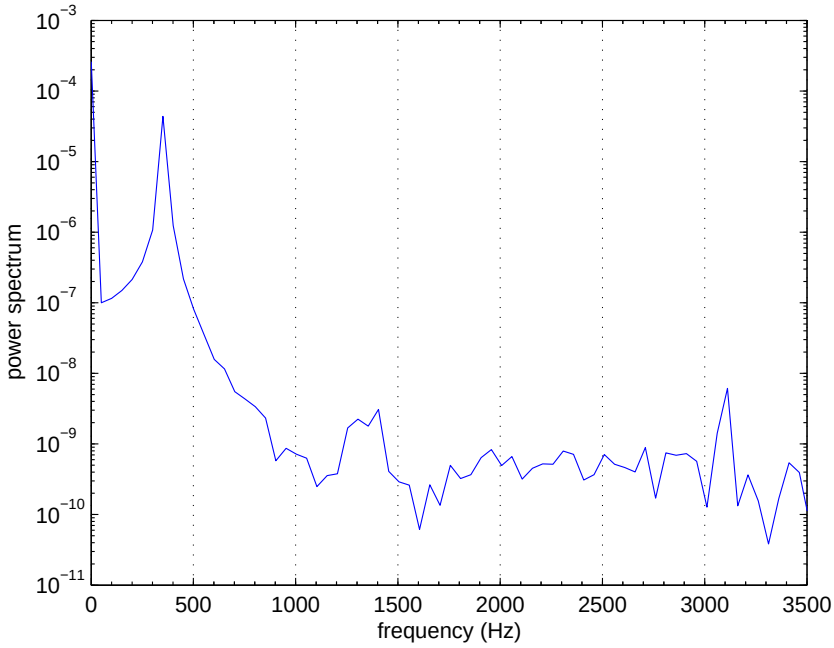

Figure 5-9: Interaction of shock wave and clamped circular aluminum plate: Power Spectrum of strain at r=0.127.

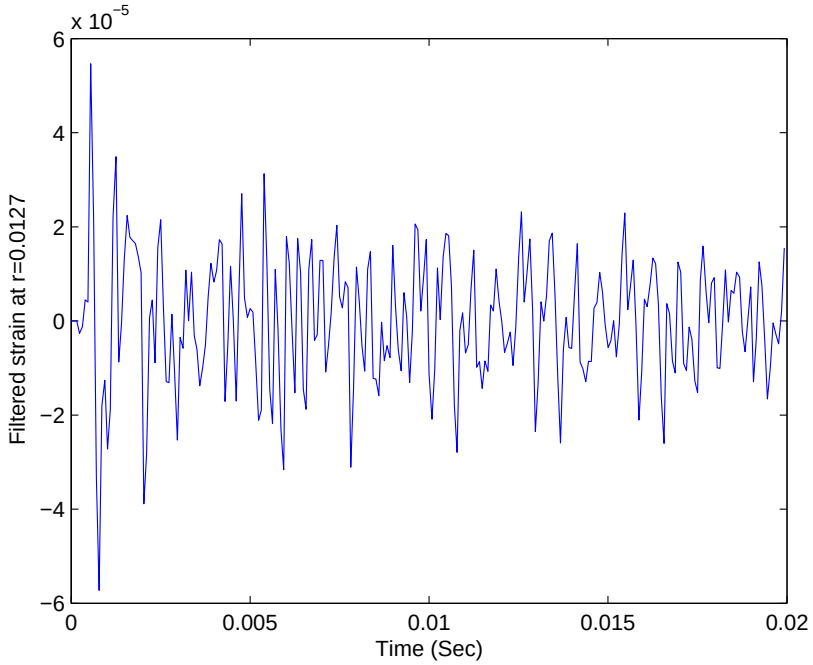

Figure 5-10: Interaction of shock wave and clamped circular aluminum plate: Filtered surface strain at r=0.127.

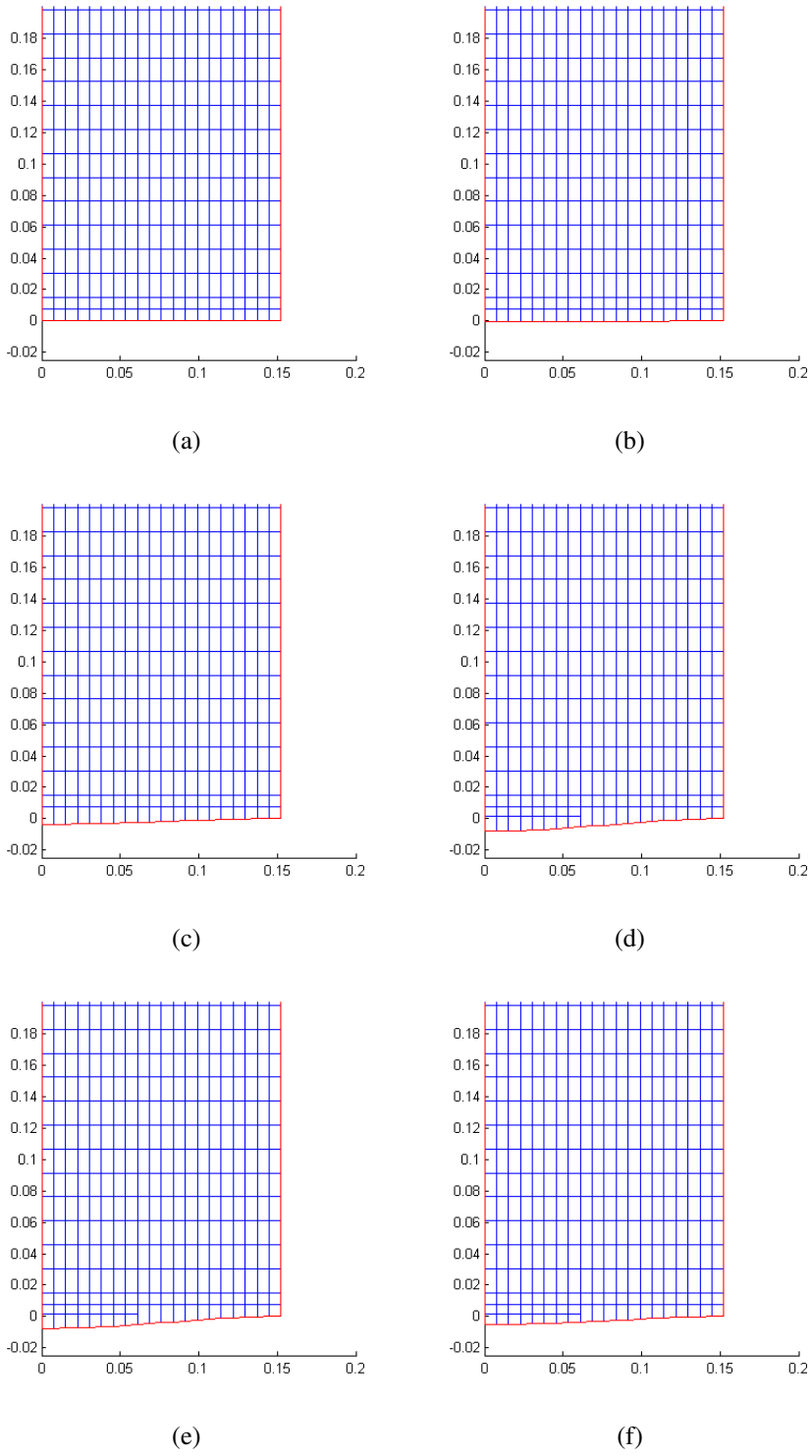

Figure 5-11: Interaction of shock wave and clamped circular aluminum plate: Mesh corresponding to Figure 5-12. Initial mesh set as 21×21

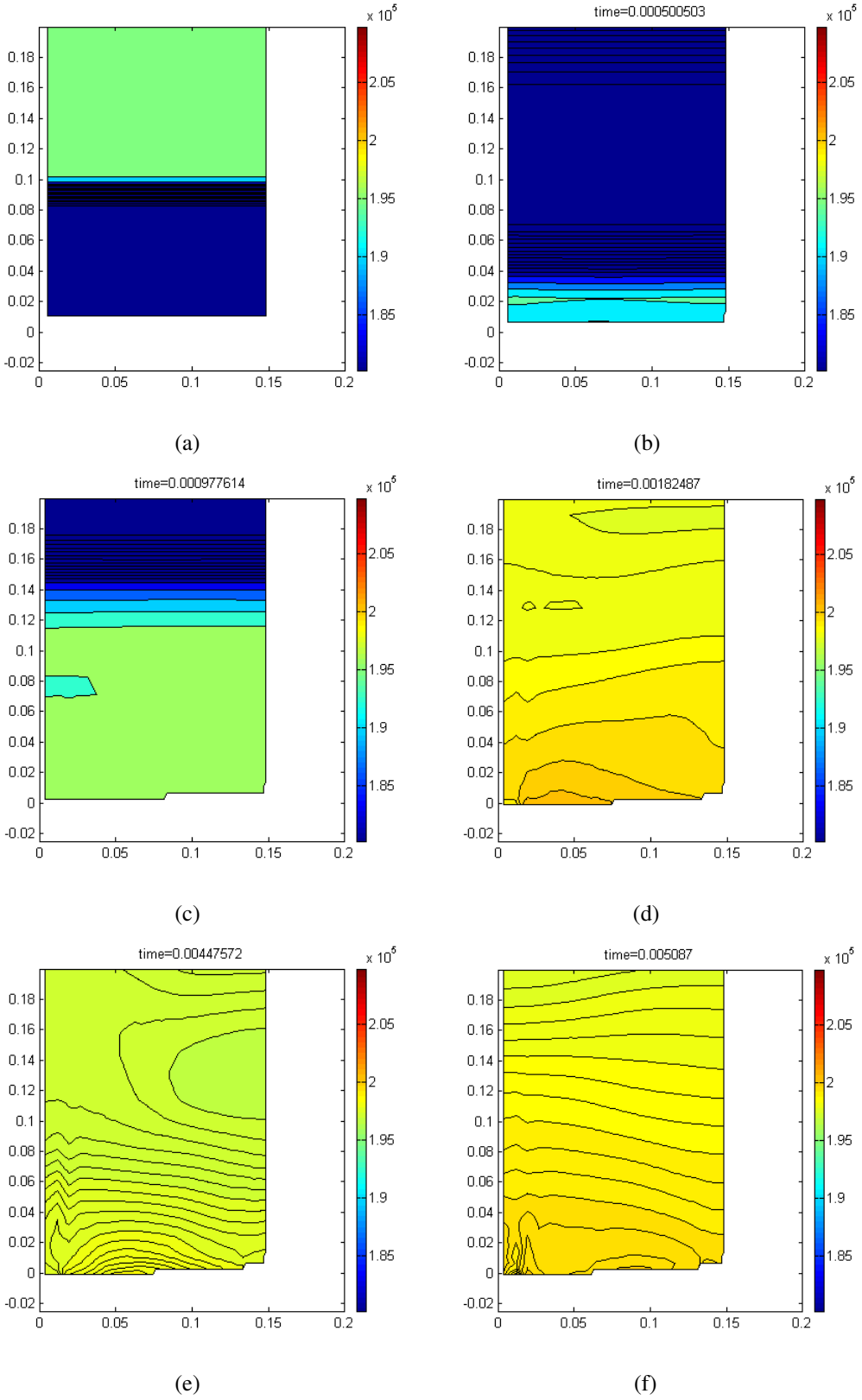

Figure 5-12: Interaction of shock wave and clamped circular aluminum plate: Pressure contour 1. Initial mesh set as 21×21

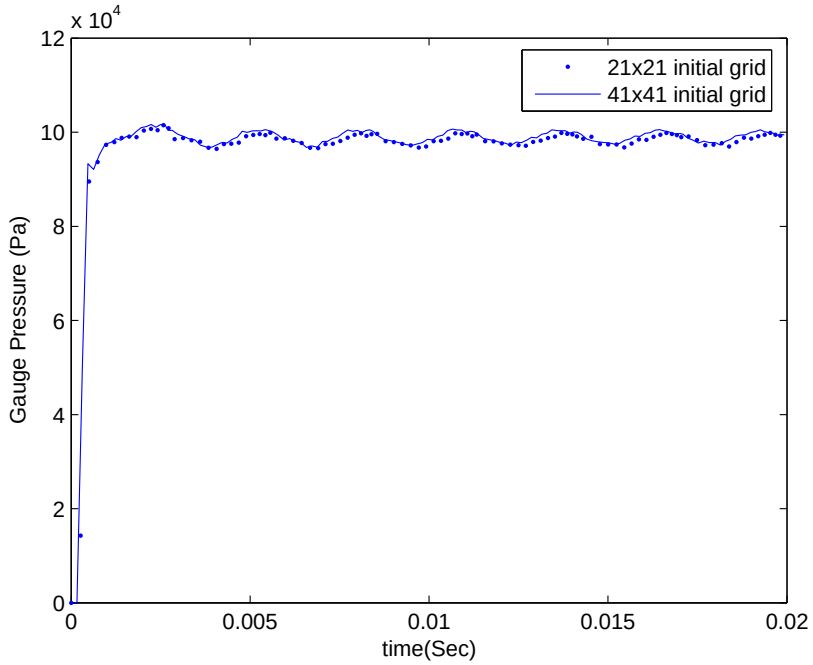

Figure 5-13: Interaction of shock wave and clamped circular aluminum plate: Comparison of center pressure loading obtained with different meshes

5.2 Interaction of Shock Wave and Clamped Circular Stainless Steel Plate

In this simulation the same mesh, initial and boundary conditions are used as those used in the previous section. The only difference is that here a stainless steel plate is used and the corresponding material properties are:

$$
\begin{aligned}
a &= 0.1524m \\
h &= 0.001588m \\
E &= 2.05 \times 10^{11} Pa \\
\nu &= 0.3 \\
\rho &= 7800 kg/m^3
\end{aligned}
$$

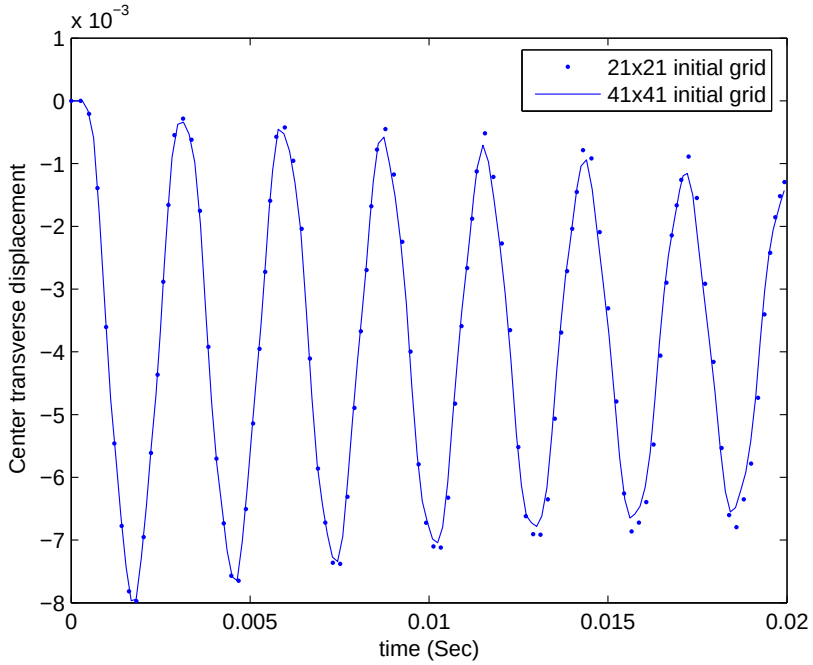

Figure 5-14: Interaction of shock wave and clamped circular aluminum plate: Comparison of center transverse displacement obtained with different meshes.

Simulation meshes and corresponding pressure contours at different time levels are plotted in Figure 5-15 and 5-16. The shock wave reflection and acoustic wave generation patterns are similar to the case of aluminum plate, except that different time scales are involved because the stainless steel plate used in this simulation has lower natural frequencies because of its lower flexural rigidity.

The pressure history at the plate center is plotted in 5-17 along with the case with shock wave reflection off a rigid wall. Pressure fluctuation is also observed in this case. Compare with the case of aluminum plate, the magnitude of this pressure fluctuation is larger, with a lower characteristic frequency. This frequency is about 170Hz, which is the first natural frequency calculated theoretically as listed in Table 3.4.

The center transverse displacement history of the plate is plotted in Figure 5-18. The maximum displacement is about 23mm and the dominant frequency is also about 170Hz. It also appear that other frequency modes also exist. The maximum stress on the plate

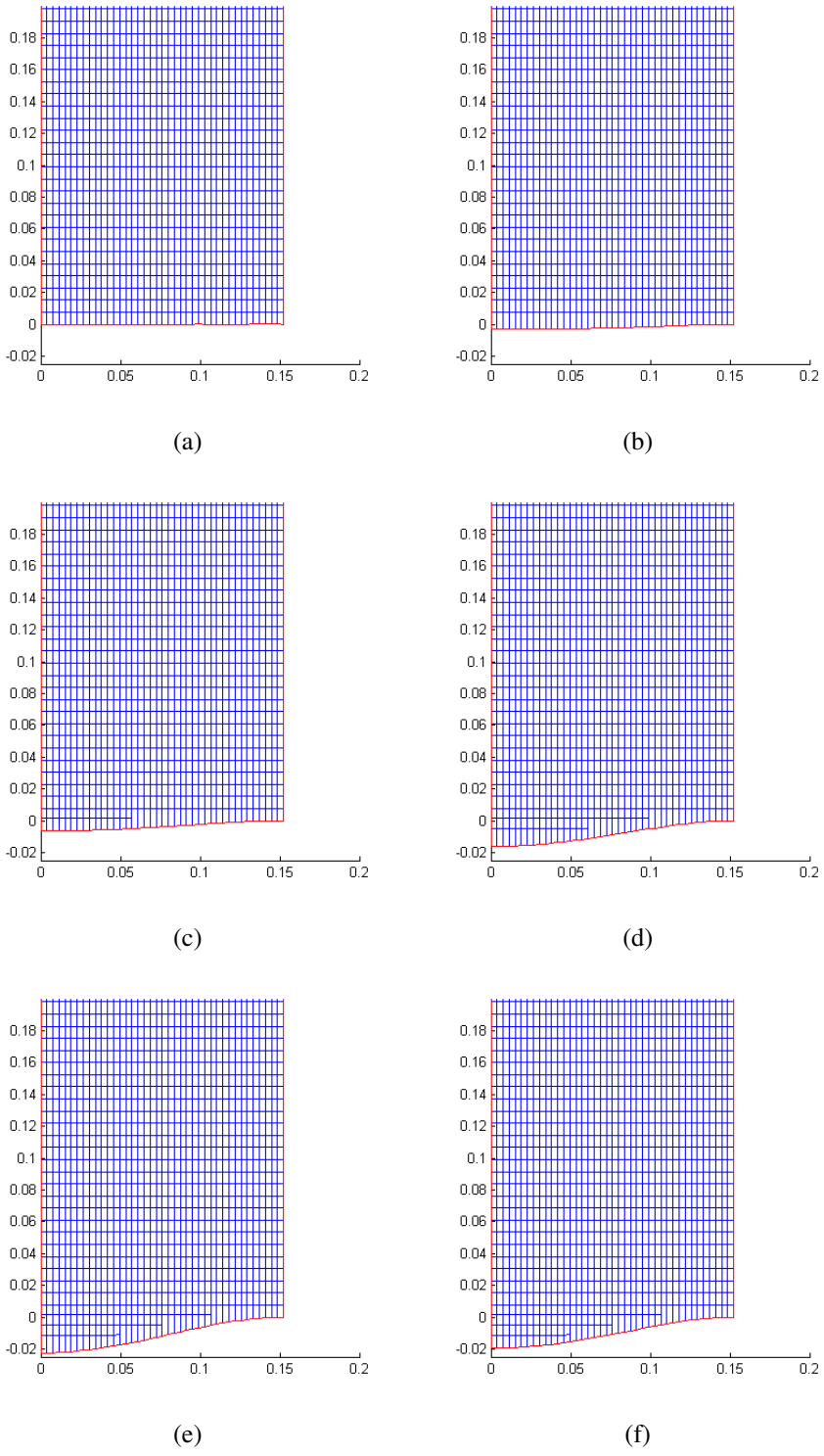

Figure 5-15: Interaction of shock wave and clamped circular stainless steel plate: Mesh corresponding to Figure 5-16

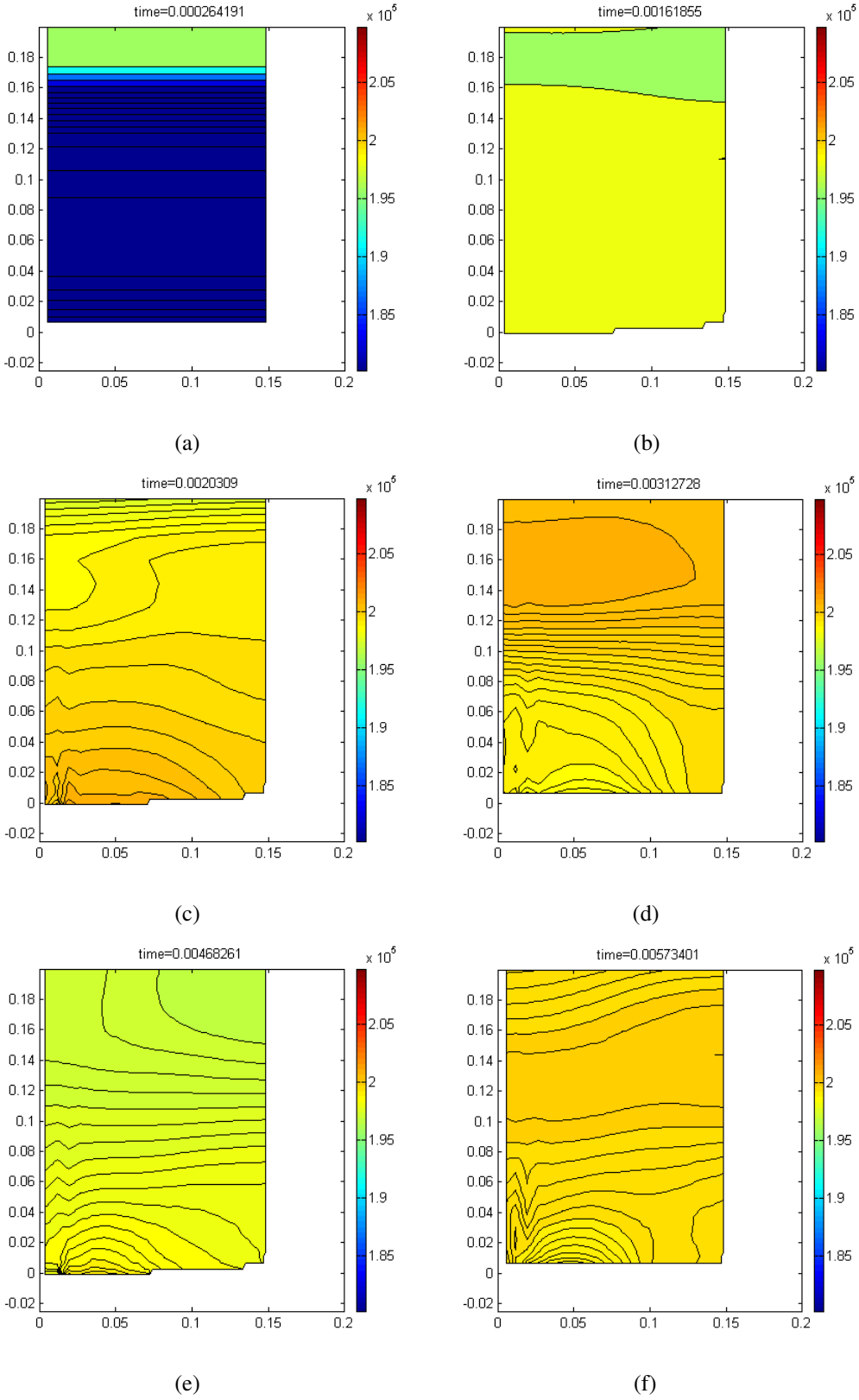

Figure 5-16: Interaction of shock wave and clamped circular stainless steel plate: Pressure contour.

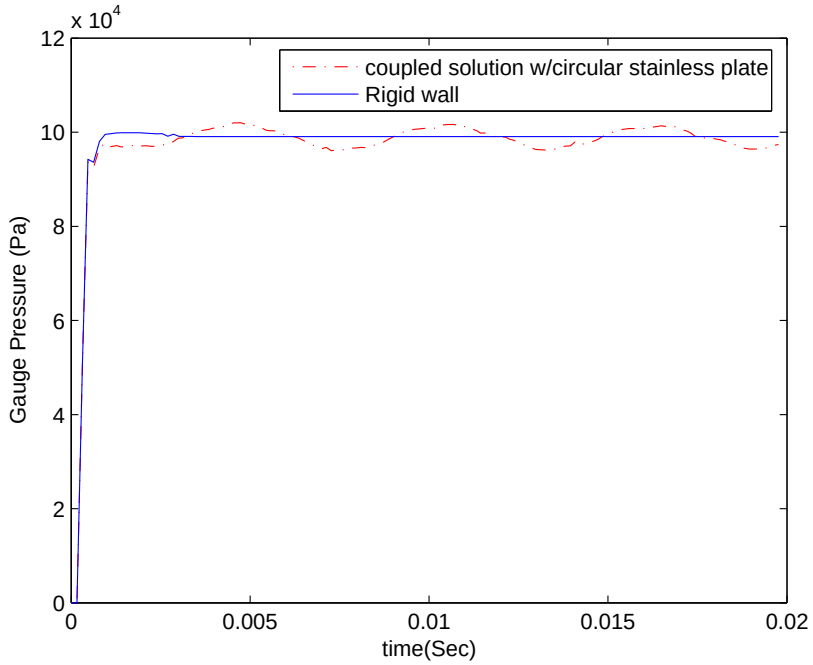

Figure 5-17: Interaction of shock wave and clamped circular stainless steel plate: Center pressure loading

can be obtained from Figure 5-19 and it is about $11.5 \times 10^8 Pa$. This stress value already exceeds the yielding stress of stainless steel at $255 \times 10^6 Pa$. Such that we would expect that permanent plastic deformation will occur during the experiment and actually permanent deformation is observed in the experiment.

Because of the permanent plastic deformation, we would also expect that the vibration of this stainless steel plate is also highly non-linear. Stain history and its power spectrum at locations near strain gage #1, #2 are plotted in Figure 5-20 to 5-23. In Figure 5-20, strain history of the plate at strain gage location #1 is plotted and we can see that this strain fluctuates at around the plate's first natural frequency. We can also see smaller fluctuations and as a result the power spectrum shown in Figure 5-22 clearly demonstrates 3 major peaks at 170Hz, 650Hz and 1500Hz. These frequencies agrees well with those calculated through other methods as listed in Table 3.4. Compare with the experiment result in Figure 2-13, we observed similar discrepancy as discussed in the aluminum plate case. Again this

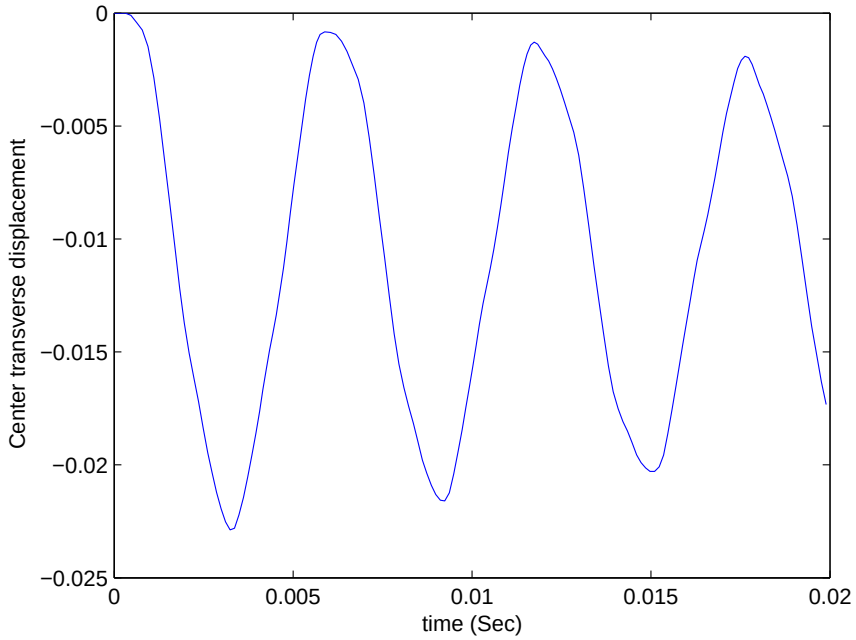

Figure 5-18: Interaction of shock wave and clamped circular stainless steel plate: Center transverse displacement

can be attributed to the plastic permanent deformation of the plate and the non-linearity of this vibration.

However, strain history of the plate at strain gage location #2 has totally different behavior than that obtained at location #1. We can see that the dominant frequency is about 650Hz, the second natural frequency of this stainless steel plate. Actually strain gage #2 is located very close to $r = 0.618a$, which is the nodal point of the first mode vibration at 170Hz. So the strain history plotted here is almost not affect by the first mode vibration of the plate, neither significantly altered because of the permanent deformation of the stainless plate. Not surprisingly, the peak to peak strain fluctuation magnitude agrees well with those obtained from experiment, about 600μ. Power spectrum of this simulated strain shows 3 major peak at 650Hz, 1500Hz and 2700Hz, which corresponding to the second, third and fourth natural frequencies of the plate.

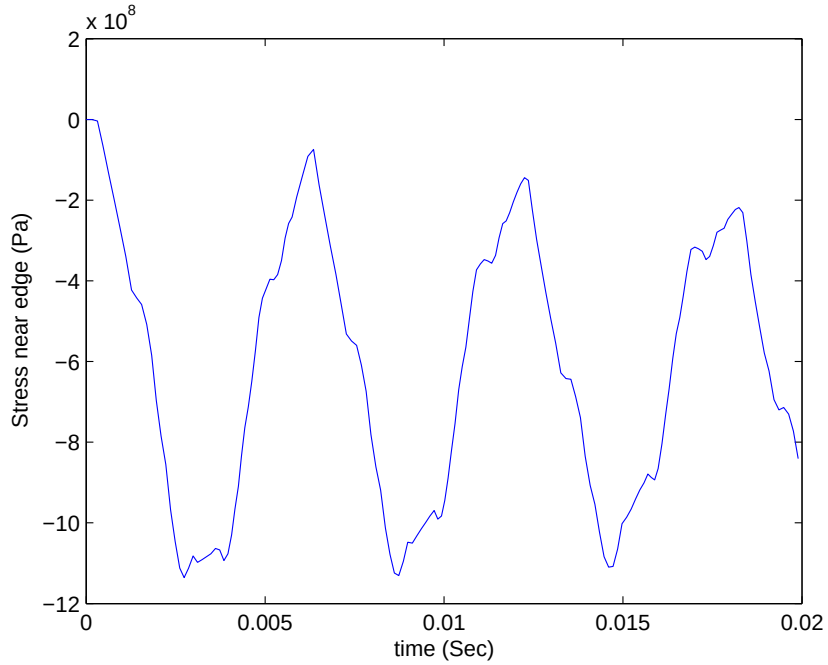

Figure 5-19: Interaction of shock wave and clamped circular stainless steel plate: Stress history near the clamped edge

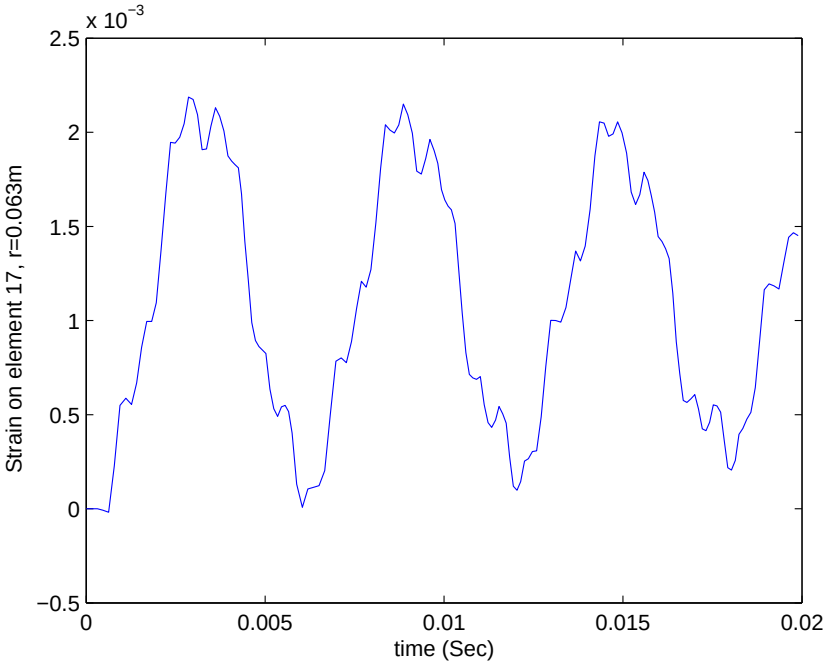

Figure 5-20: Interaction of shock wave and clamped circular stainless steel plate: Surface strain at r=0.063m.

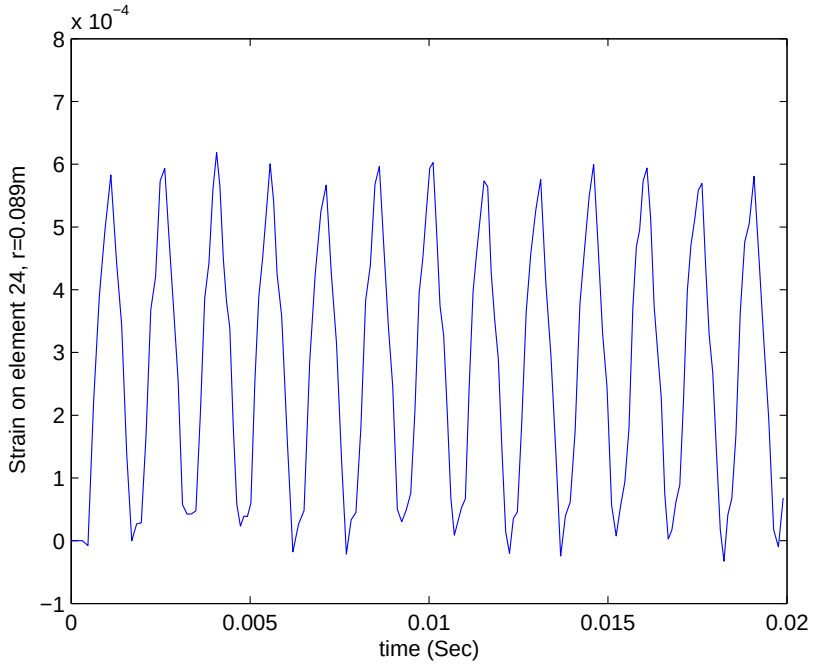

Figure 5-21: Interaction of shock wave and clamped circular stainless steel plate: Surface strain at r=0.089m.

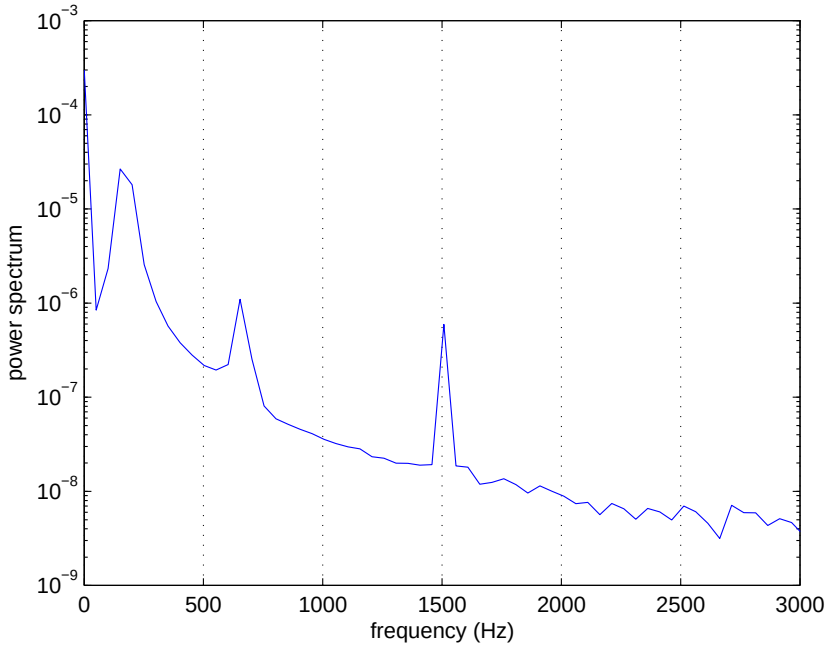

Figure 5-22: Interaction of shock wave and clamped circular stainless steel plate: Power Spectrum of strain at r=0.063m.

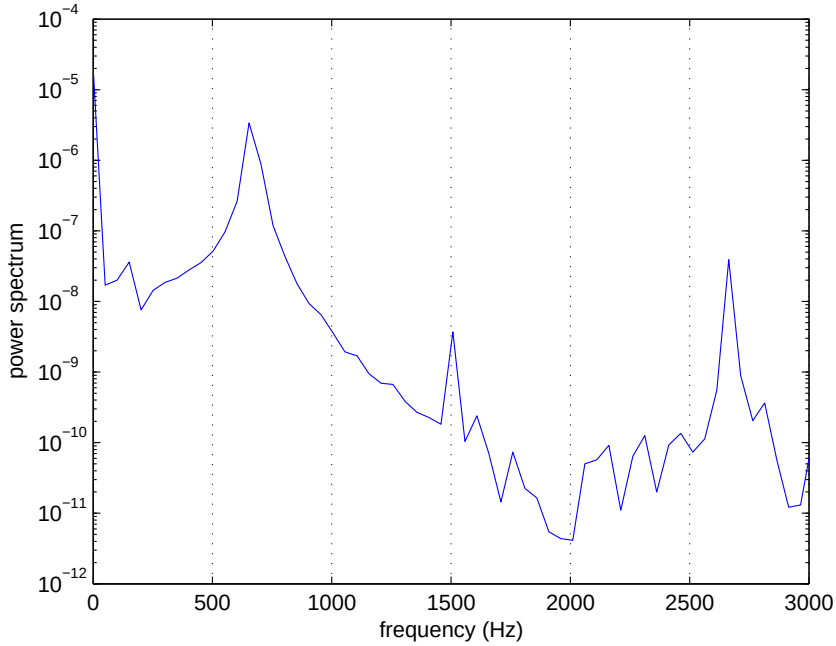

Figure 5-23: Interaction of shock wave and clamped circular stainless steel plate: Power Spectrum of strain at r=0.089m.

5.3 Interaction of Shock Wave and Clamped Circular Quasi-isotropic Composite Plate

In this simulation the same mesh, initial and boundary conditions are used as those used in the case of metalic plate. The material properties used for the quasi-isotropic composite plate are:

$$
\begin{aligned}
a &= 0.1524m \\
h &= 0.005588m \\
E &= 0.33 \times 10^{11} Pa \\
\nu &= 0.25 \\
\rho &= 1811 kg/m^3
\end{aligned}
$$

Simulation meshes and corresponding pressure contours at different time levels are plotted in Figure 5-24 and 5-25. The shock wave reflection and acoustic wave generation patterns are similar to the case of metallic plate, except that different time scales are involved because the composite plate used in this simulation has higher natural frequencies.

The pressure history at the plate center is plotted in 5-26 along with the case with shock wave reflection off a rigid wall. Pressure fluctuation is also observed in this case. The magnitude of this pressure fluctuation is small because this plate has a larger flexural rigidity and the center transverse displacement is small compare with other metallic plates. The fluctuation frequency is about 480Hz, which is the first natural frequency calculated theoretically as listed in Table 3.5.

The center transverse displacement history of the plate is plotted in Figure 5-27. The maximum displacement is about 3mm only, about an order of magnitude smaller than that of the stainless steel plate. Because this displacement is so small, we would expect that the composite plate will not be damaged in this case. The time history of stress near the edge of the plate is plotted in 5-29. The maximum stress is about $7 \times 10^7 Pa$, which is much lower than the normal ultimate stress of the glass fiber, at about $2 \times 10^9 Pa$. Because during the experiment no plastic deformation or material damage is involved, less discrepancy between experiment and numerical simulation should be expected comparing with the cases with the metallic plates.

The strain time history is plotted in Figure 5-28 and its corresponding power spectrum is shown in Figure 5-30. The strain fluctuations observed here is about 2×10^{-3}. This strain history can be further compared with the experimental result as plotted in Figure 2-16, where the measured strain fluctuation from strain gage #1 is about 10^3. However, in the experimental result, significant damping effect is observed, even though the acoustic pressure fluctuation is small. This maybe caused by the internal damping of the plate itself, related to the composite's unique material properties. It is very likely energy may be dissipated between the fiber and matrix interface.

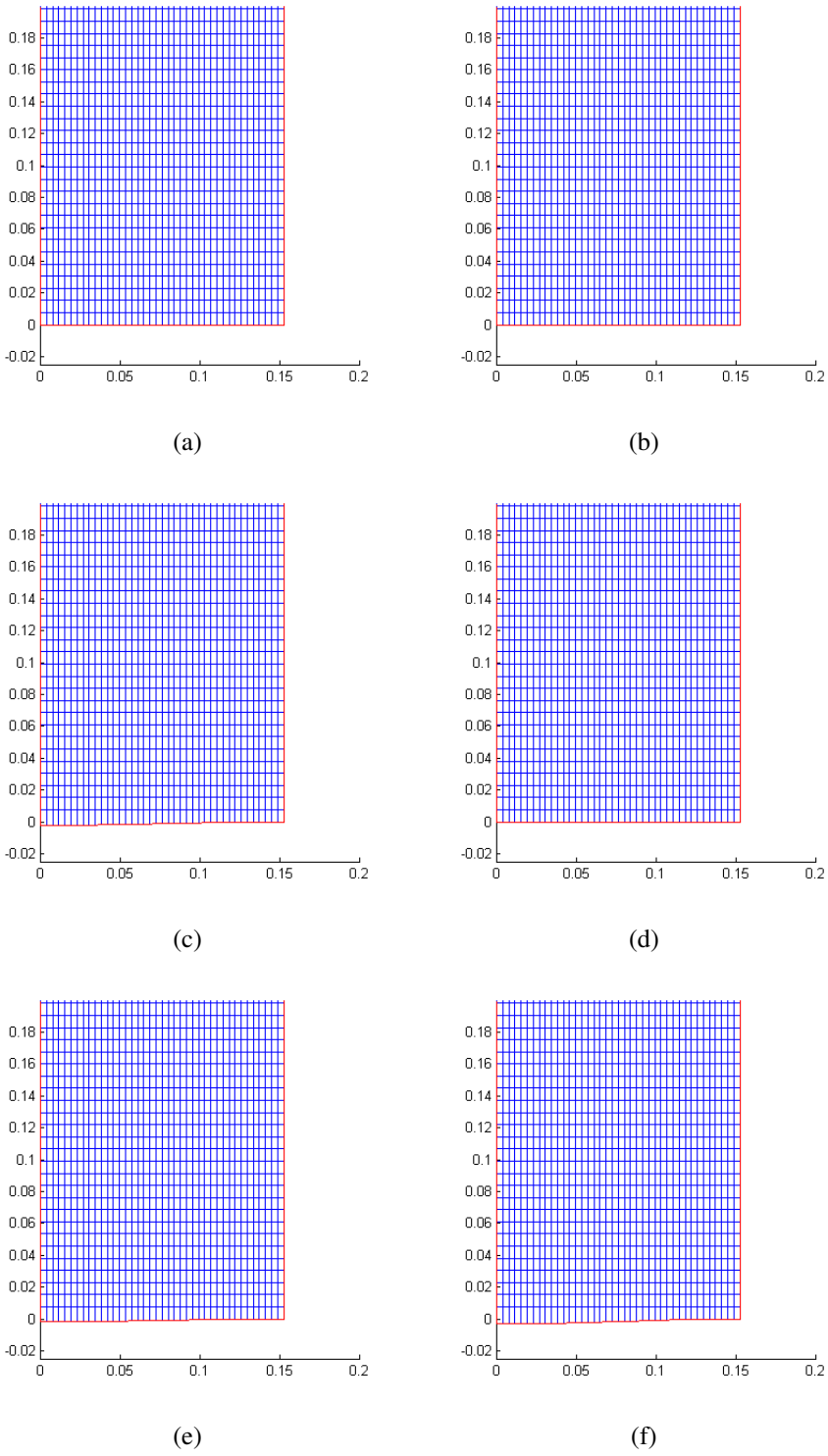

Figure 5-24: Interaction of shock wave and clamped circular quasi-isotropic composite plate: Mesh corresponding to Figure 5-25

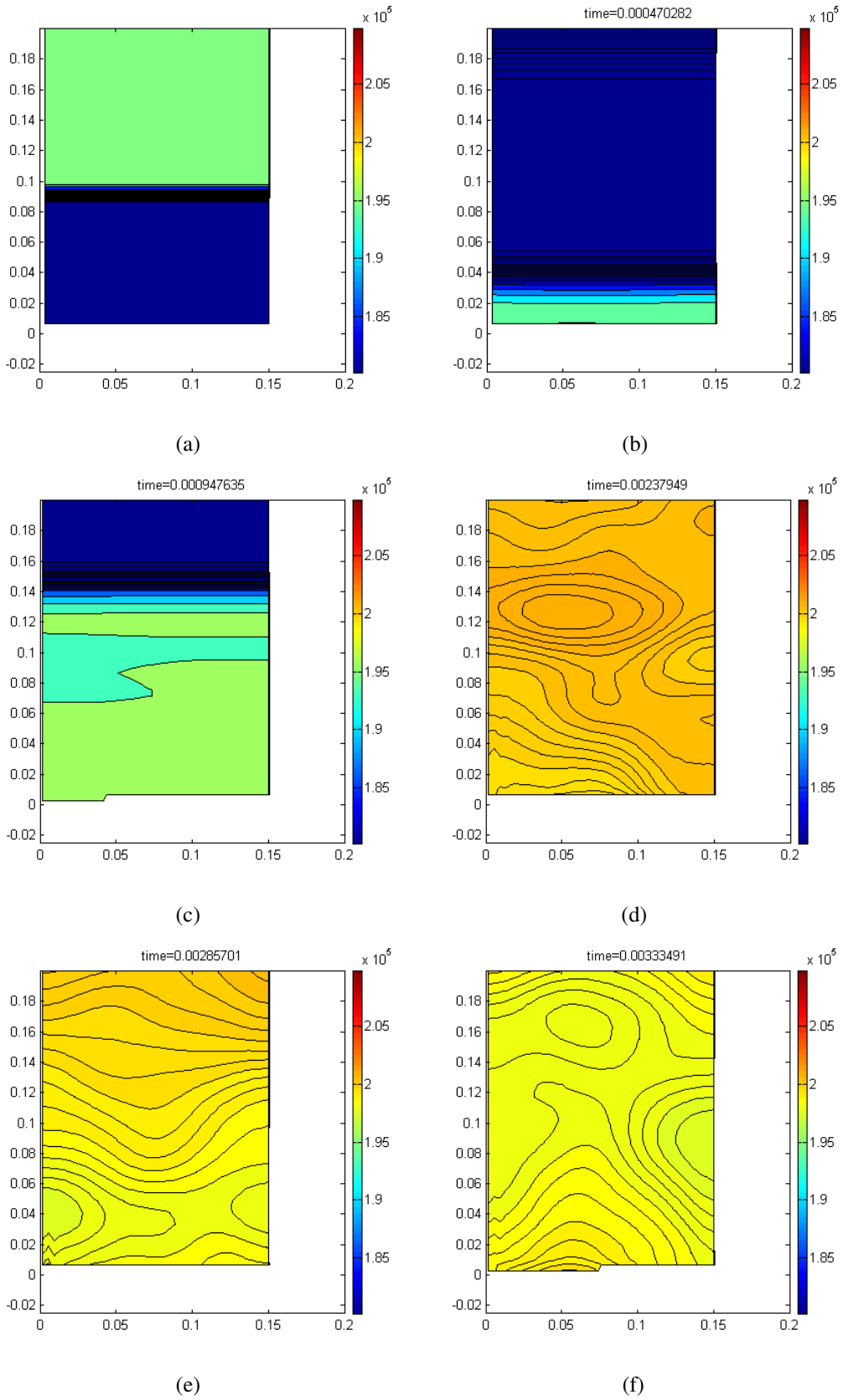

Figure 5-25: Interaction of shock wave and clamped circular quasi-isotropic composite plate: Pressure contour.

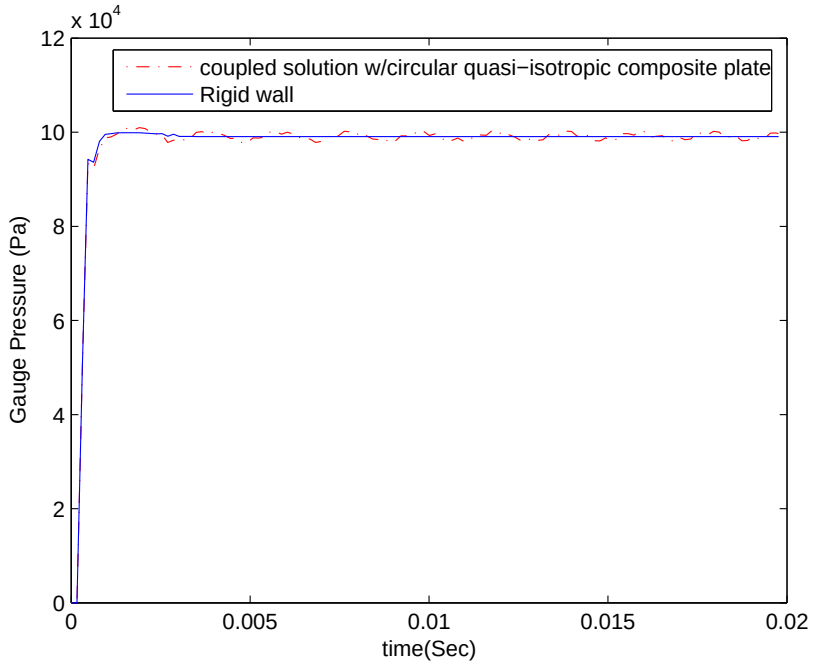

Figure 5-26: Interaction of shock wave and clamped circular composite plate: Center pressure loading

The power spectrum of the strain is plotted in Figure 5-30. Three major peaks are observed at about 480Hz, 1900Hz and 4300Hz. These peaks agree well with those calculated in Table 3.5. The dominant frequency observed in the experiment is at about 400Hz, which is lower than calculated. This suggests that the actual composite plate may has a lower flexural rigidity than what used in the calculation, which was calculated using a simply formula for isotropic material. Further calculations showing that a reduced flexural rigidity at 80% of the original values used will yield better agreement between experiment and numerical simulations.

5.4 Interaction of Blast Wave and Sandwich Plate

To further demonstrate the complicated process of fluid-structure interaction, numerical simulation was performed on the mutual interaction between blast wave and a circular

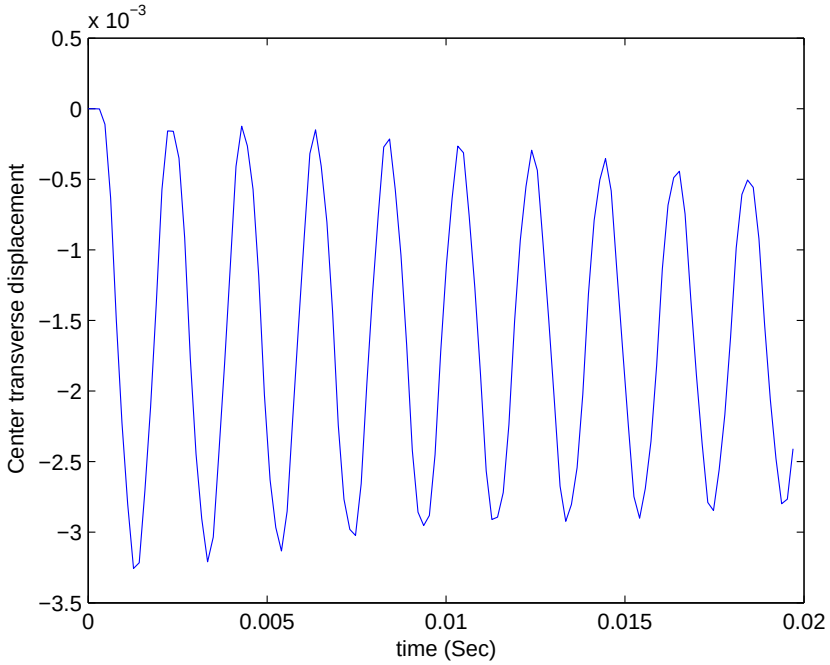

Figure 5-27: Interaction of shock wave and clamped circular composite plate: Center transverse displacement

sandwich plate fully clamped at its edge.

The blast wave was initialized with a high pressure core at $0.2m$ above the center of sandwich plate. The radius of the core is $0.04m$, with a core pressure of $2 \times 10^8 Pa$ and a core density of $2460kg/m^3$. The sandwich plate was in corrugated configuration, with the top and bottom surface made of $1.59mm$ steel plate. The sandwich core was made of aluminum, with an element thickness of $0.794mm$. A total of 120 elements were used to model this sandwich plate as illustrated in Figure 5-33.a .

The pressure contour at different time steps are plotted in Figure 5-31 and Figure 5-32. Complicated pressure waves were seen in the pressure contour, as the blast loading on the plate possesses more unevenness. The pressure loading on the center of the sandwich plate is plotted in Figure 5-34 and compared with the pressure loading of a blast wave impacting on a rigid wall. At the instant the blast wave hit the sandwich plate, the plate starts to deform and as a result blast wave is not fully reflected off the plate as in the case of rigid

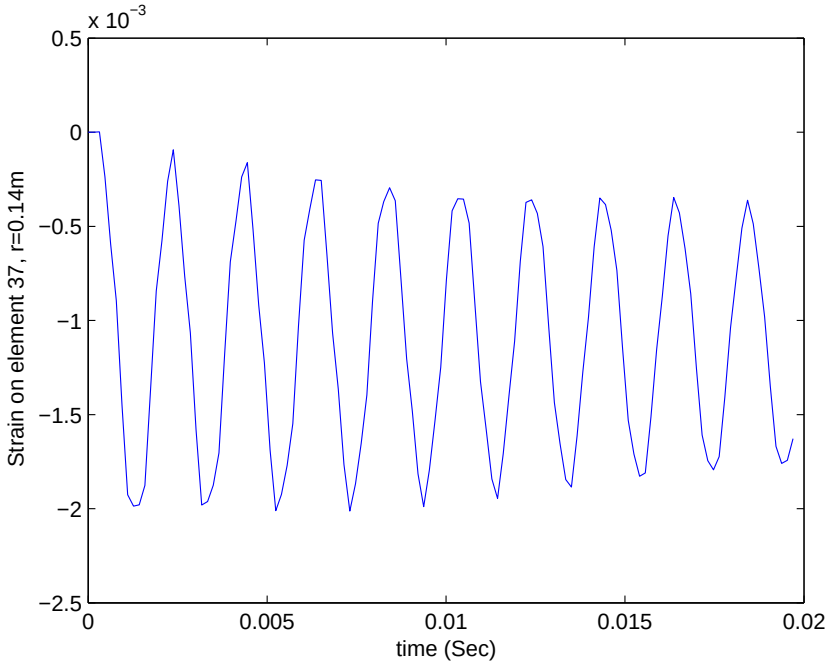

Figure 5-28: Interaction of shock wave and clamped circular quasi-isotropic composite plate: Surface strain at r=0.14m.

wall. Because of that the pressure loading is smaller than fully reflected pressure.

It was mentioned in literature [47] that under shock loading, a sandwich plate will be subject to a phenomena called as *core compression phase*. At the instant the blast wave hit the sandwich plate, the outer plate experiencing face-on impact will gain a velocity while the core and the other side of the plate is remaining stationary. This phase was then followed by a *bending and stretching phase*, while the whole plate will have a uniform velocity except at the support. From Figure 5-33, we can see that the two face plates of the sandwich plate possess different deformation profile, but, in a closely coupled fashion, both phases mentioned above took place simultaneously.

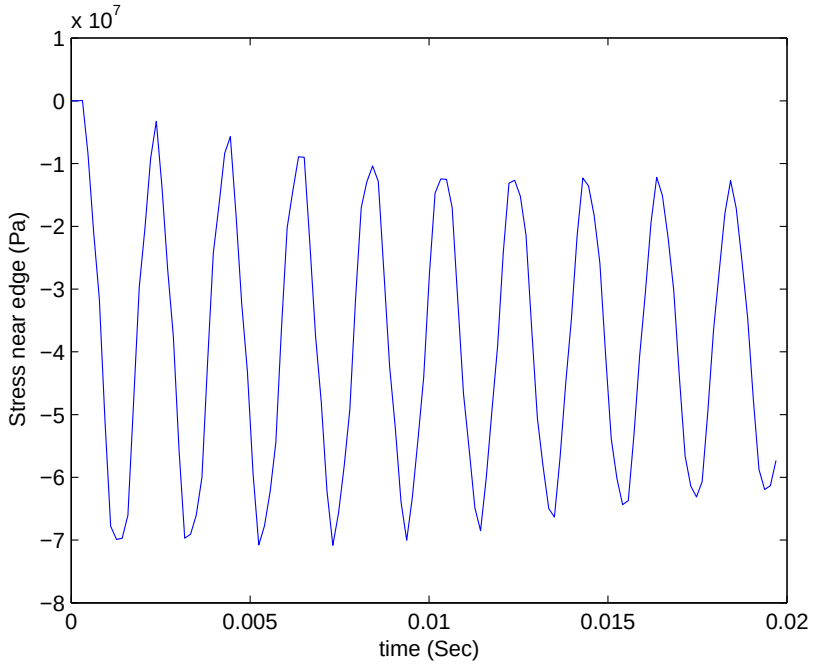

Figure 5-29: Interaction of shock wave and clamped circular quasi-isotropic composite plate: Surface stress at r=0.14m.

5.5 Summary

In this chapter numerical simulations were performed on the interactions between shock wave, blast wave with various plates. Numerical results are further validated by theoretical analysis, experiment data and results from other numerical simulation. Grid dependency study is performed and results show that the physical phenomena and quantities are independent of the numerical grid chosen in the simulation. Numerical simulations confirmed existing theories and experimental observations. With the aid of numerical simulation, complicate flow phenomena and structure vibration patterns are observed, which are beyond the capabilities of the current experimental technique. Current numerical simulation also successfully modelled the aero-acoustic damping effects on the structure, which do not exist in the common numerical model.

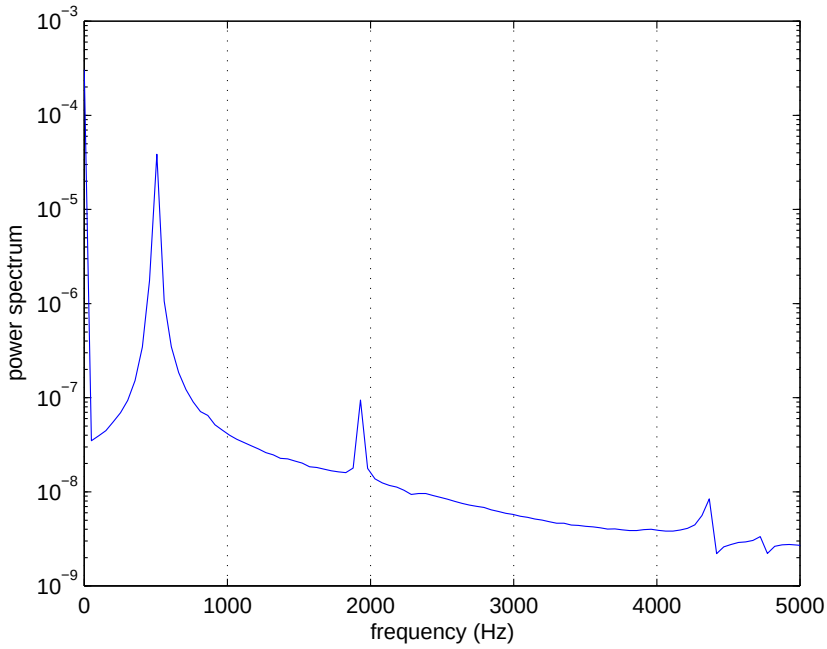

Figure 5-30: Interaction of shock wave and clamped circular quasi-isotropic composite plate: Power Spectrum of strain at r=0.14m.

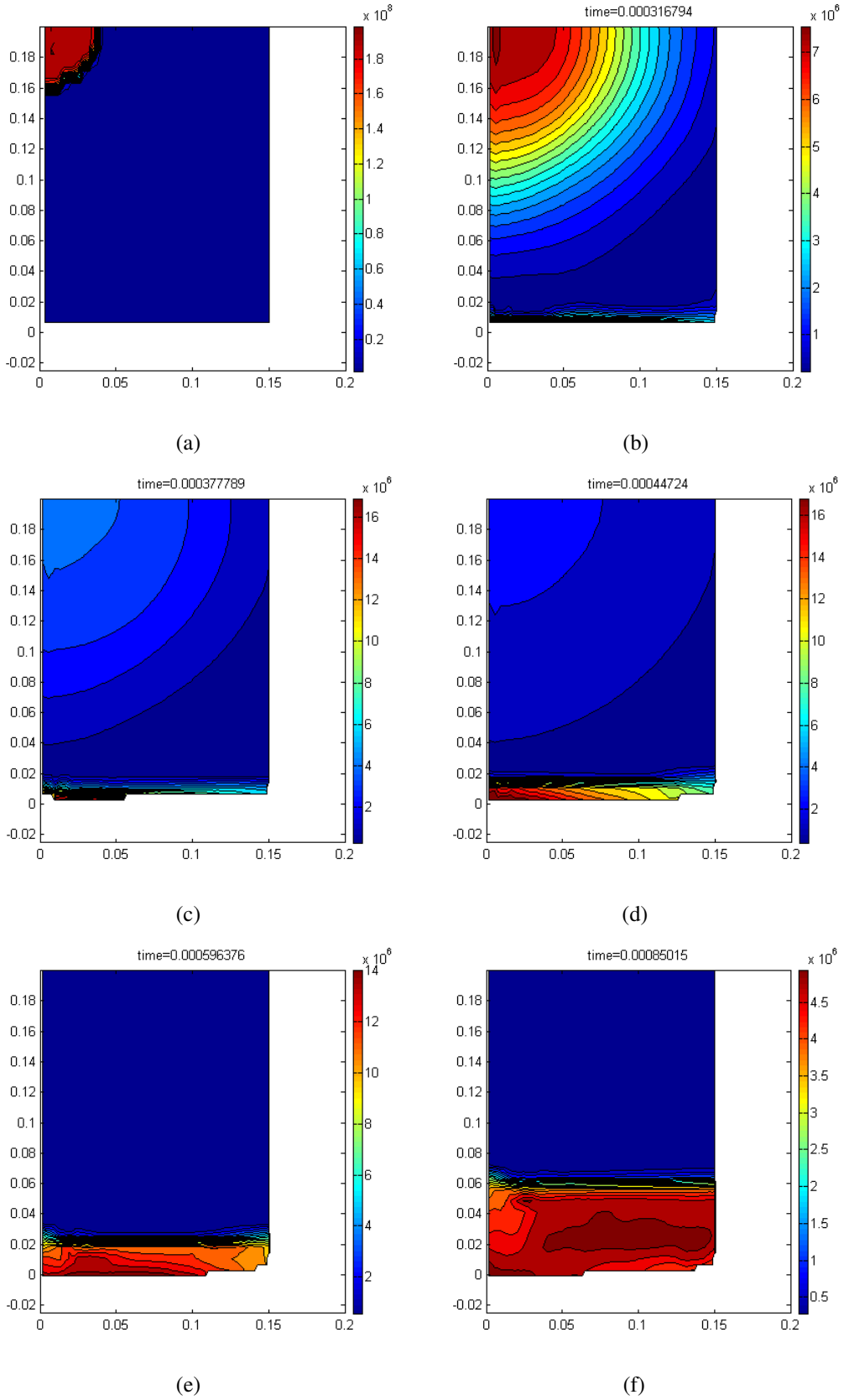

Figure 5-31: Interaction of blast wave and circular sandwich plate: Pressure contour 1

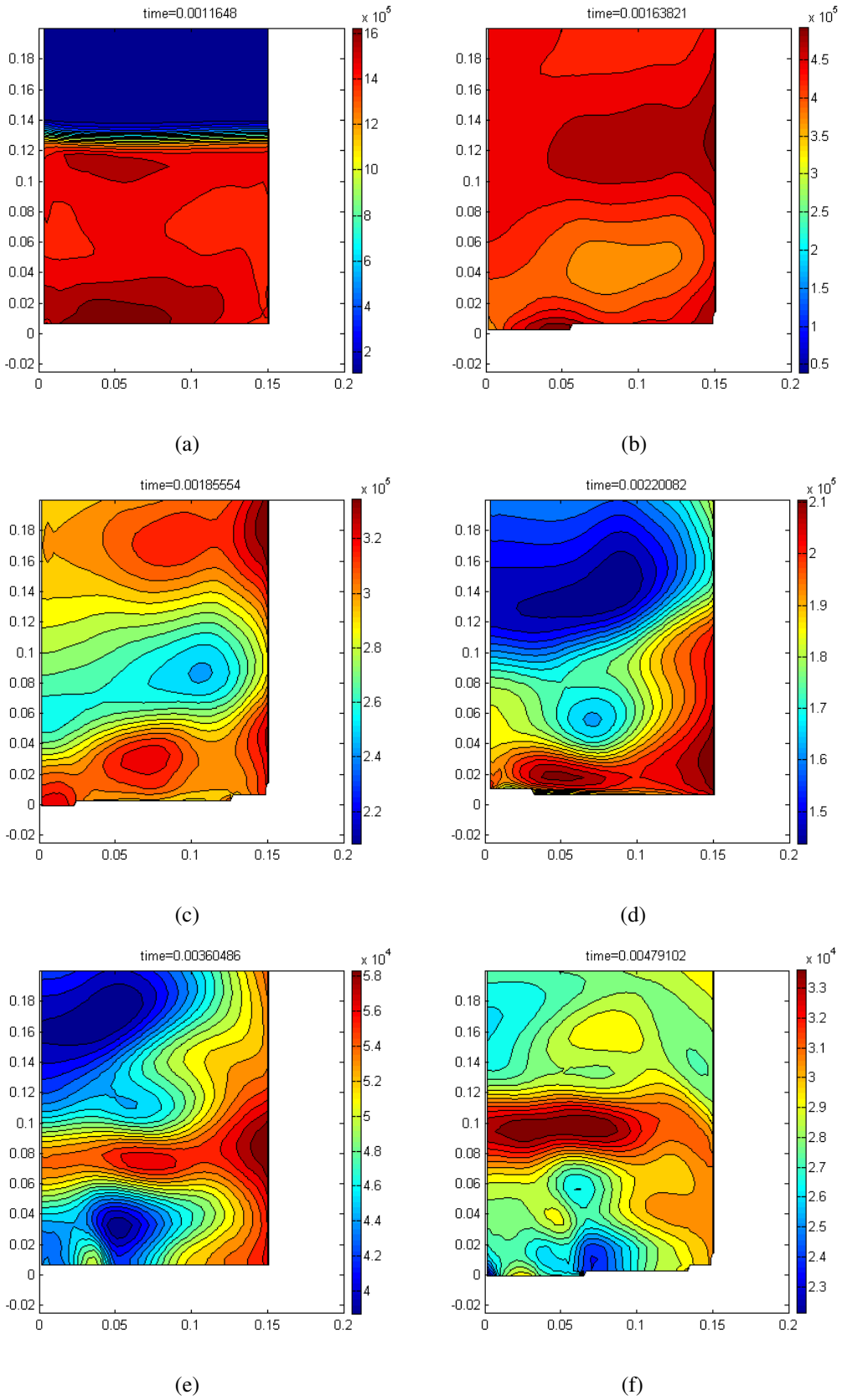

Figure 5-32: Interaction of blast wave and circular sandwich plate: Pressure contour 2

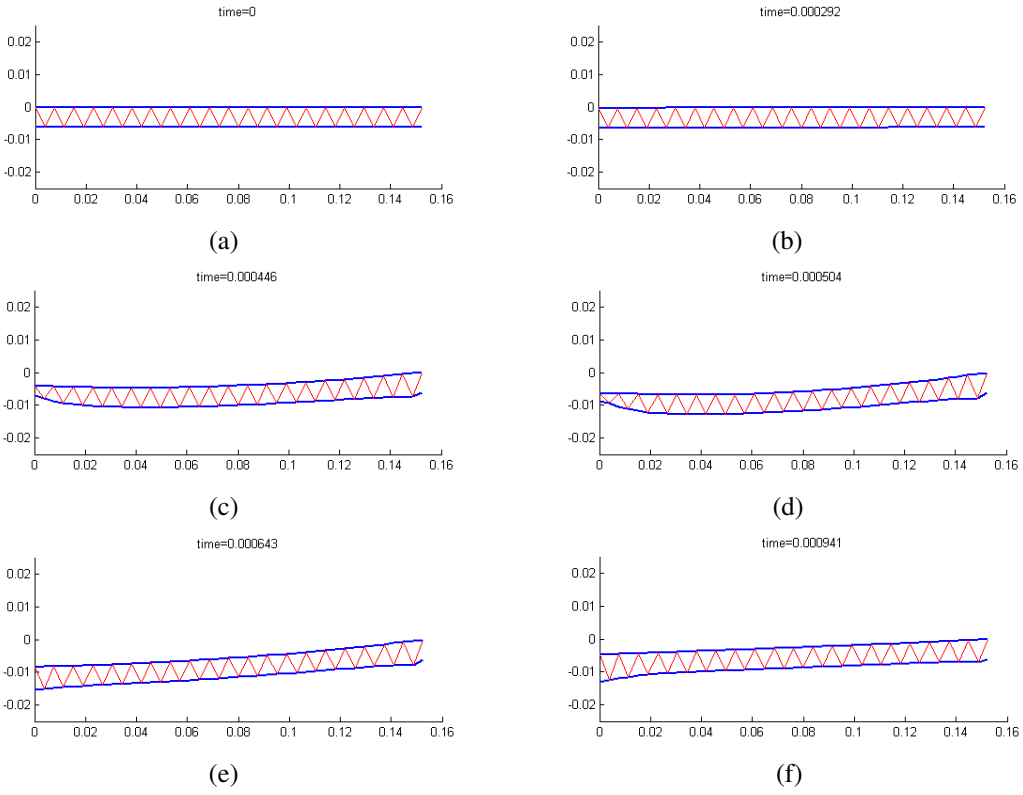

Figure 5-33: Interaction of blast wave and circular sandwich plate: plate deformation

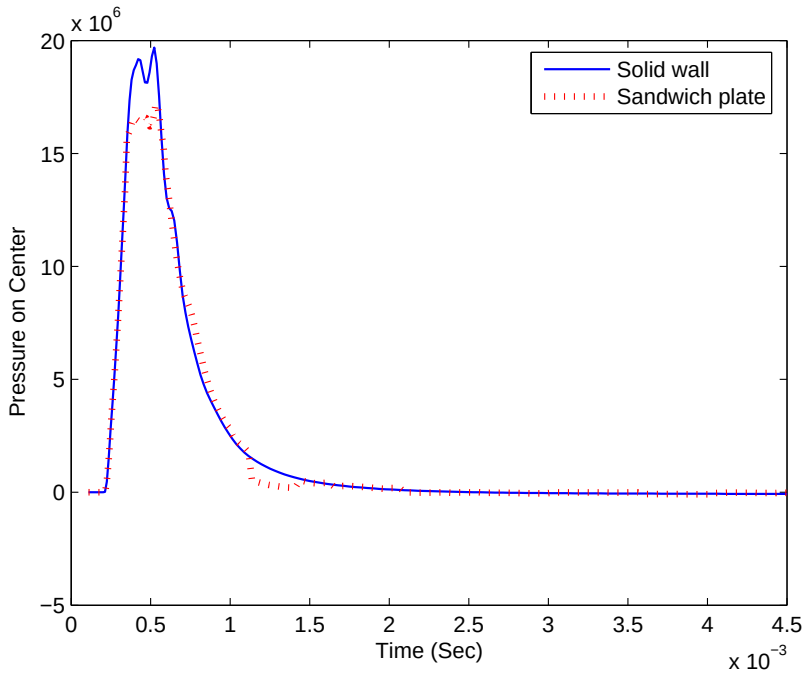

Figure 5-34: Interaction of blast wave and circular sandwich plate: Center pressure loading

Chapter 6

Non-linear Behavior in the Interaction

It was observed in the experiments that during the interaction of the plates and shock waves, the vibration of the plate was dominated by several modes. Comparison of the magnitude of these modes obtained from experiment with those from theoretical analysis or numerical simulation shows that modal suppression took place possibly as a result of the non-linear plastic deformation of the plate. Experimental results also show that there exists several extra peaks in the resonance signal power spectrum besides those from the basic modal frequencies of the plate. It has been suggested in [21] that these peaks may belong to the subharmonic and high harmonic of the acoustic excitation as a result of both non-linear vibration of the plate and non-linear propagation of the pressure waves. With the aid of numerical results obtained in previous chapters, we can further investigate this non-linear coupling process between the structure and shock wave interaction. Hence we introduce the *phase diagram* and *Poincare map* to further investigate this non-linear behavior.

6.1 Phase Diagram and Poincare Map

Phase diagram and Poincare map are effective tools in the study of non-linear system. The theories and their application can be found in [60]. Phase diagram can be obtained by plotting the time derivative against the quantity, and a typical Poincare map can be obtained

by plotting the $(n+1)th$ local maximum of the time series against the nth local maximum. For an ideal sinusoidal time series, the phase diagram is circular and the Poincare maps will reduce to a point. The phase diagram of a non-linear time series will have heavier circular lines due to the lack of precise periodicity or the lines will not be circular at all if the time series is highly non-linear. Similarly, the Poincare map for a non-linear system will have several spaced regions. In the case of a chaotic system, Poincare map points will be spreading all over the region. In the following study, phase diagrams and Poincare maps are obtained by processing the time series with the following Matlab code:

```
function poincare(time, data)
%plot poincare map and phase diagram.
%usage: poincare(time,data)
%Minwei Gong, 2005

%plot phase diagram
%find time derivative of data
diffdata=diff(data)./diff(time);
figure('Position',[100,100,700,300]);
subplot(1,2,1);
plot(data(1:end-1), diffdata);
set(gca,'PlotBoxAspectRatio',[1,1,1]);
xlabel('Phase Diagram');
%plot poincare map of data
%first find the local extrema of data
ad=diff(0.5*sign(diffdata));
p=find(abs(ad)==1);
%plot poincare map
subplot(1,2,2);
plot(data(p(1:end-1)+1),data(p(2:end)+1),'*');
```

```
set(gca,'PlotBoxAspectRatio',[1 1 1]);
xlabel('Poincare map');
```

In plotting Poincare maps, local extrema of the time series are needed and usually this process is not a trivial task. This program takes advantage of the Matlab index operation and thus all local extrema can be found effectively using a few line of codes. However, if identification of shock waves or blast waves peak is needed, a more advanced algorithm will be needed and the typical work is illustrated in [3].

6.2 Non-linear Vibration of the Plate

The phase diagrams and Poincare maps of the plate center displacement under shock wave impact was plotted in Figure 6-1, 6-2 and 6-3. Instead of using experiment data, numerical results are analyzed here to take advantage of idealized parameters. The center displacement phase diagram of all three plates is not circular, however, still follows a loop pattern. This suggests that there is non-linearity involved in the vibration of the plate, but this non-linearity is not dominant such that the vibrations still exhibit certain periodicity. The Poincare maps also showing slightly spreading of the extrema points, but these points are still clustered, thus such non-linearity is not dominant. Comparing the Poincare Map of different plates, it appears that the stainless steel plate has most spreading on the map, while the composite plate has the least. This suggests that this non-linearity is related to the displacement magnitude of the plate, where the stainless steel plate has the largest displacement and the composite plate has the smallest. Because all plates are modelled as linear in the Finite Element code, the source of this linearity should be solely attributed to the interaction process, where the loading on the plate is not uniform or perfectly periodic.

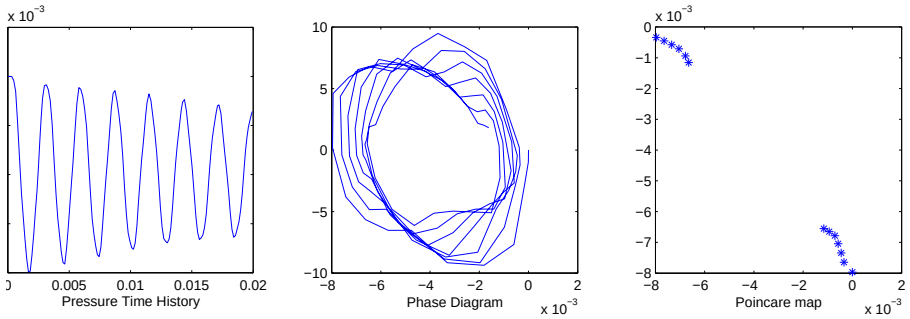

Figure 6-1: Aluminum plate center displacement phase diagram and Poincare map.

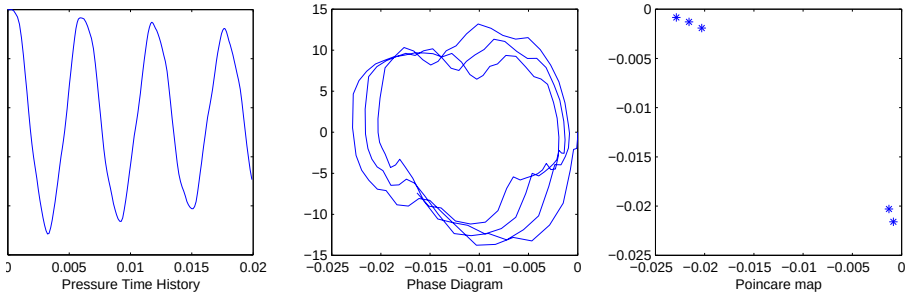

Figure 6-2: Stainless steel plate center displacement phase diagram and Poincare map.

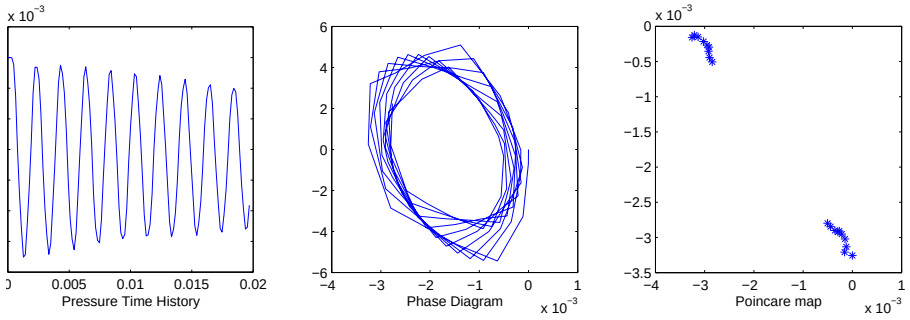

Figure 6-3: Composite plate center displacement phase diagram and Poincare map.

6.3 Non-linear Pressure Loading on the Plate

The non-linear pressure loading on the plate can be further analyzed using a similar approach above. The phase diagrams and Poincare maps of plates center pressure loading during the interaction was plotted in Figure 6-4, 6-5 and 6-6. From the time history plot, we can already see that all these pressure histories are not perfectly sinusoid, even though there exists certain periodicity. It appears that the pressure history with the stainless steel is the cleanest while that with the composite is of the opposite. The phase diagram of

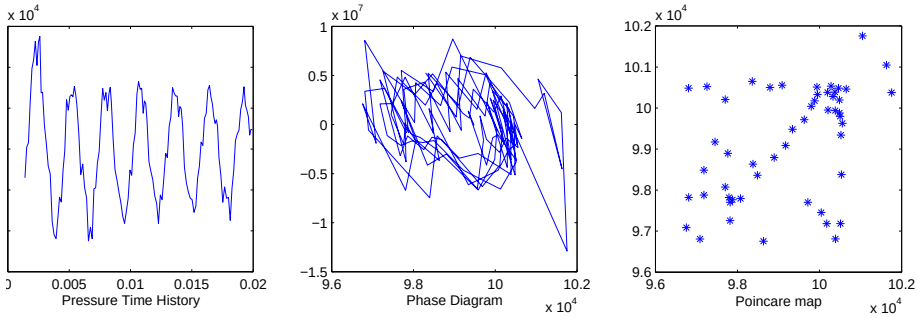

Figure 6-4: Aluminum plate center pressure phase diagram and Poincare map.

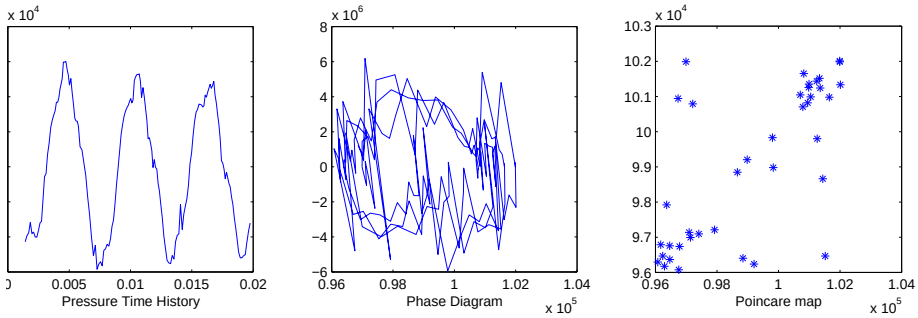

Figure 6-5: Stainless steel plate center pressure phase diagram and Poincare map.

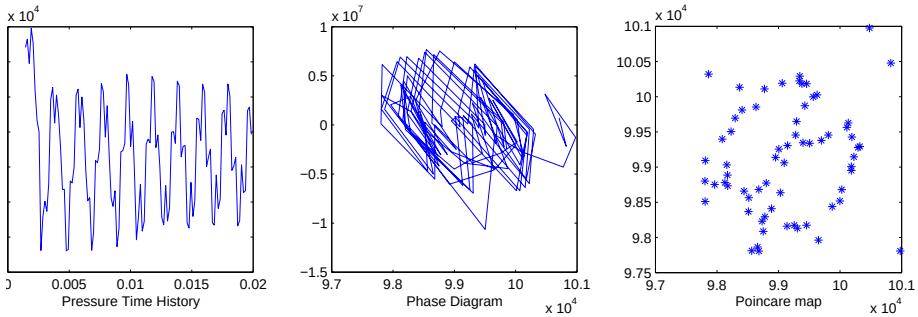

Figure 6-6: Composite plate center pressure phase diagram and Poincare map.

the pressure in the case of stainless steel plate is less chaotic and certain loop can still be observed, while in the case of the composite plate, lines have been crossing each other heavily thus it appears that the pressure loading on the composite is highly non-linear. All Poincare maps are showing considerable spreading. However, in the case of stainless steel plate, most of the points are linearly correlated along the diagonal line. In the case of the composite plate, such spreading has a different pattern, where those points seems to be clustered around two loops. Such kind of clustering suggests the existence of non-linear

harmonics or subharmonics in the pressure time history.

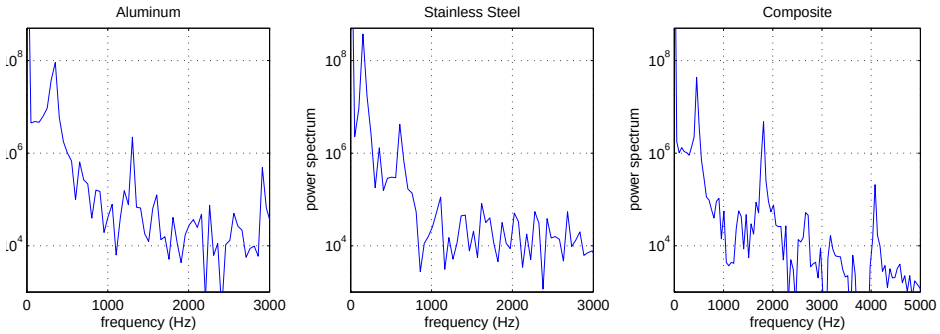

Figure 6-7: Power spectrum of plates center pressure.

These non-linear frequency characteristics are further illustrated in Figure 6-7, where the power spectra of the plates' center pressure are plotted. In these plots, besides the major peaks which belongs to the natural frequency of the plate vibration modes, there also exist lots of small peaks. More interesting results can be obtained if we further compare the magnitude of the basic natural frequency peaks of each plate. In the case of stainless steel plate, the ratio between the first peak and second peak is at about 100, while for the aluminum plate it is about 50 and for the composite plate, it is only 10. This suggests that while the composite plate has a higher fundamental frequency and less center displacement, somehow its second modes has been amplified in the non-linear process. Yet in the analysis from previous section, the center displacement of the composite plate is showing the least non-linearity. This behavior can be further confirmed by the experiment results, shown in Figure 2-16 where the strain signal appears to be cleaner than that of the metallic plate, the acoustic resonance pressure is showing lots of small spikes. This phenomena is illustrated more clearly with the aid of power spectrum shown in Figure 2-17 and 2-18. Similar phenomena is also observed in [22] where through numerical simulation of a plate excited by time harmonic, normally incident acoustic source, acoustic waves propagate non-linearly into the far-field. The non-linear propagation of these pressure waves is a result of complicate interactions between these pressure waves themselves. To further investigate this phenomena, the one-dimensional non-linear propagation of pressure waves is illustrated

analytically in the next section.

6.4 Non-linear Propagation of Pressure Waves

From analysis in the previous section, we find that during the interaction the pressure propagation is non-linear. This non-linear process starts as soon as the impact of the shock wave set the plate in motion. Such plate motion will again transfer energy into the flow fields and set the fluid in motion, which will result as a series of infinitesimal pressure waves, as shown in Figure 6-8.

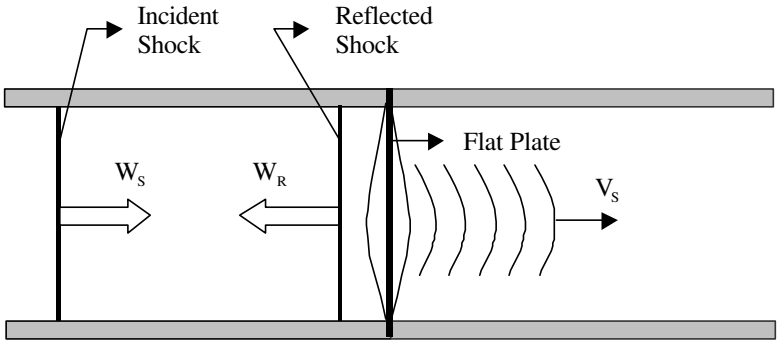

Figure 6-8: An axisymmetrically loaded plate.

If the plate is vibrating periodically with a series of modes, we can assume a simple form of its transverse displacement velocity as:

$$u(t) = \sum A_i \sin \omega_i t \tag{6.1}$$

where

A_i is the magnitude of the plate transverse displacement velocity belongs to the ith mode,

ω_i is the ith modal frequency of the plate.

The plate ith mode transverse displacement is:

$$x_i = \int_0^t u_i(t) = \frac{A_i}{\omega_i}(1 - cos\omega_i t) \tag{6.2}$$

As the acoustic wave travels through the fluid, it imparts velocity to its particles and creates infinitesimal changes in the fluid properties. Considering the propagation of a wave of finite amplitude into an inviscid compressible fluid in a constant cross-sectional area duct, assume the duct to be frictionless with no heat interaction, i.e. the flow is adiabatic, the fluid ahead of the wave has uniform properties, p, ρ, T and so on, the flow properties across these waves can be modelled with the following analysis as similar to those in [27].

$$\begin{aligned} x &= (u + a)t + f(u) \\ u &- \frac{2a}{\gamma - 1} = K \end{aligned} \tag{6.3}$$

Here K is referred to as Riemann Invariable along the characteristic line, $(u + a)$ is the right-running wave propagation speed, its relationship with pressure is:

$$\frac{d}{dp}(u + a) = \frac{du}{dp} + \frac{da}{dp} \tag{6.4}$$

With the help of perturbation method and the perfect gas relationship, this characteristic relationship can be further expressed as:

$$\frac{d}{dp}(u + a) = \frac{1}{2\rho^4 a^3}(\frac{d^2 p}{dv^2})_s \tag{6.5}$$

where $v = \frac{1}{\rho}$.

This equation shows the relationship between wave propagation and pressure. Form the temperature-pressure relationship for perfect gas, $pv^\gamma = C$,

$$\frac{d^2 p}{dv^2} = \frac{\gamma(\gamma + 1)p}{v^2} > 0 \tag{6.6}$$

Subsequently we have

$$\frac{d}{dp}(u+a) > 0 \tag{6.7}$$

Thus if the wave is travelling in the same direction as the particle, increasing of pressure will result in an increase of the waves travelling velocity $u + a$. This means that the compression waves formed by the right hand-side acceleration of the plate will steepen as they travel along the duct, and the compression region tending to coalesce into a shock wave. For the expansion waves formed by the left hand-side acceleration of the plate, it tends to spread wider as a result of the reduction in pressure. This will result in a distortion of the original waves emitted from the fluid-structure interface. A sinusoidal wave will no longer be sinusoidal while experiencing non-linear phase and frequency shift. Under extreme condition the compression of the wavefront may eventually reaches a point where a shock forms. This compression waves steepening and shock wave formation process is illustrated in Figure 6-9. In this figure t_0 is the time when the steepening of the compression

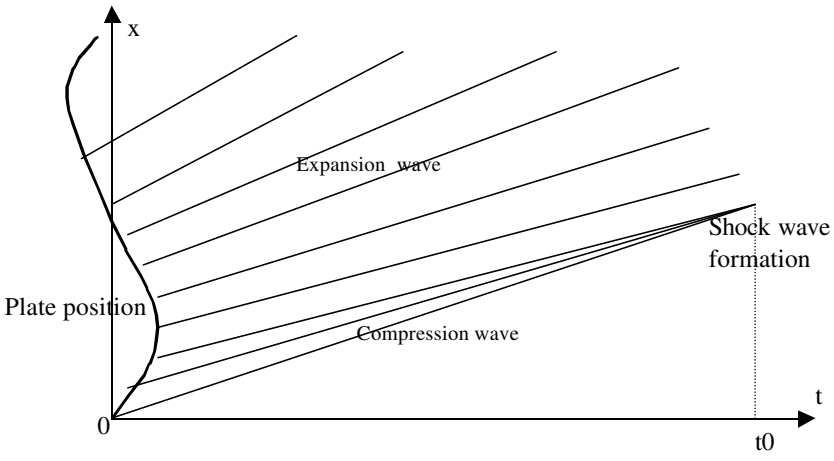

Figure 6-9: Steepening of compression wave and the formation of shock wave.

wave is maximum and a shock is formed. Notice that at this point isentropic flow ceases to be valid because of the large gradients in the flow variables. If, however, the shock is pursued further with the assumption of isentropic flow, then at the location where the shock

is formed, $(\frac{\partial u}{\partial x})_t$ tends to be infinity. Equivalently, we have:

$$(\frac{\partial x}{\partial u})_t|_{u=0} = 0 \tag{6.8}$$

This gives the shock wave forming condition. From aforementioned wave relation Equation 6.3, we have:

$$\begin{aligned} a &= a_1 + \frac{\gamma - 1}{2}u \\ x &= (a_1 + \frac{\gamma + 1}{2}u)t + f(u) \end{aligned} \tag{6.9}$$

where a_1 is the sound speed of the quiescent area before the compression wave arrives. Take the derivative of x with regard to u at $u = 0$ and make the derivative to be zero, we have the shock wave formation time:

$$t_s = -\frac{2}{\gamma + 1}f'(0) \tag{6.10}$$

Yet the expression of $f(u)$ is to be determined from the boundary condition. At the exact interface between the plate and structure, we have

$$x_p = \frac{A_i}{\omega_i}(1 - \cos\omega_i t) = (a_1 + \frac{\gamma + 1}{2}u_p)t + f(u) \tag{6.11}$$

where subscript p indicate properties at the plate and structure interface. We can express all t in terms of u. With $t = \arcsin\frac{u_p}{A_i}$ and $\cos\omega_i t = \sqrt{1 - \frac{u_p^2}{A_i^2}}$, we have:

$$\frac{A_i}{\omega_i}(1 - \sqrt{1 - \frac{u_p^2}{A_i^2}}) = \frac{1}{\omega_i}(a_1 + \frac{\gamma + 1}{2}u_p)\arcsin\frac{u_p}{A_i} + f(u) \tag{6.12}$$

From this we can get the expressions for $f(u)$ and $f'(u)$ as:

$$f(u) = \frac{A_i}{\omega_i}(1 - \sqrt{1 - \frac{u^2}{A_i^2}}) - \frac{1}{\omega_i}(a_1 + \frac{\gamma + 1}{2}u)\arcsin\frac{u}{A_i} \tag{6.13}$$

$$f'(u) = \frac{A_i}{\omega_i} \frac{\frac{u}{A_i^2}}{\sqrt{1 - \frac{u^2}{A_i^2}}} - \frac{\gamma + 1}{2\omega_i} \arcsin \frac{u}{A_i} - \frac{1}{\omega_i A_i}(a_1 + \frac{\gamma + 1}{2} u) \frac{1}{\sqrt{1 - \frac{u^2}{A_i^2}}} \tag{6.14}$$

So the shock wave is forming at time t_s:

$$t_s = -\frac{2}{\gamma + 1} f'(0) = \frac{2}{\gamma + 1}(\frac{a_1}{\omega_i A_i} + \frac{\gamma + 1}{2} \frac{k\pi}{\omega_i}) \tag{6.15}$$

where $k = 0, 1, ...N$. For $k = 0$, the shock wave forms at time:

$$t_s = \frac{2}{\gamma + 1} \frac{a_1}{\omega_i A_i} \tag{6.16}$$

And the location of shock wave formation x_s is:

$$x_s = a_1 t_s + f(0) = \frac{2}{\gamma + 1} \frac{a_1^2}{\omega_i A_i} + f(0) \tag{6.17}$$

Typical shock wave formation time for a plate vibrating at a frequency of $1kHz$ and maximum transverse displacement of $0.01m$ is about $0.72ms$. the corresponding shock wave is formatted at $0.24m$ away from the plate. Though shock wave is not presented on the plate during the interaction if all waves are assumed to be propagating one-dimensionally apart from the plate with the above derivation, the compression of the wavefront starts immediately at the fluid-structure interface, results in a non-linear behavior of the pressure fluctuation. Furthermore as the plate is not vibrating like a piston, the pressure waves will not propagating one-dimensionally, but rather in a two-dimensional manner while complicate interactions and reflections occur. Such complicate pressure wave patterns can also be observed in the pressure contours from numerical simulation. Such non-linear propagation of pressure waves can further complicate the loading on the plate, result in the non-linear vibration of the plate itself, further cascading the non-linearity. From above analysis we can also see that the faster the plate is vibrating, and the higher the vibrating frequency is, the stronger such non-linear effects will be. Because of this, the composite plate exhibits the highest non-linear effects on the pressure fluctuation because its natural frequency is

higher, and such non-linear behavior is more evident on the higher frequency modes.

6.5 On the Time Scale of Wave Reflection off the Structure

Numerical results also reveal that in the case of a shock wave reflecting off a flat elastic plate, reflection starts at the same time at all locations of contact between the shock front and the surface of the plate. In the present example, the characteristic time of the shock wave reflection is much less than the time needed for the plate to deform. It was also mentioned in [1] that "the importance of dynamic effects depends on the relative magnitudes of two characteristic times: the time characterizing the external application of the disturbance and the characteristic time of transmission of disturbance across the body". To estimate the time scale of the shock wave loading, the thickness of the shock wave can be used as a characteristic length scale of the disturbance thus it will be estimated as following.

Thickness of shock wave

A shock wave has a finite but very small thickness, Δ_s caused by "packing" of the molecules during the compression process as the shock wave moves through the fluid. The density of the fluid in the region of the shock wave tries to distribute itself evenly during the propagation of the shock wave into the undisturbed fluid. The distribution of density, pressure within the shock is governed by fluid viscosity. For shocks of moderate strength, theory and experiments all lead to the result that shock thickness Δ_s is in the order of magnitude of a few mean free paths (ℓ) of the gas, which can be expressed as: [48].

$$\Delta_s \simeq \frac{\nu}{V_1} = \frac{\nu}{M_1 a_1} \tag{6.18}$$

where V_1, M_1 and a_1 are the relative velocity, Mach number and sound speed before the shock, respectively. ν is the kinematic viscosity of the gas. For shocks of small and up

to moderate shock Mach number M_1, a better estimation of the shock thickness can be achieved by solving the Navier-Stokes equations which yields [54]:

$$\Delta_s \simeq \frac{8\ell}{3(M_1 - 1)} \simeq \frac{8\nu}{3a_1(M_1 - 1)} \tag{6.19}$$

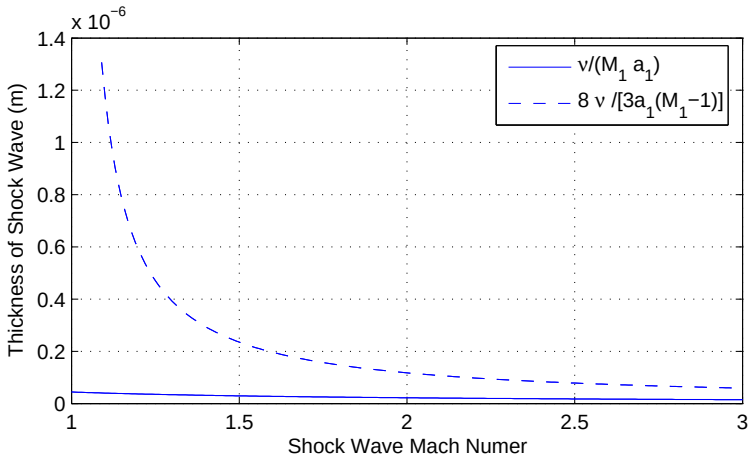

Figure 6-10: Shock wave thickness vs. Mach Number

The shock wave thickness as predicted by Equation 6.18 and 6.19 are plotted against Mach number $M_1 = V_1/a_1$ in Figure 6-10, where the air properties under normal temperature are used, with $\nu = 1.5 \times 10^{-5} m^2/s$ and $a_1 = 340 m/s$. At low Mach number there are several order-of-magnitude difference on the shock wave thickness as predicted by Equation 6.18 and 6.19, where Equation 6.19 is a more closer estimate.

In the case of Mach number 1.2 as used in the experiment and numerical simulation, we have the shock wave thickness as $0.6\mu m$, the associated time for shock to travel this thickness is $1.5 \times 10^{-9} s$. This time can be compared with the characteristic time associated with the transmission of stress waves across the solid plate. The wave propagation speed in the solids is around $6 \times 10^3 m/s$ for both aluminum and steel. Thus the time needed for stress waves to travel across the thickness of the plate, $3.2 \times 10^{-3} m$ as used in this experiment, is $5.2 \times 10^{-7} s$. Compare with the time scale associated with the shock wave reflection, this time scale is of two orders of magnitude larger. As a result, during the

reflection of the shock wave off the plate, the plate is loaded but not deformed significantly such that the shock wave is reflected off the plate surface uniformly. However, the plate will start to gain velocity as soon as the aerodynamic loading is applied. As a result of the plate motion pressure waves will be generated at the plate surfaces and further propagate towards the flow field non-linearly following the reflected shock wave.

Another characteristic scale associated with non-linearity arise during the interaction process, which is the relationship between the characteristic time scale of the plate represented by its natural frequency modes and the time scale of the pressure wave propagation represented by the sound speed inside the fluid flow field. Non-linearity is intensified when the plate is vibrating at high frequency while the wave propagation speed is low.

6.6 Summary

Analysis shows that non-linearity arises because the wave propagation in the fluid is non-linear. Further more, such non-linear pressure wave will result in a non-linear and non-uniform loading on the plate, which will cause the plate to vibrating non-linearly, especially when the plate vibration has a relatively larger magnitude.

There maybe other factors that will further intensify the non-linear behavior. Damping played an important role during the interaction and it is more evident in the experimental result, especially in the case of composite plate. Such damping will also result in a non-linear broadening of spectrum.

Research in [13] also showing that fluid wall shear stress can both suppress and increase the non-linear response of the plate and acoustic resonance. Preliminary numerical experiment in this research also shows that the effect of viscosity can further attribute to the non-linear behavior of the flow behavior, in the forms of vorticity generation and transport.

From experimental result in the case of the metallic plates, the non-linear behaviors of the interaction process present as the suppression of the first mode. Such non-linear behavior is caused by plastic deformation of the plate upon large shock wave impact loading. To

fully resolve such non-linear behavior, an advanced non-linear FEM model for the plate is needed in the future.

Chapter 7

Conclusions and Final Remarks

In this thesis, the mutual interaction of moving shock waves and structures was studied experimentally, numerically and theoretically.

Experiments were carried out in a shock tube to investigate the aero-elastic response of fully clamped thin circular plates during face-on impact with planar shock waves. High frequency response dynamic strain history was obtained on various locations of the plate and measurement of acoustic pressure excited by the vibrating plate was performed as well. Experimental results show that plates made of different material exhibits distinct modal response when subject to shock wave loading. It is also observed that there exists non-linear acoustic excitation by the plate. Damping of the plate vibration in time was also observed on all plates during the interaction.

Analytical formulas based on Poisson-Kirchoff theory were employed to determine the modal frequency. Finite Element Analysis revealed that modal frequency calculated by using a coupled system of equations between the fluid and solid phases of monolithic materials provided predictions closer to measured values than that with classical modal analysis.

Further more, a coupled aero-elastic solver based on *quad-edge* data structure was implemented to solve the fluid structure interaction problem. The moving boundary was treated with an advancing front remeshing which was fully conservative. Adaptive mesh

refinement was also implemented for improved efficiency and accuracy. It was also shown that shock wave reflection starts at the same time at all locations of contact, and the reflected pressure may exceed the pressure reflected off a rigid wall in comparable configuration. Modal response of the plate subject to shock wave loading was observed in the strain signal and compared with experiments, where non-linear plastic deformation contributes severely to the suppression of the first modes in the metallic plate case. Aerodynamic damping of the plate vibration was reproduced in the numerical simulation without manually adding any damping coefficient.

Further non-linear analysis on the numerical results shows that the mutual interaction process is non-linear. Analysis shows that non-linearity arises because the wave propagation in the fluid is non-linear and it will further cascade a non-linear and non-uniform loading on the plate. Non-linearity intensifies when the plate is vibrating at high frequency while the wave propagation speed is low, which is characterized by the characteristic time scale of the plate vibration and pressure wave propagation.

There maybe other factors that will further intensify the non-linear behavior. Damping played an important role during the interaction and it is also one source of non-linearity. Viscous shear stress can also contribute to the non-linear response of the plate and acoustic resonance. Non-linear behavior caused by plastic deformation of the plate upon large shock wave impact loading was also evident in the experiment. To fully resolve these non-linear behaviors, a more advanced non-linear FEM model for the plate coupled with a viscous fluid flow model is desirable in the future.

Bibliography

[1] J. Achenbach. *Wave propagation in elastic solids*. elsevier science publishers, eight impression edition, 1999.

[2] A.M.Saad. *Compressible Flow*. Prentice Hall, New Jersey, 1984.

[3] Y. Andreopoulos, M. Gong, Z. Wang, and S. Xanthos. A probe to measure direction and strength of moving shocks or blast waves. *AIAA J*, vol. 41(3):pp 476–484, 2003.

[4] E. Balaras. Modeling complex boundaries using an external force field on fixed cartesian grids in large-eddy simulations. *Computers & Fluids*, 33(3):375, 2004.

[5] T. Barth. Numerical aspects of computing viscous high reynolds number flows on unstructured meshes. *AIAA Paper*, 91-0721, 1991.

[6] T. J. Barth. Higher order solution of the euler equations on unstructured grids using quadratic reconstruction. In *28th aerospace sciences meeting*, volume 90-0013, Reno Nevada, 1990. AIAA paper.

[7] T. J. Barth and D. C. Jespersen. The design and application of upwind schemes on unstructured meshes. In *27th aerospace sciences meeting*, volume 89-0366, Reno, Nevada, 1989. AIAA Paper.

[8] B. G. Baumgart. *Geometric modeling for computer vision.* PhD thesis, 1974.

[9] G. Berti. *Generic software components for Scientific Computing*. PhD thesis, Faculty of mathematics, computer science, and natural science, BTU Cottbus, Germany, 2000.

[10] F. B. A. Beshara. Modelling of blast loading on aboveground structures–i. general phenomenology and external blast. *Computers & Structures*, 51(5):585, 1994.

[11] M. E. Braaten and C. SD. Three dimensional unstructured adaptive multigrid scheme for the navier-stokes equations. *AIAA J*, 34(2):281–90, 1996.

[12] G. Briassulis, J. H. Agui, J. Andreopoulos, and C. B. Watkins. A shock tube research facility for high-resolution measurements of compressible turbulence. *Experimental Thermal and Fluid Science*, 13(4):430, 1996.

[13] W. Buhler and A. Frendi. Effect of fluid wall shear stress on non-linear beam vibration. *Journal of Sound and Vibration*, 270(4-5):793, 2004.

[14] M. S. Darwish and F. Moukalled. Tvd schemes for unstructured grids. *International Journal of Heat and Mass Transfer*, 46(4):599, 2003.

[15] S. F. Davis. A rotationally biased upwind difference scheme for the euler equations. *Journal of Computational Physics*, 56(1):65, 1984.

[16] D. DeZeeuw and K. G. Powell. An adaptively refined cartesian mesh solver for the euler equations. *Journal of Computational Physics*, 104(1):56, 1993.

[17] E. H. Dowell and K. C. Hall. Modeling of fluid-structure interaction. *Annu Rev. Fluid Mech*, 33:445–90, 2001.

[18] C. M. Eastman. Introduction to computer aided design,course notes, 1982.

[19] C. Farhat, M. Lesoinne, and P. Le Tallec. Load and motion transfer algorithms for fluid/structure interaction problems with non-matching discrete interfaces: Momentum and energy conservation, optimal discretization and application to aeroelasticity. *Computer Methods in Applied Mechanics and Engineering*, 157(1-2):95, 1998.

[20] N. A. Fleck and V. S. Deshpande. The resistance of clamped sandwich beams to shock loading. *Journal of Applied Mechanics, Transactions ASME*, 71(3):386.

[21] A. Frendi, L. Maestrello, and A. Bayliss. Coupling between plate vibration and acoustic radiation. *Journal of Sound and Vibration*, 177(2):207, 1994.

[22] A. Frendi, L. Maestrello, and L. Ting. An efficient model for coupling structural vibrations with acoustic radiation. *Journal of Sound and Vibration*, 182(5):741, 1995.

[23] N. Frink. Recent progress toward a three dimensional unstructured navier-stokes flow solver. *AIAA Paper*, 94-0061, 1994.

[24] J. Glimm, M. J. Graham, J. Grove, X. L. Li, T. M. Smith, D. Tan, F. Tangerman, and Q. Zhang. Front tracking in two and three dimensions. *Computers & Mathematics with Applications*, 35(7):1, 1998.

[25] L. Guibas and J. Stolfi. Primitives for the manipulation of general subdivisions and computation of voronoi diagrams. *ACM Transactions on Graphics*, 4(2):74–123, 1985.

[26] A. D. Gupta, F. H. Gregory, R. L. Bitting, and S. Bhattacharya. Dynamic analysis of an explosively loaded hinged rectangular plate. *Computers & Structures*, 26(1-2):339, 1987.

[27] Z. Han and X. Yin. *Shock Dynamics*. Springer, 1993.

[28] A. Harten. High resolution schemes for hyperbolic conservation laws. *Journal of Computational Physics*, 49(3):357, 1983.

[29] A. Harten, B. Engquist, S. Osher, and S. R. Chakravarthy. Uniformly high order accurate essentially non-oscillatory schemes, iii. *Journal of Computational Physics*, 131(1):3, 1997.

[30] P. Heckbert. Quad edge data structure and library. 2001.

[31] W. D. Henshaw and D. W. Schwendeman. An adaptive numerical scheme for high-speed reactive flow on overlapping grids. *Journal of Computational Physics*, 191(2):420, 2003.

[32] C. W. Hirt, A. A. Amsden, and J. L. Cook. An arbitrary lagrangian-eulerian computing method for all flow speeds. *J. Comput. Phys.*, 135(2):203–216, 1997. 260732 http://dx.doi.org/10.1006/jcph.1997.5702.

[33] B. Hopkinson. British ordnance borad minutes. Technical Report 13565, British Ordnance Office,London, 1915.

[34] R. Houlston, J. E. Slater, N. Pegg, and C. G. Desrochers. On analysis of structural response of ship panels subjected to air blast loading. *Computers & Structures*, 21(1-2):273, 1985.

[35] M. E. Hubbard. Multidimensional slope limiters for muscl-type finite volume schemes on unstructured grids. *Journal of Computational Physics*, 155(1):54, 1999.

[36] G.-S. Jiang and C.-W. Shu. Efficient implementation of weighted eno schemes. *Journal of Computational Physics*, 126(1):202, 1996.

[37] B. K-J. *Finite element procedures*. Prentice-Hall, Englewood Cliffs,NJ, 1996.

[38] R. Kamakoti and W. Shyy. Fluid-structure interaction for aeroelastic applications. *Progress in Aerospace Sciences*, 40(8):535, 2004.

[39] J. M. Legakis and K. RJ. Data structures for unstructured meshes. course notes. 2000.

[40] R. Lohner. An adaptive finite element scheme for transient problems in cfd. *Computer Methods in Applied Mechanics and Engineering*, 61(3):323, 1987.

[41] R. Lohner. Mesh adaptation in fluid mechanics. *Engineering Fracture Mechanics*, 50(5-6):819, 1995.

[42] D. J. Mavriplis. Unstructured mesh generation and adaptivity. In *VKI Lect. Ser. Comput. Fluid Dyn.*, volume 26th, 1995.

[43] D. J. Mavriplis. Unstructured grid techniques. *Annual Review of Fluid Mechanics*, 29(1):473–514, 1997.

[44] G. C. Mays and P. D. Smith. *Blast effects on buildings*. Thomas Telford, 1995.

[45] O.C.Zienkiewicz and R. Taylor. The finite element method. Butterworth-Heinemann, 2000.

[46] C. S. Peskin. Numerical analysis of blood flow in the heart. *Journal of Computational Physics*, 25(3):220, 1977.

[47] X. Qiu, V. Deshpande, and N. Fleck. Dynamic response of a clamped circular sandwich plate subject to shock loading. *Journal of Applied Mechanics, Transactions ASME*, 71:637, 2004.

[48] R.A.Granger. *Fluid Mechanics*. Dover Publications, New York, 1995.

[49] P. L. Roe. Approximate riemann solvers, parameter vectors, and difference schemes. *Journal of Computational Physics*, 43(2):357, 1981.

[50] C. Ross. *Finite Element programs for axisymmetric Problems in Engineering*. John Wiley & Sons.

[51] R.S.Weiner. Forced axisymmetric motions of circular elastic plates. *Journal of Applied Mechanics, Transaction ASME*, Series E(65-APMW-7), 1965.

[52] M. Sun. *Numerical and Experimental Studies of Shock Wave Interaction with Bodies*. PhD thesis, Tohoku University, 1998.

[53] G. Taylor. *The Pressure and Impulse of Submarine Explosion Waves on Plates*, volume III of *The Scientific Papers of G. I. Taylor*. Cambridge Univ. Press, Cambridege, UK, 1963.

[54] P. A. Thompson. *Compressible Fluid Dynamics*. McGraw-Hill, 1988.

[55] S. Timoshenko and S. Woinowsky-Krieger. *Theory of plates and shells*. McGRAW-HILL, second edition edition, 1959.

[56] E. F. Toro. *Riemann Solvers and Numerical Methods for Fluid Dynamics*. Springer, 1997.

[57] H. S. Turkmen and Z. Mecitoglu. Nonlinear structural response of laminated composite plates subjected to blast loading. *AIAA Journal*, 37(12):1639, 1999.

[58] B. Van Leer. Towards the ultimate conservative difference scheme. v. a second-order sequel to godunov's method. *Journal of Computational Physics*, 32(1):101, 1979.

[59] I. Wesseling. *Principles of computational fluid dynamics*. Springer, 2000.

[60] S. Wiggins. *Introduction to applied nonlinear dynamical systems and chaos*. Springer-Verlag, 1990.

[61] Z. Xue and J. W. Hutchinson. Preliminary assessment of sandwich plates subject to blast loads. *International Journal of Mechanical Sciences*, 45(4):687, 2003.

[62] Z. Xue and J. W. Hutchinson. A comparative study of impulse-resistant metal sandwich plates. *International Journal of Impact Engineering*, 30(10):1283, 2004.